

# IOWA STATE UNIVERSITY

## Digital Repository

---

Retrospective Theses and Dissertations

Iowa State University Capstones, Theses and  
Dissertations

---

1980

## Two-phase flow characterization using reactor noise techniques

Mikdam Mahmood Saleh

*Iowa State University*

Follow this and additional works at: <https://lib.dr.iastate.edu/rtd>



Part of the [Nuclear Engineering Commons](#), and the [Oil, Gas, and Energy Commons](#)

---

### Recommended Citation

Saleh, Mikdam Mahmood, "Two-phase flow characterization using reactor noise techniques " (1980). *Retrospective Theses and Dissertations*. 7125.

<https://lib.dr.iastate.edu/rtd/7125>

This Dissertation is brought to you for free and open access by the Iowa State University Capstones, Theses and Dissertations at Iowa State University Digital Repository. It has been accepted for inclusion in Retrospective Theses and Dissertations by an authorized administrator of Iowa State University Digital Repository. For more information, please contact [digirep@iastate.edu](mailto:digirep@iastate.edu).

## **INFORMATION TO USERS**

This was produced from a copy of a document sent to us for microfilming. While the most advanced technological means to photograph and reproduce this document have been used, the quality is heavily dependent upon the quality of the material submitted.

The following explanation of techniques is provided to help you understand markings or notations which may appear on this reproduction.

1. The sign or "target" for pages apparently lacking from the document photographed is "Missing Page(s)". If it was possible to obtain the missing page(s) or section, they are spliced into the film along with adjacent pages. This may have necessitated cutting through an image and duplicating adjacent pages to assure you of complete continuity.
2. When an image on the film is obliterated with a round black mark it is an indication that the film inspector noticed either blurred copy because of movement during exposure, or duplicate copy. Unless we meant to delete copyrighted materials that should not have been filmed, you will find a good image of the page in the adjacent frame.
3. When a map, drawing or chart, etc., is part of the material being photographed the photographer has followed a definite method in "sectioning" the material. It is customary to begin filming at the upper left hand corner of a large sheet and to continue from left to right in equal sections with small overlaps. If necessary, sectioning is continued again—beginning below the first row and continuing on until complete.
4. For any illustrations that cannot be reproduced satisfactorily by xerography, photographic prints can be purchased at additional cost and tipped into your xerographic copy. Requests can be made to our Dissertations Customer Services Department.
5. Some pages in any document may have indistinct print. In all cases we have filmed the best available copy.

**University  
Microfilms  
International**

300 N. ZEEB ROAD, ANN ARBOR, MI 48106  
18 BEDFORD ROW, LONDON WC1R 4EJ, ENGLAND

8106050

SALEH, MIKDAM MAHMOOD

TWO-PHASE FLOW CHARACTERIZATION USING REACTOR NOISE  
TECHNIQUES

*Iowa State University*

PH.D.

1980

University  
Microfilms  
International 300 N. Zeeb Road, Ann Arbor, MI 48106

**PLEASE NOTE:**

In all cases this material has been filmed in the best possible way from the available copy. Problems encountered with this document have been identified here with a check mark ✓.

1. Glossy photographs ✓
2. Colored illustrations \_\_\_\_\_
3. Photographs with dark background ✓
4. Illustrations are poor copy ✓
5. Print shows through as there is text on both sides of page \_\_\_\_\_
6. Indistinct, broken or small print on several pages ✓
7. Tightly bound copy with print lost in spine \_\_\_\_\_
8. Computer printout pages with indistinct print ✓
9. Page(s) \_\_\_\_\_ lacking when material received, and not available from school or author
10. Page(s) \_\_\_\_\_ seem to be missing in numbering only as text follows
11. Poor carbon copy \_\_\_\_\_
12. Not original copy, several pages with blurred type \_\_\_\_\_
13. Appendix pages are poor copy \_\_\_\_\_
14. Original copy with light type \_\_\_\_\_
15. Curling and wrinkled pages \_\_\_\_\_
16. Other \_\_\_\_\_

**Two-phase flow characterization using  
reactor noise techniques**

**by**

**Mikdam Mahmood Saleh**

**A Dissertation Submitted to the  
Graduate Faculty in Partial Fulfillment of the  
Requirements for the Degree of  
DOCTOR OF PHILOSOPHY**

**Major: Nuclear Engineering**

**Approved:**

Signature was redacted for privacy.

**In Charge of Major Work**

Signature was redacted for privacy.

**For the Major Department**

Signature was redacted for privacy.

**For the Graduate College**

**Iowa State University  
Ames, Iowa**

**1980**

## TABLE OF CONTENTS

	Page
I. INTRODUCTION	1
II. LITERATURE REVIEW	5
A. Input Noise Sources in Nuclear Reactors	5
B. Stochastics of Two-phase Flow in a Reactor Coolant Channel	7
C. Theoretical and Experimental Investigations of Void Fluctuations in Nuclear Reactors	11
III. THEORY	18
A. Evaluation of the Input Noise Source to Void Fluctuations	18
B. Two-phase Flow and its Associated Noise Sources	32
C. Derivation of the Detector Response Model	49
D. Evaluation of the APSD and CPSD of the detector response function	65
IV. EXPERIMENTAL SET-UP	70
A. The UTR-10 Reactor	70
B. Experimental Loop	70
C. The Signal Processing System	76
V. EXPERIMENTAL PROCEDURES	85
A. Anti-aliasing Procedures	87
B. Electronics and Software System Checks	87
C. Two-phase Flow Characteristics	89
VI. RESULTS AND DISCUSSION	96
A. Auto-power Spectral Density (APSD) Measurements	97

	Page
B. Comparison With Theory	110
C. The Cross-power Spectral Density (CPSD)	115
VII. CONCLUSIONS	121
VIII. SUGGESTIONS FOR FUTURE WORK	125
IX. LITERATURE CITED	127
X. ACKNOWLEDGMENTS	137
XI. APPENDIX A: COMPUTATION OF THE SPECTRA VIA FFT CALCULATIONS	138
A. The Algorithm For Calculating the APSD's of Two Channels and Their Associated CPSD	138
B. Program Listing	143
XII. APPENDIX B: EVALUATION OF THE ADJOINT RESPONSE USING THE CRAM CODE	153
A. Two-Dimensional Modeling of the UTR-10	153
B. Checking the CRAM Code	154
C. CRAM Results	158
D. Input Data Preparation	171
E. Sample Input Data to CRAM	179
XIII. APPENDIX C: THE COMPUTATIONS OF THE APSD AND CPSD OF THE VOID FRACTION FOR TWO-PHASE FLOW	183
A. SOURCE Results	185
B. Listing of the SOURCE Code	191

## LIST OF TABLES

	Page
<b>Table 3.1.</b> Stochastic processes and change of state induced in the test channel	23
<b>Table 6.1.</b> Experimental two-phase flow data for the test loop	98
<b>Table 6.2.</b> Summary of experimental results	99
<b>Table B.1.</b> Macroscopic parameters for the fuel region of the UTR-10 at a coolant temperature of 32°C	156
<b>Table B.2.</b> Macroscopic parameters for the graphite reflector region of the UTR-10	156
<b>Table B.3.</b> Macroscopic parameters for water at a temperature of 32°C	157
<b>Table B.4.</b> Two-group macroscopic parameters for the regions of the UTR-10	157
<b>Table B.5.</b> The thermal adjoint response (at $x = y = 0$ ) for a detector at position $Z = 15$ cm	165
<b>Table B.6.</b> The thermal adjoint response at $(x = y = 0)$ for a detector at position $Z = 27$ cm	166

## LIST OF FIGURES

	Page
<b>Figure 2.1.</b> Diabatic flow regimes [62]	<b>9</b>
<b>Figure 3.1.</b> Schematic diagram of the test loop	34
<b>Figure 3.2.</b> APSD, due to bubbles transport, as computed for a simple theoretical model	48b
<b>Figure 4.1.</b> The longitudinal cross-sectional view of the UTR-10 reactor [96]	71
<b>Figure 4.2.</b> A schematic diagram of the experimental loop [96]	72
<b>Figure 4.3.</b> The detailed design of the test section assembly [96]	74
<b>Figure 4.4.</b> Examples of two-phase flow regimes created in the test section: (a) bubbly flow; (b) bubbly (lower section) and slug flow (upper section); (c) bubbly (lower) and slug and churn flow (upper); (d) churn (below) and slug and churn flow (upper)	78
<b>Figure 4.5.</b> The experimental two-phase flow loop	79
<b>Figure 4.6.</b> Block diagram of the reactor noise detection system	80
<b>Figure 4.7.</b> Flow diagram of the FFT program	82
<b>Figure 4.8.</b> The data acquisition system	83
<b>Figure 4.9.</b> Block diagram of the data acquisition system	84
<b>Figure 5.1.</b> APSD at 500 W, observed at detector A, for the case of bubbly two-phase flow and liquid flow only	86
<b>Figure 5.2.</b> Block diagram of the system for evaluating the transfer function of a filter	88

	Page
<b>Figure 5.3.</b> Magnitude of the transfer function of the anti-aliasing filter with cutoff frequency set at 10 Hz	90
<b>Figure 5.4.</b> The phase characteristics of the anti-aliasing filter	91
<b>Figure 5.5.</b> APSD of the reactor at one watt, ob- served at detector A	92
<b>Figure 5.6.</b> APSD for run 1-4-33 before the pump's harmonics were removed	94
<b>Figure 5.7.</b> APSD for run 1-4-33 after the pump's harmonics were removed	95
<b>Figure 6.1.</b> The measured APSD's, in stagnant water, for run 1-3-22	100
<b>Figure 6.2.</b> The measured APSD's, in stagnant water, for run 1-3-23	102
<b>Figure 6.3.</b> The measured APSD's, for forced circulation, for run 1-4-34	103
<b>Figure 6.4.</b> The measured APSD's, for forced circulation, for run 1-4-26	104
<b>Figure 6.5.</b> The measured APSD's, for forced circulation, for run 1-4-33	105
<b>Figure 6.6.</b> Comparison between the APSD's, for forced circulation, with and without void generation	106
<b>Figure 6.7.</b> APSD's for predominantly bubbly flow at various water and gas flow rates	108
<b>Figure 6.8.</b> APSD's for predominantly slug flow at various water and gas flow rates	109
<b>Figure 6.9.</b> APSD's for slug flow as observed near the test section, detector B, and inside the south reflector of the UTR-10 reactor, detector A	111

	Page
<b>Figure 6.10.</b> Theoretical APSD's for slug flow at various void velocities	113
<b>Figure 6.11.</b> The peak position from the experimental and theoretical APSD's for different void velocities	114
<b>Figure 6.12.</b> The magnitude and phase of the CPSD for run 1-3-23	116
<b>Figure 6.13.</b> The magnitude of a typical CPSD calculation in the UTR-10 between two positions along the test section, 12 cm apart	117
<b>Figure 6.14.</b> The phase angle of a typical CPSD calculation in the UTR-10 between two positions along the test section, 12 cm apart	118
<b>Figure B.1.</b> Schematic cross-sectional diagram for the UTR-10 reactor (all units are in centimeters)	155
<b>Figure B.2.</b> Fast and thermal flux distribution along the Z-axis crossing the internal graphite reflector region	159
<b>Figure B.3.</b> Fast and thermal flux distribution along the Z-axis ( $X = 23.6$ , $y = 0$ ) crossing the fuel and water regions	160
<b>Figure B.4.</b> Fast and thermal flux distribution along the X-axis ( $Z = 19.6$ , $y = 0$ ) crossing the internal graphite, fuel and graphite reflector regions	161
<b>Figure B.5.</b> A comparison between the adjoint response's magnitude for the 1-D CRAM solution and the exact Green's solution	162
<b>Figure B.6.</b> A comparison between the adjoint response's phase for the 1-D CRAM solution and the exact Green's solution	163
<b>Figure B.7.</b> The magnitude of the thermal adjoint functions along the Z-axis ( $x = y = 0$ )	167

	Page
Figure B.8. The phase of the thermal adjoint functions along the Z-axis ( $x = y = 0$ )	168
Figure B.9. The magnitude of the UTR-10 reactor response for various source locations along the Z-axis ( $x = y = 0$ )	169
Figure B.10. The phase of the UTR-10 reactor response for various source locations along the Z-axis ( $x = y = 0$ )	170
Figure B.11. A schematic of a two-dimensional reactor (illustrating the zone and channel concepts)	172
Figure C.1. Schematic flow diagram of the SOURCE code	184
Figure C.2. APSD's due to void fluctuations for completely coherent sources	186
Figure C.3. APSD's due to void fluctuations for exponentially coherent sources	187
Figure C.4. APSD's due to void fluctuations for uncorrelated sources	188
Figure C.5. The magnitude of the CPSD's due to void fluctuations for different space correlation dependence	189
Figure C.6. The phase angle of the CPSD's due to void fluctuations for different space correlation dependence	190

## I. INTRODUCTION

The characteristics of two-phase flow are a very important subject of study and a great deal of work has been done to map the different flow patterns and the boundaries between them. Although the descriptive terms applied to various two-phase regimes vary from author to author, there are basic patterns which have been described as follows [121]

- 1 - Bubbly flow, in which distinct bubbles are dispersed in a continuous flow of liquid
- 2 - Slug flow which is characterized by a series of individual large bubbles which almost fill the available flow cross section
- 3 - Churn turbulent which represents a transition region between bubbly flow and slug flow. This regime is characterized by significant bubble break-up and coalescence
- 4 - Annular flow, in which a continuous liquid film flows along the wall of a pipe while the gas flows in a central "core"
- 5 - Misty flow, in which the discrete liquid droplets are entrained in a continuous gas phase.

In a BWR reactor, the two-phase flow patterns play a critical role in the safe and optimum operation of the plant. Fluctuation of the local steam content in the cooling channels takes place due to generation and transport of discrete bubbles. These fluctuations in steam content affect the moderator density and hence the nuclear parameters, which in turn induce variations in the local neutron flux. This is the essential source of neutron noise in this type of reactor.

By virtue of its origin, this noise source contains such important information as the steam's void fraction and its velocity. Consequently, neutron noise measurements in BWR reactors can provide such information. Several models were proposed to aid in the interpretation process. A model that enjoys wide acceptance is based on the local-global concept [120]. Here the global component of the noise was assumed to be the reactivity noise, which is partly caused by the steam bubbles, while the local effect was interpreted as the flux changes in the vicinity of the steam bubbles.

Recently it was reported in the literature [61] that the local component of voids generates a spectral pattern in the 30-40 Hz range, which is much higher than all the known characteristic frequencies relevant to reactor noise investigations (e.g. neutronic, temperature, flow and pressure noise sources). An earlier investigation [74] indicated that the magnitude of the neutron fluctuations are largely determined by the bubble sizes. Accordingly it should be possible using two or more detectors to distinguish by means of local neutron noise measurement between a channel in which bubbly flow is occurring and one in which slug flow is occurring. If bubbly flow occurs in portions of a channel followed by slug flow, this also should be easily identifiable, as would be the case if annular flow follows slug flow. On the other hand, the void fluctuations from fully established annular flow is generally small and it follows that the probability of distinguishing between

bubbly flow and annular flow is not expected to be high. As a consequence of the above argument, it is reasonable to assume that the void generated noise will give a signature that uniquely characterizes some of the distinct flow regimes outlined above.

The aims of this investigation are two-fold:

- a) To demonstrate the possibility of characterizing different flow regimes by their spectral density signatures.
- b) To investigate the detection and possible identification of flow pattern changes.

To this end an experimental loop was installed in the vertical central stringer of the University Training Reactor (UTR-10). The design of the loop provides for a test section with an abrupt diameter change that simulates a blockage in a reactor coolant channel. This abrupt change in flow conditions will promote the development of a flow pattern transition, i.e. from bubbly to slug flow, etc. The loop may be operated at different water flow rates and has provision for the controlled introduction of voids in the form of purified nitrogen bubbles. Two neutron detectors are incorporated to study two phase flow patterns.

An identical out of pile loop was used to visually observe, record on film and categorize the two-phase flow patterns along the test section. This arrangement helps to identify the measured spectra with a given flow pattern.

In order to develop proper understanding and explanation of the phenomena, experimental work was supported by a theoretical treatment that combines the stochastics of voids with a two-dimensional two-group neutronic model of the reactor response.

## II. LITERATURE REVIEW

The identification of flow patterns in a BWR using neutron noise techniques requires a review of the theoretical and experimental areas relevant to input neutron noise sources, two phase flow and at-power void fluctuations in reactor cores.

The historical development of the detection of boiling noise in Light Water Reactors (LWR) has been reported extensively in the literature [2-10, 16-17, 91, 98, 114].

The first generalized noise model, driven by reactivity variations, was developed by Seifritz [104]. This model produced a transfer function relating random processes to reactivity driving functions.

### A. Input Noise Sources in Nuclear Reactors

The random birth and death processes of neutrons and precursors contribute to what is normally termed the "intrinsic noise" source or input noise source in zero power reactors. The characteristics of this source were postulated and later verified experimentally to be Gaussian white noise, where the term white noise describes the fact that the power spectral density of the noise is flat over the entire frequency range. Cohn [22] applied the Schottky formula to calculate its strength. However, Griffin and Randall [43] and Utsuro and Shibata [119] observed that as the reactor is operated at progressively higher power levels, the intrinsic noise source

begins to deviate more and more from that of a white source. The deviation was particularly pronounced in the low frequency region of less than one Hertz. To alleviate this discrepancy, Sheff and Albrecht [108] developed a space dependent stochastic model using the Langevin technique to evaluate the correlation function of "equivalent noise" sources. They concluded that when delayed neutron effects are included, the input noise sources are not white. In a somewhat heuristic way, they derived a frequency dependent noise source. Saito [88, 89] approached the problem of describing the noise equivalent source by assuming that the macrostochastic variables characterizing the state of the nuclear reactor follow a Markoffian random process. Using the generalized Schottky formula, he obtained an expression for the frequency dependent noise equivalent source which is very similar to that derived by Sheff and Albrecht [108]. The delayed neutron component was treated as a feedback to the neutron field while in [108] it is taken as an independent state variable. In an effort to evaluate the equivalent noise source under more realistic conditions, Saito [90] included a fuel to coolant temperature feedback component. An expression for the equivalent noise source was obtained which revealed a roll-off that is determined by the mean relaxation time constant of the fuel temperature feedback. The at-power reactor noise was examined by Saito [90, 92] and more recently by Matthey [71] who included in his model

a two-phase coolant. Saito concluded that random birth and death processes of neutrons contribute a white noise component to the input source, while the temperature feedback loops, fuel and coolant, contribute a frequency dependent noise which has a roll-off that is determined by the joint relaxation time constants of the fuel and coolant reactivity feedback effects. He further concluded that the nonwhite component becomes predominant at a high power level. Matthey [71], using his model, reached similar conclusions except for the roll-off frequency of the equivalent noise source which now depends on the three relaxation time constants associated with the liquid phase, vapor phase and the fuel feedback coefficients. He also pointed out that both the shape and magnitude of the input noise source depends on the ratio of the quantized thermal energy released by fission to that from steam condensation.

#### B. Stochastics of Two-Phase Flow in A Reactor Coolant Channel

In nuclear reactors the formation of vapor bubbles on the walls of the channels and their motion into the liquid, followed by their growth, detachment or collapse has a profound effect upon the reactor performance. In normal operation the liquid in the heated channels is in turbulent motion. Furthermore, if the bubbles present are large, their motion will perhaps introduce a form of turbulence that will add to the liquid turbulence already present. Different size bubbles suspended in a liquid will have distinct velocities and under

turbulent conditions, a phenomenon known as coalescence also occurs.

Two-phase flow may assume distinct geometrical configurations or what are normally referred to as regimes. In a typical BWR reactor, the basic sequence of the flow patterns have the characteristics displayed in Figure 2.1. The flow is diabatic [20, 53] since the flow patterns are sequentially being developed as the flow progresses up the coolant channel.

Excellent summaries of the status of knowledge of boiling heat transfer have been reviewed by Wallis [121], Hsu and Graham [53], Boure et al. [18] and more recently by Lahey and Moody [62] who dealt exclusively with the thermal hydraulic aspects of boiling water reactors.

Houghton [51,52] presented a theoretical model to predict the void profile in vertical heated channels. He treated the bubble as a free particle suspended in turbulent liquid and assumed its motion to be Brownian. In analogy with the problem of the Brownian motion of submicroscopic particles in an external field, he applied the Einstein-Smoluchowski technique by replacing the molecular motion by the corresponding eddying motion of the liquid. The resulting continuity and heat balance equations were then linearized and numerically solved to yield the void fraction profile. A generalized voids model was proposed by Sha [107] which showed that Houghton's model [51] is a special case. The

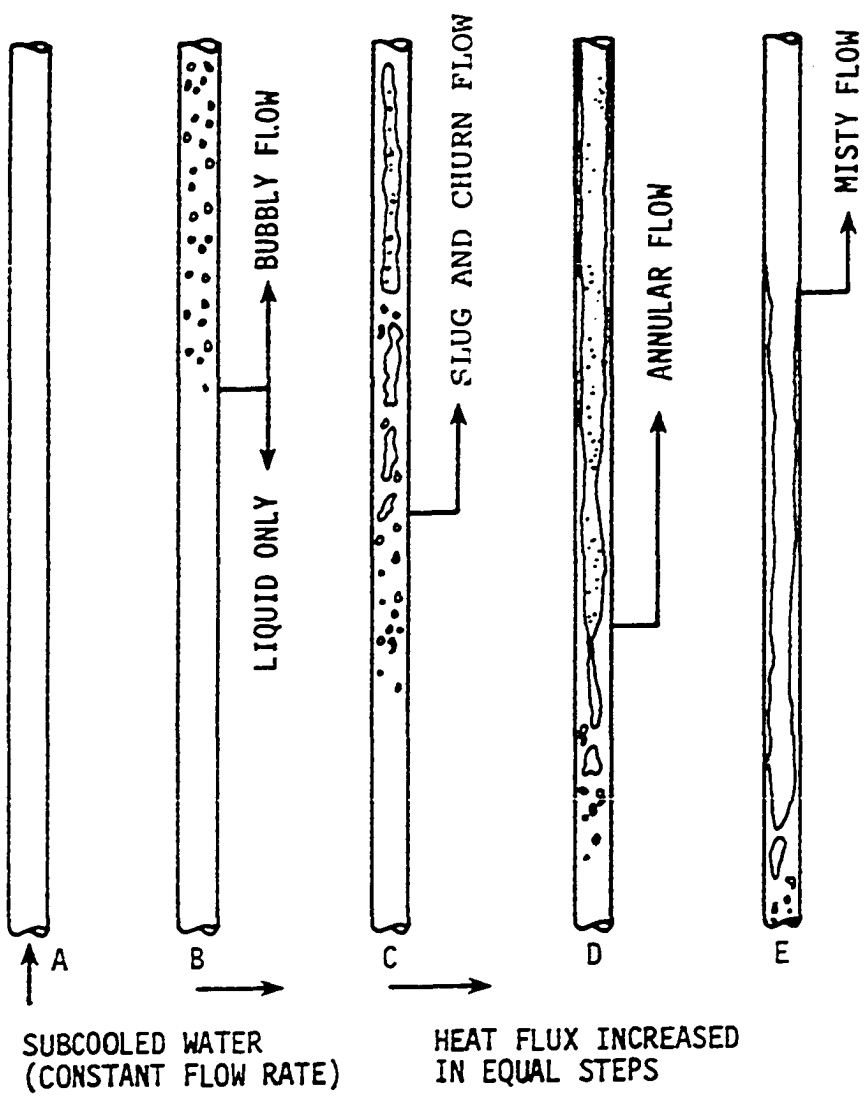


Figure 2.1. Diabatic flow regimes [62]

model treated bubbles as free particles and used the continuity and heat balance equations to compute both the axial and radial void distributions in a light-water-moderated reactor channel. The calculation algorithm is well-suited for computer programming. It can be used to explicitly and simultaneously evaluate the heat and mass balances as well as voids profiles. The model also allows for several parameters to be adjusted as empirical or better experimental data become available.

Singh and Stegemann [110] and Gebureck et al. [38] developed a stochastic void model based on the solution of the two-phase mass and energy balance equations. The analytical model allowed for random fluctuations in the velocity of the liquid and the axial void fraction. The model incorporated the space correlation of the noise sources. Three cases were examined, namely, noise sources completely uncorrelated, completely correlated, or exponentially correlated. The assumption of exponentially coherent sources agreed more closely with experiments.

Nomura [78] adopted the notion of discrete bubble formation in his model and arrived at a stochastic solution of the void fraction by using the mass and energy balance equations for two-phase flow. Although the model neglected feedback due to void generation, it provided for temperature and pressure feedback effects.

The model transformed the white input heat source into a band limited reactivity input which drove the reactor closed loop transfer function. The calculated power spectral density (PSD) compared sufficiently well to the measured PSD's to warrant further studies.

#### C. Theoretical and Experimental Investigations of Void Fluctuations in Nuclear Reactors

The importance of the effect of steam bubbles formation, detachment and transport on the reactivity, power density profile and hydrodynamic behavior of a water moderated reactor has long been recognized. However, the mechanisms of steam-bubble formation and collapse are complex phenomena that are not well-understood. This is chiefly due to the stochastic nature of these phenomena, which incidentally, provides a strong and predominant noise source in boiling water reactors. Study of this noise source can, in principle, reveal such important system parameters as steam velocity, void fraction and even thermal hydraulic instabilities.

In recent years, much work has been carried out in this field [27-33, 41-42, 48, 69, 93, 95, 109] but the earliest investigation of void fluctuations and measurement was carried out by Boyd [19] in 1959. He detected the onset of boiling in a nuclear reactor. An electrically heated ribbon wrapped around an ion-chamber, placed inside a research reactor, was used to produce local boiling. Measurements showed a distinct

and consistent increase of noise signal as the power from the heater was increased. Colomb and Binford [24] put a heater inside a reactor to produce boiling. They were able to detect some acoustical signal but the results were more qualitative and rather inconclusive.

In analyzing the noise spectra from a PWR, Rajagopal [85] observed a resonance peak between 10 and 20 Hz that was attributed to the onset of boiling. Thie [115] reported the results of noise measurement at the Pathfinder Nuclear Power Plant. The results indicated that the noise level, for frequencies higher than .5 Hz, consistently increased as the detector was moved to a higher position in the core. This trend was attributed to increased boiling. Seifritz [105] observed the spectra from the Lingen BWR using in-core self-powered neutron detectors. The spectra exhibited a low pass filter characteristic in the lower part of the core which changed to a band pass filter characteristic in the middle and upper parts of the reactor. It was also noted that the relative root mean square of the noise signal progressively increased as the detector was moved to a higher position in the core. The first void speed measurements in a BWR were reported by Seifritz and Cioli [106]. They observed that the phase lag between two axially placed detectors was a linear function of frequency. They also noted an enhancement in the noise spectra, over the frequency region of 1 to 10 Hz, as the detector was moved to a higher position in the core.

In an attempt to interpret these findings, Wach and Kosaly [120] proposed a phenomenological model that postulated the existence of local and global driving noise sources. The joint effect on the structures of the auto and cross-spectral densities were derived. The model revealed that void speed information is contained in the local component of the noise field and that any such measurement is only possible if the local component dominates over the global component. In order to substantiate the idea of a two component noise field, Behringer et al.[10] presented a theoretical stochastic model based on the one-dimensional, two-group diffusion equations. The model was successful in resolving the noise field into two components with distinct relaxation lengths that can readily be associated with the local and global components observed earlier [120]. Analytis [4] managed to decouple the reactor noise field into a global and a local component by using the one-dimensional diffusion equation with an appropriate slowing down kernel. The linearized stochastic equations were solved for a homogeneous unreflected core by the method of Green's Function. Kosaly and Mesko [59] studied the effect of finite detector size on the observed spectra and postulated the existence of a finite volume of sensitivity associated with the detector. Noise spectra were developed by introducing a relaxation length for the effect of the local perturbation and by integrating the point model response

over the length of the detector. Rothman [87] used the collision probability approach and the Langevin technique to evaluate the noise field in a BWR. He treated the neutron noise as arising from random local fluctuation of voids. The effect of detector size on the measured spectra was qualitatively presented. Huang [54] examined the detector sensitivity to a localized noise source of bubbles in a research reactor. His modeling of the detector response was based on the adjoint formulation of the neutron field in frequency space. This formulation was simplified by expressing the adjoint fluxes as the sum of a real and an imaginary component, thereby transforming the adjoint equation into two coupled equations. The coupling was removed when the frequency range was restricted to the plateau region of the zero power transfer function of the reactor. A three dimensional-two group static code was then applied twice in succession to evaluate the real and imaginary components of the adjoint function. The model compared well with the measurements in predicting the sensitivity of the detector to a local voidage noise source. The volume of sensitivity of the detector was estimated to be a sphere of about 8 cm in radius.

To study the local component of bubble noise, Nabavian [77] employed a loop inside the thermal column of a research reactor. His findings indicated that the amplitude of the auto spectral density of the noise showed strong dependence

on air flow rates around one Hertz. Recently, Kosaly et al. [60] studied the noise patterns from the Huhleberg BWR. Measurements were reported for spectra below 10 Hz and in the range 4-50 Hz. The phase lag between two incore detectors were found to be linear with frequency as predicted [59]. However, at high frequencies the data from the upper part of the core indicated the existence of what may be a second transit time. All the noise spectra showed a predominant peak in the range of 20-30 Hz which was attributed to void fluctuation. The effects of bubble size and void fraction on the measured spectra were examined by Mogil'ner [74]. He assumed the neutron noise to be composed of two parts: the inherent noise of gas bubbles and that induced by pressure fluctuations. In this model, the inherent noise was treated as shot noise and hence was assumed white. The presence of gas bubbles causes local pressure fluctuations that lead to additional reactivity fluctuations. By comparing his model to experiments it was possible to deduce the void fraction and the average volume of the bubble. Morishima [75] developed a working set of equations that deals with the transport processes of nuclear, thermal and hydraulic quantities. The set of Markoffian equations and the moment equations were used to derive an expression for the noise spectrum so that a comparison could be made with measurements. It was concluded that the derived spectrum displayed the low frequency

behavior that characterized the measurements of Griffin and Randall [43].

Time dependent perturbation theory was applied by Dam [27-29] to compute the detector frequency response to void fluctuations in a BWR. The derived response was to be, chiefly, composed of two components. The first stems from fluctuations in the fast absorption cross section, which is weighted by the magnitude of the fast flux squared, and hence is detected on a global scale. The second stems from fluctuations in the moderation cross section, which is weighted by the difference of the fast and thermal adjoint functions. Since this difference was shown to exhibit a strong local peaking near the detector, it was concluded that the second component represents the local component of the detector response. In an attempt to verify the validity of the above model, Kleiss and Dam [57] simulated a BWR by injecting air bubbles into the water moderator of a subcritical assembly. A neutron source and a neutron detector were present in the system. The influence of the bubbles on the detector response was measured using an average-response technique. These measurements confirmed the validity of the model developed by Kleiss and Dam [57]. The average response technique was originally developed by Fuge and Valko [37] who first used it to study the individual components that make up the detector response. By analyzing the signal in the time domain, they

were able to infer the spatial relaxation length of the local bubble disturbance in water, which is comparable to the neutron diffusion length in the same medium. Matthey [71] demonstrated the possibility of using a zero power reactor to study void fluctuations in a BWR. In order to simulate heat transfer and steam void fluctuations in a BWR, he used a research reactor and a bubble feedback mechanism. He found that the noise spectra exhibited a resonance peak which tended to be shifted to higher frequency as the reactor power was increased. This behavior is similar to that observed in a BWR operating at a high power level [113].

It is clear from the references cited that noise measurements due to void generation can be used to provide information on system performance without the need to apply external perturbations to the system. It is desirable to use noise measurements as a tool to monitor and characterize, on a continuous basis, the flow regimes in a reactor coolant channel.

Since the heat, mass, and momentum transfer characteristics depend on the flow regimes [20, 62, 85], it may be possible to detect undesirable core operating conditions and approach to safety margins from these measurements. This possibility accounts in part for the intense interest in noise measurements in power reactors.

### III. THEORY

#### A. Evaluation of the Input Noise Source to Void Fluctuations

The input noise sources from two-phase flow in a channel are considered. A stochastic point model will be developed using the transition probability approach [88]. This method relies on a suitable choice of state variables that best describe the system. It further requires that the stochastic components of this vector be Markoffian in character with zero mean. Briefly stated, the method describes the relevant phenomenon by a set of elementary processes or events, whereby for each of the events, the net change in the state vector is evaluated. This procedure generates a table of events with appropriate entries of the rate of occurrence for each of the elementary processes. Using this table, the first two moments of the state vector are calculated. By applying the Langevin technique to the first order moment, the linearized system of equations will yield the relaxation matrix. The combined knowledge of the relaxation matrix, which characterizes the dynamics of the system, with the second order moments will lead to the evaluation of the cross power spectral density of the noise sources.

The flow channel used in this study is shown in Figures 4.2 and 4.3. Since the two phases considered are water and nitrogen gas, the problems of bubble collapse and heat transfer events will not be included. Flow and voidage

fluctuations may arise as a result of any of the following processes

- (a) Random momentum exchange between the two flow components, for instance through bubble coalescence, bubble break up and friction exchanges.
- (b) Random introduction of discrete bubbles or an aggregate of bubbles through the channel entrance.
- (c) Random leakage of discrete bubbles or an aggregate of bubbles through the exit of the channel.

### 1. Table of events

The dynamics of the flow may be described through the state vector  $\underline{x}$ , defined as

$$\underline{x} = [M_g \ M_l \ P_g \ P_l]^T, \quad (3-1)$$

where

$M_g$  = Total mass of the gas phase in the channel

$M_l$  = Total mass of the liquid phase in the channel

$P_g$  = Net momentum of the gas phase in the channel

$P_l$  = Net momentum of the liquid phase in the channel.

In order to introduce the various kinds of elementary events that take place in the system, it is helpful to define some additional terms, let

$S_l, S_g$  = Liquid mass flow rate in gm/sec and the number of bubbles/sec entering the system respectively

$\lambda_i$  = Probability per unit time that a momentum transfer event occurred in phase i

$\lambda_{ri}$  = Probability per unit time that phase i is removed from the channel exit

$P(\mu_i)$  = Probability that  $\mu$  momentum is exchanged with phase  $i$  through coalescence, break up or an internal friction event

$P(K,V)$  = The joint probability that a bubble of  $K$  volume and velocity  $V$  is introduced at the input stream

$P(\mu,V)$  = The joint probability that a liquid of mass  $\mu$  and velocity  $V$  escaped through the channel exit.

Now it is possible to construct Table 3.1 of the elementary events that are taking place in the proposed channel. Such a table will be used later to evaluate the first two moments of the state vector [92].

## 2. The first order moment equations

Assume that the state vector  $X$  is composed of a steady state component plus a fluctuating component that is Markoffian in character with zero mean. Then according to Lax's theory [64], the determination of the first order moments of the stochastic variables can be accomplished solely through the use of Table 3.1. The results are as follows

$$D_1(M_g) = \langle S_g \rho_g K_i P(K_i, V_{ig}) - \lambda_{rg} M_g \mu_{rg} P(\mu_{rg}, V_g) \rangle \quad (3-2a)$$

$$D_1(M_\ell) = \langle S_\ell - \lambda_{r\ell} M_\ell \mu_{r\ell} P(\mu_{r\ell}, V_\ell) \rangle \quad (3-2b)$$

$$\begin{aligned} D_1(P_g) &= \langle S_g \rho_g K_i V_{ig} P(K_i, V_{ig}) - \lambda_g P_g \mu_g P(\mu_g) \\ &\quad + \lambda_\ell P_\ell \mu_\ell P(\mu_\ell) - \lambda_{rg} M_g \mu_{rg} V_g P(\mu_{rg}, V_g) \rangle \quad (3-2c) \end{aligned}$$

$$\begin{aligned} D_1(P_\ell) &= \langle S_\ell V_i + \lambda_g P_g \mu_g P(\mu_g) - \lambda_\ell P_\ell \mu_\ell P(\mu_\ell) \\ &\quad - \lambda_{r\ell} M_\ell \mu_{r\ell} V_\ell P(\mu_{r\ell}, V_\ell) \rangle, \quad (3-2d) \end{aligned}$$

where the notation  $\langle f \rangle$  stand for the ensemble average and  $D_1(X)$  is the first order moment of the state variable  $X$  over all members of the ensemble initially in the state  $f$ .

Taking the ensemble averages of Equation (3-2), the result in matrix notation is

$$\underline{D}_1(\underline{X}) = \underline{B} \underline{X} + \underline{S}, \quad (3-3)$$

where

$$\begin{aligned} \underline{S} &= [S_{rg} \rho_g \langle K_i \rangle \ S_{rl} \ S_{rg} \rho_g \langle K_i V_{ig} \rangle \ S_{rl} \langle V_i \rangle]^T \\ \underline{B} &= \begin{bmatrix} -\lambda_{rg} \langle u_{rg} \rangle & 0 & 0 & 0 \\ 0 & -\lambda_{rl} \langle u_{rl} \rangle & 0 & 0 \\ -\lambda_{rg} \langle u_{rg} V_g \rangle & 0 & -\lambda_g \langle u_g \rangle & \lambda_l \langle u_l \rangle \\ 0 & -\lambda_{rl} \langle u_{rl} V_l \rangle & \lambda_g \langle u_g \rangle & -\lambda_l \langle u_l \rangle \end{bmatrix} \end{aligned} \quad (3-4)$$

The somewhat artificial parameters introduced earlier to describe the various transition probabilities can now be evaluated in terms of the more conventional quantities that are normally encountered in the literature of two-phase flow. This can be more easily accomplished by noting that the first order moments for the steady state are equal to zero and hence from Equation (3-3)

$$\underline{B} \underline{X}_0 + \underline{S} = \underline{0}, \quad (3-5)$$

where

$\underline{0}$  is the (4x1) null vector and the subscript zero implies steady state.

Conventional mass balance considerations for the gas and liquid phase, in the steady state, yield

$$S_g \rho_g \langle K_i \rangle - \frac{M_g}{\tau_g} = 0 \quad (3-6a)$$

$$S_\ell - \frac{M_\ell}{\tau_\ell} = 0 , \quad (3-6b)$$

where  $\tau_i$  is the transit time in seconds, of phase  $i$  through the channel.

Similarly, from the momentum balance equation for the gas phase, in the steady state, one gets

$$S_g \rho_g \langle K_i V_{ig} \rangle - \frac{M_g \langle V_g \rangle}{\tau_g} = \text{Friction loss.} \quad (3-6c)$$

The friction loss cannot be calculated rigorously, but several empirical expressions are available in the literature.

If the flow regime is either bubbly or churn flow, then according to Wallis [121], the friction loss is given by

$$- \left( \frac{\partial P}{\partial Z} \right) = 2C_f (\rho_g J_g + \rho_\ell J_\ell) (J_g + J_\ell) / D , \quad (3-7)$$

where

$C_f$  = friction factor with the wall of the channel

$D$  = equivalent channel diameter, cm =  $4 \times \text{area/perimeter}$

$J_g$  = volumetric flux of the gas phase, cm/sec =  $\alpha \langle V_g \rangle$

$J_\ell$  = volumetric flux of the liquid phase, cm/sec  
 $= (1-\alpha) \langle V_\ell \rangle$ .

Substituting the definitions of the  $J_i$ 's into Equation (3-7),

Table 3.1. Stochastic processes and change of state induced in the test channel

Nature of elementary events	Rate of occurrence	$M_g$	$M_\ell$	$P_g$	$P_\ell$
Liquid phase source	$S_\ell$	0	1	0	$v_i$
Gas phase source	$S_g P(K_i, v_{ig})$	$\rho_g K_i$	0	$\rho_g K_i v_{ig}$	0
Momentum transfer to liquid phase	$\lambda_g P_g P(\mu_g)$	0	0	$-\mu_g$	$\mu_g$
Momentum transfer to gas phase	$\lambda_\ell P_\ell (P_{\mu_\ell})$	0	0	$\mu_\ell$	$-\mu_\ell$
Gas leakage through channel exit	$\lambda_{rg} M_g P(\mu_{rg}, v_g)$	$-\mu_{rg}$	0	$-\mu_{rg} v_g$	0
Liquid leakage through channel exit	$\lambda_{rl} M_\ell P(\mu_{rl}, v_\ell)$	0	$-\mu_{rl}$	0	$-\mu_{rl} v_\ell$

yields after simplifying and neglecting terms of order  $\rho_g/\rho_\ell$

$$-(\frac{\partial P}{\partial Z}) = \frac{C_f}{D} [\rho_\ell (1-\alpha) ((1-\alpha)v_\ell^2 + \alpha v_\ell v_g) + \rho_g \alpha (\alpha v_g^2)]. \quad (3-8)$$

The total friction loss along the channel can be obtained by introducing the following definitions

$$\bar{\alpha} = \frac{1}{H} \int_0^H \alpha(z) dz, \quad (3-9)$$

$$\bar{v}_i = \frac{1}{H} \int_0^H v_i(z) dz, \quad (3-10)$$

where  $H$  is the length of the channel in cm, consequently, the average pressure gradient can be immediately written from Equation (3-8) as

$$-(\frac{\partial \bar{P}}{\partial Z}) = \frac{C_f}{D} [\rho_\ell (1-\bar{\alpha}) ((1-\bar{\alpha})v_\ell^2 + \bar{\alpha} \bar{v}_\ell \bar{v}_g) + \rho_g \bar{\alpha} (\bar{v}_g^2)]. \quad (3-11)$$

Accordingly, the total friction loss is given by

$$\text{Friction loss} = - A \int_0^H (\frac{\partial P}{\partial Z}) dz = - A H (\frac{\partial \bar{P}}{\partial Z}). \quad (3-12)$$

By substituting Equation (3-11) into Equation (3-12) and noting that

$$\begin{aligned} M_g &= HA \rho_g \bar{\alpha} \\ M_\ell &= HA \rho_\ell (1-\bar{\alpha}) \\ P_g &= M_g \bar{v}_g \\ P_\ell &= M_\ell \bar{v}_\ell \end{aligned} \quad (3-13)$$

Equation (3-12) is reduced to

$$\text{Friction loss} = \frac{C_f}{D} [P_\ell ((1-\bar{\alpha})\bar{V}_\ell + \bar{\alpha}\bar{V}_g) + P_g \bar{\alpha}\bar{V}_g] . \quad (3-14)$$

Substituting this equation into Equation (3.6c) and omitting the bar from the averaged variables, yields

$$S_g \rho_a K V_{ig} - \frac{M_g V_g}{\tau_g} - \frac{C_f}{D} [P_\ell ((1-\alpha)V_\ell + \alpha V_g) + P_g \alpha V_g] = 0 . \quad (3-15)$$

Following the same procedure, the corresponding equation for the liquid phase is obtained in the following form

$$S_\ell V_i - \frac{M_\ell V_\ell}{\tau_\ell} + \frac{C_f}{D} [P_\ell ((1-\alpha)V_\ell + \alpha V_g) + P_g \alpha V_g] = 0 . \quad (3-16)$$

The system of Equations (3-6a), (3-6b), (3-15) and (3-16) are now rewritten in matrix form as

$$\underline{C} \underline{x}_o + \underline{s} = \underline{0} , \quad (3-17)$$

where

$$\underline{C} = \begin{bmatrix} -\frac{1}{\tau_g} & 0 & 0 & 0 \\ 0 & -\frac{1}{\tau_\ell} & 0 & 0 \\ -\frac{V_g}{\tau_g} & 0 & -\alpha V_g & -(1-\alpha)V_\ell - \alpha V_g \\ 0 & -\frac{V_\ell}{\tau_\ell} & \alpha V_g & (1-\alpha)V_\ell + \alpha V_g \end{bmatrix} . \quad (3-18)$$

It is interesting to note that the elements of this matrix are expressed in terms of the conventional constants normally associated with describing two-phase flow. Furthermore, it should be noted that Equations (3-5) and (3-17) are equivalent.

Accordingly from now on, the matrix C will replace the matrix B throughout. Equation (3-7) which represents the first order moments is rewritten as

$$D_1(\underline{X}) = \underline{C} \underline{X} + \underline{S} . \quad (3-19)$$

### 3. Relaxation matrix

The first moment Equation (3-19) is now linearized by letting

$$\underline{X} = \underline{X}_0 + \delta \underline{X} . \quad (3-20)$$

Substituting the above equation into Equation (3-19), subtracting the steady state and neglecting second order terms, gives

$$D_1(\delta \underline{X}) = \underline{C} \delta \underline{X} . \quad (3-21)$$

This is equivalent to the following equation [72]

$$\frac{\partial}{\partial t} (\delta \underline{X}) - \underline{C} \delta \underline{X} = \underline{0} . \quad (3-22)$$

In the state variable formulation, the negative of the matrix C is normally referred to as the response or relaxation matrix [90]. Defining the response matrix R as

$$\underline{R} = - \underline{C} , \quad (3-23)$$

Equation (3-22) is now rewritten as

$$\frac{\partial}{\partial t} (\delta \underline{X}) + \underline{R} \delta \underline{X} = \underline{0} . \quad (3-24)$$

#### 4. Diffusion matrix

According to Saito [93] and Matthey [72], the components of the second order moment are the elements of the diffusion matrix. The diffusion matrix can be readily obtained from the application of the generalized Schottky formula and Table 3.1. This formula states that the noise cross spectral matrix, or the diffusion matrix is given by [88]

$$2 D_{ij} = \sum_k \langle q_k^i q_k^j p_{ij}^k \rangle , \quad (3-25)$$

where

$q_k^n$  is the net increase in the stochastic variable n during an event of type K

$p_{ij}^k$  is the joint probability density per unit time that the event K contributes a net increase to the stochastic variables i and j simultaneously.

Applying Equation (3-25) to Table (3.1), the following elements of the diffusion matrix are obtained (note that  $S$  and  $S_g$  are eliminated entirely from the following equations through the use of Equation (3-5))

$$\begin{aligned} 2D_{11} &= (\rho_g K \mu_{rg} \lambda_{rg} + \mu_{rg}^2) M_g \\ 2D_{13} &= 2D_{31} = (\rho_g K V_{i2} \mu_{rg} \lambda_{rg} + \mu_{rg} V_g \lambda_{rg}) M_g \\ 2D_{22} &= (\mu_{rl} + \mu_{rl}^2) \lambda_{rl} M_l \\ 2D_{24} &= 2D_{42} = (\mu_{rl} V_{il} + \mu_{rl}^2 V_l) \lambda_{rl} M_l \\ 2D_{33} &= (\rho_g \mu_{rg} K V_{i2} + \mu_{rg} V_g^2) \lambda_{rg} M_g + \mu_g^2 \lambda_g M_g + \mu_l^2 \lambda_l M_l \end{aligned} \quad (3-26)$$

$$\begin{aligned}
 2D_{34} &= 2D_{43} = \mu_g^2 \lambda_g P_g - \mu_\ell^2 \lambda_\ell P_\ell \\
 2D_{44} &= (\mu_{rl} v_{il}^2 + \mu_{rl}^2 v_\ell^2) \lambda_{rl} M_\ell + \mu_g^2 \lambda_g P_g + \mu_\ell^2 \lambda_\ell P_\ell \quad (3-26) \\
 2D_{12} &= 2D_{21} = 2D_{14} = 2D_{41} = 2D_{23} = 2D_{32} = 0 ,
 \end{aligned}$$

where

$2D_{ij}$  = the second order moment between the  $i^{th}$  and  $j^{th}$  component of the state vector  $\underline{x} = [1 \ 2 \ 3 \ 4]$ .

Using Equation (3-17), the steady state vector  $\underline{x}_o$  is given by

$$\underline{x}_o = - \underline{C}^{-1} \underline{S} . \quad (3-27)$$

It is worth noting that the diffusion matrix is symmetric. This can be verified directly from its definition as given by Equation (3-25).

### 5. Impulse response of the channel

The impulse response is, by definition, related to the behavior of the system when excited by an impulse source. Since the stochastic behavior of the channel is represented by Equation (3-24), the impulse response can be evaluated from this equation by replacing the null matrix by an impulse source in the relevant state variable. Due to the fact that the primary objective of this study is to evaluate the voids noise source, then it is clear that the impulse source should be associated with the state variable  $M_g$ . Mathematically stated, Equation (3-24) now becomes

$$\frac{\partial}{\partial t} \delta \underline{x}(t) + \underline{R} \delta \underline{x}(t) = \delta(t) \underline{U} , \quad (3-28)$$

where

$\delta(t)$  = the Dirac delta function

$$\underline{U} = [1 \ 0 \ 0 \ 0]^T.$$

Applying the Laplace transform to Equation (3-28) and rearranging yields

$$\delta \underline{X}(s) = (s\underline{I} + \underline{R})^{-1} \underline{U} = \underline{Q} \underline{U}, \quad (3-29)$$

where

$$\begin{aligned} \underline{I} &= \text{The } (4 \times 4) \text{ unitary matrix and } s \text{ is the Laplace variable} \\ \underline{Q} &= (s\underline{I} + \underline{R})^{-1}. \end{aligned} \quad (3-30)$$

From the definition of the inverse of a matrix, it follows that

$$\underline{Q} = \frac{1}{|s\underline{I} + \underline{R}|} [C_{ij}], \quad (3-31)$$

where

$|A|$  = the determinant of matrix A

$C_{ij}$  = represent the cofactor of the matrix  $(s\underline{I} + \underline{R})^T$

Applying the definition of the cofactor, the  $C_{ij}$  elements are evaluated and are given below

$$C_{11} = (s + \mu_{rl}\lambda_{rl}) [(s + \mu_g\lambda_g)(s + \mu_\ell\lambda_\ell) - \mu_\ell\mu_g\lambda_\ell\lambda_g]$$

$$C_{22} = (s + \mu_{rg}\lambda_{rg}) [(s + \mu_g\lambda_g)(s + \mu_\ell\lambda_\ell) - \mu_\ell\mu_g\lambda_\ell\lambda_g] \quad (3-32)$$

$$C_{31} = -\mu_{rg}\nu_g\lambda_{rg}(s + \mu_{rl}\lambda_{rl})(s + \mu_\ell\lambda_\ell)$$

$$\begin{aligned}
 C_{32} &= - (s + \mu_{rg}\lambda_{rg}) \mu_\ell \lambda_\ell \lambda_{rl} \mu_{rl} v_\ell \\
 C_{33} &= (s + \mu_{rg}\lambda_{rg}) (s + \mu_{rl}\lambda_{rl}) (s + \mu_\ell \lambda_\ell) \\
 C_{34} &= (s + \mu_{rg}\lambda_{rg}) (s + \mu_{rl}\lambda_{rl}) \mu_\ell \lambda_\ell \\
 C_{41} &= - (s + \mu_{rl}\lambda_{rl}) \mu_{rg} v_g \lambda_{rg} \lambda_g \mu_g \\
 C_{42} &= - (s + \mu_{rg}\lambda_{rg}) (s + \mu_g\lambda_g) \lambda_{rl} \mu_{rl} v_\ell \\
 C_{43} &= (s + \mu_{rg}\lambda_{rg}) (s + \mu_{rl}\lambda_{rl}) \mu_g \lambda_g \\
 C_{44} &= (s + \mu_{rg}\lambda_{rg}) (s + \mu_{rl}\lambda_{rl}) (s + \mu_g\lambda_g) \\
 C_{12} = C_{13} = C_{14} = C_{21} = C_{23} = C_{24} &= 0 .
 \end{aligned} \tag{3-32}$$

Through the use of Equation (3-32), the cross spectral impulse response matrix [72] is obtained.

The impulse response to bubbles may be recognized as  $\delta X_i(s)$  and is given by

$$\delta X_i(s) = \sum_j Q_{ij} U_j \tag{3-33}$$

for  $j = 1, 2, \dots, 4$ .

According to Equations (3-31) – (3-32), Equation (3-33) gives

$$X_i(s) = Q_{11} = \frac{C_{11}}{|sI + R|} = \text{impulse response due to bubbles.} \tag{3-34}$$

## 6. Power spectral density and input noise source

The cross spectral density matrix (CSD) can now be written as [72]

$$\underline{P}(\omega) = \underline{Q}(s) 2\underline{D} \underline{Q}^T(-s) , \quad (3-35)$$

where  $\underline{P}$  is the CSD matrix and  $\omega$  is the frequency, rad/sec.

The main interest is in evaluating the first element of the matrix  $\underline{P}(\omega)$ , namely  $P_{11}(\omega)$ . This element represents the power spectral density (PSD) of the void fluctuations, and it follows from elementary matrix algebra that

$$P_{11}(\omega) = \sum_{ij} Q_{li} 2D_{ij} Q_{jl}^{*T} , \quad (3-36)$$

for  $i, j = 1, 2, \dots, 4$

where the (\*) stands for complex conjugation.

Performing the indicated operations in Equation (3-36) gives

$$P_{11}(\omega) = 2D_{11}|Q_{11}(s)|^2 . \quad (3-37)$$

Substituting Equations (3-36) and (3-34) in the above equation yields

$$P_{11}(\omega) = (\rho_g K_i \mu_{rg} \lambda_{rg} + \mu_{rg}^2 \lambda_{rg}) M_g |Q_{11}(s)|^2 . \quad (3-38)$$

Defining the input noise source due to bubbles as

$$I(\omega) = \frac{\text{output PSD}}{(\text{impulse response})^2} . \quad (3-39)$$

Then clearly, the input noise source is given by

$$I(\omega) = (\rho_g K_i \mu_{rg} \lambda_{rg} + \mu_{rg}^2 \lambda_{rg}) M_g . \quad (3-40)$$

Comparing the first element of matrices  $\underline{C}$  and  $\underline{B}$  (Equations (3-4) and (3-18)) gives

$$\frac{1}{\tau_g} = \mu_{rg} \lambda_{rg} \quad . \quad (3-41)$$

Substituting back into Equation (3-40) gives

$$I(\omega) = \frac{M_g}{\tau_g} (\rho_g K_i + \mu_{rg}) = V_g (\rho_g K_i + \mu_{rg}) \quad . \quad (3-42)$$

Since the R.H.S. of this equation is independent of the frequency, it is concluded that the input noise source due to bubbles is white in character.

Since the quantity in brackets is the mass of both the average bubbles entering plus the average bubbles leaving the channel, Equation (3-42) may be written as

$$I(\omega) = 2V_g \times (\text{average mass of the bubbles in the channel})$$

$$I(\omega) \sim V_g \quad (\text{average volume of the bubbles}) \quad . \quad (3-43)$$

The above form of the input noise source suggest that such measurements can give information about the average bubble size and velocity.

#### B. Two-phase Flow and its Associated Noise Sources

In this section, bubbles will be treated as discrete entities and may be regarded as free particles. The radial motion of the bubble is influenced by the random eddies of the turbulent liquid phase, while its axial motion is dictated by buoyancy and by the direction of the liquid flow in the channel. These effects give rise to a "velocity type" noise source. Another dominant noise source comes about from random events of

coalescence or break up of bubbles. These phenomena introduce a "void type" noise source. Both of these noise sources will be developed from basic considerations of mass and momentum balance.

The proposed channel is depicted schematically in Figure 3.1. It consists essentially of two annular sections. Bubbles of gas are injected at the base of the channel and a self-priming pump circulates the two-phase media. The two phases are separated at the reservoir and only the liquid phase is allowed to circulate back through the pump.

### 1. Development of the two-phase stochastic equation

For two phase flow, the mass and momentum continuity equations can be written in the following form [62, 121]

$$\frac{\partial}{\partial t} [\rho_1(1-\alpha) + \rho_2\alpha] + \nabla \cdot [\rho_1(1-\alpha)\mathbf{v}_1 + \rho_2\alpha\mathbf{v}_2] = S \quad (3-44)$$

$$\begin{aligned} \rho_1 \frac{\partial}{\partial t} \mathbf{v}_1 - \rho_2 \frac{\partial}{\partial t} \mathbf{v}_2 + \rho_1 \mathbf{v}_1 \nabla \mathbf{v}_1 - \rho_2 \mathbf{v}_2 \nabla \mathbf{v}_2 &= -g[(1-\alpha)\rho_1 - \rho_2\alpha] \\ &\quad - \nabla \cdot \mathbf{P} \end{aligned} \quad (3-45)$$

where  $\rho, \alpha, \mathbf{v}, g$  denote the density, void fraction, velocity and the gravity acceleration respectively. The subscript 1 and 2 refer to the liquid phase and the gas phase, respectively. The input gas source is denoted as  $S$ .  $Z$  and  $P$  refer to the axial position in the channel and to dynamic pressure at position  $z$ , respectively.

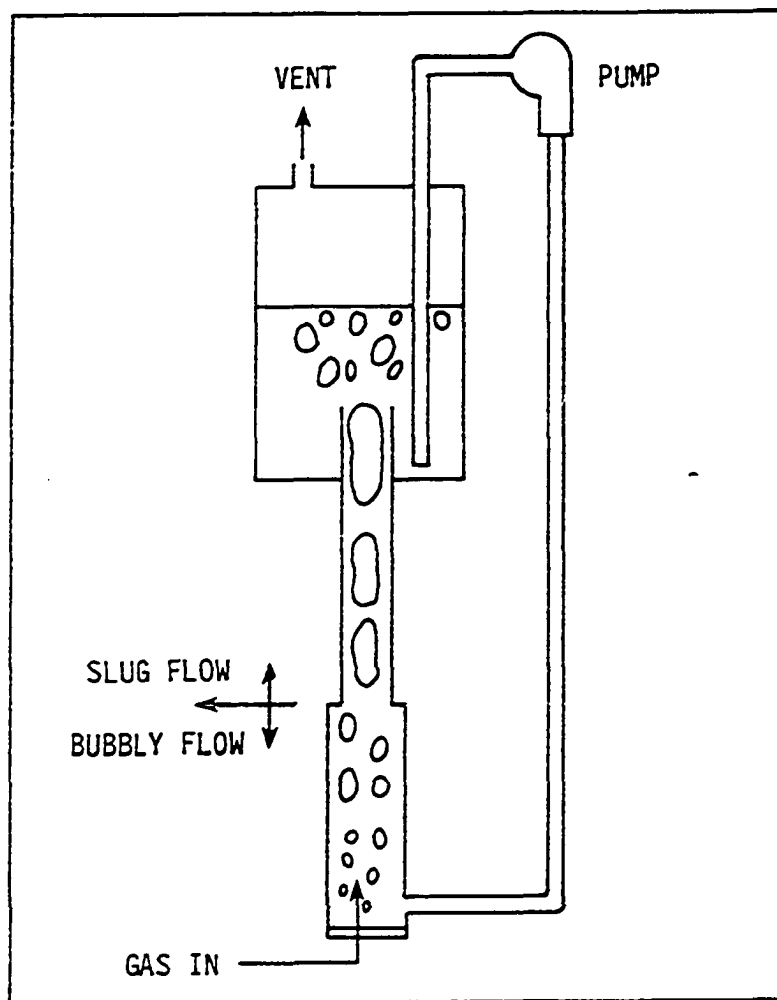


Figure 3.1. Schematic diagram of the test loop

To simplify the treatment, the following assumptions are introduced

- a. The flow is one dimensional and accordingly all the flow parameters are properly averaged over the radial region. Also the gradient terms are replaced by  $\frac{\partial}{\partial Z}$ .
- b. The liquid phase, namely water, is incompressible and consequently  $\rho_l$  is a constant.
- c. The variables  $\alpha$ ,  $V$  and  $P$  are functions of both time and space.

Applying these assumptions, Equations (3-44) and (3-45) are now reduced, after simplifying and rearranging to

$$-\rho \frac{\partial \alpha}{\partial t} + \rho(1-\alpha) \frac{\partial V}{\partial Z} - \rho V \frac{\partial \alpha}{\partial Z} = S. \quad (3-46)$$

$$\rho \frac{\partial V}{\partial t} + \rho V \frac{\partial V}{\partial Z} = -g(1-\alpha) - (\frac{\partial P}{\partial Z})_{\text{friction}}. \quad (3-47)$$

Note that all the subscripts are dropped since all the parameters refer to the liquid phase only.

The friction pressure gradient  $(\frac{\partial P}{\partial Z})_{\text{friction}}$  depends primarily on the type of flow in the channel. Using the drift flux model, the following expressions are obtained [121]:

For bubbly and churn flow

$$-(\frac{\partial P}{\partial Z})_{\text{friction}} = f(\alpha) = \frac{2C_f}{D} (\rho_1 J_1 + \rho_2 J_2) (J_1 + J_2), \quad (3-48)$$

where

$C_f$  = The empirical friction factor

$J_1$  = The volumetric flux of the liquid phase =  $(1-\alpha)V_1$

$J_2$  = The volumetric flux of the gas phase =  $\alpha V_1$

$D$  = The equivalent channel diameter.

and for slug flow

$$-(\frac{\partial P}{\partial Z}) = f(\alpha) = \frac{2C_f}{D}(1-\alpha)\rho_1(J_1+J_2)^2 . \quad (3-49)$$

Since the pressure gradient depends on  $v_1$  and  $v_2$ , it is more convenient to eliminate the  $v_2$  dependence. To this end, the following empirical relations are used

$$v_2 = rv_1 , \quad (3-50)$$

where  $r$  is the slip ratio which is related to the void fraction through [110]

$$r = \frac{1-\alpha}{k-\alpha} , \quad (3-51)$$

and where the parameter  $k$  depends on the pressure of the system in the following manner [62]

$$K = 0.71 + 10^{-4} P . \quad (3-52)$$

The value of  $K$  at the conditions of the channel is essentially a constant independent of pressure.

As was previously mentioned, the two dominant sources of noise in this system stem from random fluctuations in both the velocity and the void fraction. Expressing the time dependent variables as the sum of a steady state part plus a fluctuating part leads to

$$\begin{aligned} \alpha &= \bar{\alpha} + \delta\alpha \\ v &= \bar{v} + \delta v \\ r &= \bar{r} + \delta r \end{aligned} \quad (3-53)$$

Substituting Equation (3-53) into Equations (3-46) and (3-47),

subtracting the steady state and neglecting second order terms yield

$$\left( \frac{\partial}{\partial t} + \frac{\partial \bar{v}}{\partial z} \right) \delta \alpha - (1-\bar{\alpha}) \frac{\partial}{\partial z} (\delta v) + \delta v \frac{\partial \bar{\alpha}}{\partial z} + \bar{v} \frac{\partial}{\partial z} (\delta \alpha) = - \frac{\partial s}{\rho}, \quad (3-54)$$

$$\frac{\partial}{\partial t} (\delta v) + \bar{v} \frac{\partial}{\partial z} (\delta v) + \delta v \frac{\partial \bar{v}}{\partial z} = g \delta \alpha + \delta f(\alpha), \quad (3-55)$$

where for bubbly flow,  $\delta f(\alpha)$  is given by (omitting the bars over the variables  $\alpha$ ,  $v$  and  $r$  for notational convenience)

$$\begin{aligned} \delta f(\alpha) = & \frac{2C_f}{D} [v^2 (2\alpha(1-r)+r-2 - \frac{\alpha(1-\alpha)(1-r)}{k-\alpha}) \delta \alpha \\ & + 2v(\alpha^2(1-r)+\alpha(r-2)+1) \delta v] \end{aligned} \quad (3-56)$$

and for slug flow,  $\delta f(\alpha)$  is given by

$$\begin{aligned} \delta f(\alpha) = & \frac{4C_f}{D} [(v^2(1-\alpha)(1+\alpha(r-1))(\alpha \frac{r-1}{k-\alpha} + r-1) \\ & - \frac{v^2}{2}(1+\alpha(r-1))^2] \delta \alpha. \end{aligned} \quad (3-57)$$

Applying the above expressions for  $\delta f(\alpha)$  into Equation (3-55) results in

$$v \nabla \delta v + \left( \frac{\partial}{\partial t} + C_i \right) \delta v + D_i \delta \alpha = 0, \quad (3-58)$$

where  $i=1$  refers to bubbly flow,  $i=2$  refers to slug flow and

$$\begin{aligned} C_1 = & - \frac{2C_f}{D} [2v(\alpha^2(1-r)+\alpha(r-2)+1) + \nabla v \\ C_2 = & - \frac{4C_f v^2}{D} [(1-\alpha)(1+\alpha(r-1))(\alpha \frac{r-1}{k-\alpha} + r-1) - \frac{1}{2}(1+\alpha(r-1))^2] \\ & + \nabla v \end{aligned} \quad (3-59)$$

$$\begin{aligned} D_1 = & -g - \frac{2C_f v^2}{D} [2\alpha(1-r)+r-2 - \frac{\alpha(1-\alpha)(1-r)}{k-\alpha}] \\ D_2 = & -g - \frac{4C_f v^2}{D} [(1-\alpha)(1+\alpha(r-1))(\alpha \frac{r-1}{k-\alpha} + r-1) - \frac{1}{2}(1+\alpha(r-1))^2] \end{aligned}$$

Application of the Laplace transform to Equations (3-54) and (3-55), yields in matrix notation

$$\underline{A} \nabla_z \underline{X} + \underline{B}_i \underline{X} = \underline{S} \quad (3-60)$$

where

$$\underline{X} = [\delta v \ \delta a]^T \quad (3-61a)$$

$$\nabla_z = \frac{\partial}{\partial z} \quad (3-61b)$$

$$\underline{A} = \begin{pmatrix} \alpha^{-1} & v \\ v & 0 \end{pmatrix} \quad (3-62a)$$

$$\underline{B}_i = \begin{pmatrix} \nabla a & s + \nabla v \\ s + C_i & D_i \end{pmatrix} \quad (3-62b)$$

$$\underline{S} = [-\frac{\delta S}{\rho} \quad 0]^T \quad (3-63a)$$

$$s = \text{The Laplace variable} = j\omega. \quad (3-63b)$$

By matrix inversion, Equation (3-60) is reduced to the form

$$\nabla_z \underline{X} + \underline{A}^{-1} \underline{B}_i \underline{X} = \underline{A}^{-1} \underline{S}. \quad (3-64)$$

It should be noted that the  $i$  index refers to the type of flow regime and is defined by Equation (3-59).

Examination of Equation (3-60) reveals the following observations

- a. The elements of the matrices are a function of the steady state solution, which is in general space dependent.
- b. The diagonal elements of the matrix  $\underline{B}_i$  are real but the off diagonal elements are complex quantities and

depend on the steady state gradients of  $v$  and  $\alpha$ . Consequently, the steady state solution must be evaluated first before proceeding to solve the general stochastic equations.

## 2. Steady state solution

The steady state two-phase flow is completely described by Equations (3-46) and (3-47) when the time derivatives are set to zero. In matrix notation, the result is

$$\underline{A}^O \nabla_z \underline{x}^O = \underline{B}_i^O , \quad (3-65)$$

where

$$\underline{x}^O = [\bar{v} \quad \bar{\alpha}]^T = [v \quad \bar{\alpha}]^T$$

$$\underline{B}_i^O = \left[ \frac{S}{\rho} \quad g(1-\alpha) + f(\alpha) \right]^T \quad (3-66)$$

$$\underline{A}^O = \begin{bmatrix} 1-\alpha & -v \\ v & 0 \end{bmatrix}$$

$i$  = flow index.

By matrix inversion, Equation (3-65) is transformed to the form

$$\nabla_z \underline{x}^O = \underline{E}_i , \quad (3-67)$$

where

$$\underline{E}_i = (\underline{A}^O)^{-1} \underline{B}_i^O . \quad (3-68)$$

Equation (3-67) is now solved by dividing the channel into small segments such that  $\nabla v$  and  $\nabla \alpha$  vary rather slowly over these sections. Approximating the first derivatives by the

first central difference which is given by

$$\nabla_z \underline{x} = \frac{\underline{x}_{j+\frac{1}{2}} - \underline{x}_{j-\frac{1}{2}}}{\Delta z}, \quad (3-69)$$

where

$\Delta z$  = the axial interval width

$j$  = segment index.

Substituting Equation (3-69) into Equation (3-67) and rearranging yields for any segment  $j$

$$\underline{x}_{j+\frac{1}{2}}^o = (\underline{F}_j^i + \underline{x}_{j-\frac{1}{2}}^o) \Delta z, \quad (3-70)$$

where

$$\underline{F}_j^i = \frac{1}{2}(\underline{E}_{j+\frac{1}{2}}^i + \underline{E}_{j-\frac{1}{2}}^i) \quad (3-71)$$

for  $i = 1, 2$

$j = 1, 2, \dots, N$ .

The steady state solution at point  $j+\frac{1}{2}$  can be obtained from Equation (3-70) if its value at point  $j-\frac{1}{2}$  is known.

Therefore, starting the calculation at the bottom of the channel, the state vector  $\underline{x}^o$  can be calculated as a function of axial position. The steady state gradient  $\nabla_z \underline{x}^o$  can be directly calculated from Equation (3-67), which gives

$$\nabla_z \underline{x}_{j+\frac{1}{2}}^o = \frac{1}{2}(\underline{E}_{j+\frac{1}{2}}^i + \underline{E}_{j-\frac{1}{2}}^i) = \underline{F}_j^i \quad (3-72)$$

for  $j = 1, 2, \dots, N$

$i = 1, 2$ .

### 3. Solution of the stochastic two-phase flow

In the formulation presented in Section B.1 of this Chapter, the effects associated with bubbles coalescence and break up were introduced by allowing for random fluctuations in the velocity and void fraction of the bubbles. This led to Equation (3-60), which can now be solved numerically since all the coefficient matrices can be evaluated using the procedure described in the previous section.

To solve Equation (3-60) for the state vector  $\underline{x}$  as a function of space and frequency, the channel is again divided into  $N$  small segments. For any one segment  $j$ , the gradient is approximated by the first central difference, and subsequently Equation (3-60) can be approximated as

$$\underline{x}_{j+\frac{1}{2}}^i = (\underline{I} + \underline{D}_{j-\frac{1}{2}}^i)^{-1} (\underline{I} - \underline{D}_{j-\frac{1}{2}}^i) \underline{x}_{j-\frac{1}{2}}^i + (\underline{I} + \underline{D}_{j-\frac{1}{2}}^i) \underline{E}_{j-\frac{1}{2}}^i, \quad (3-73)$$

for  $i = 1, 2$

$j = 1, 2, \dots, N$

where

$$\begin{aligned} \underline{D}_j^i &= \frac{1}{2} \underline{A}_j^{-1} \underline{B}_j^i \Delta z \\ \underline{E}_j^i &= \underline{A}_j^{-1} \underline{S}_j \Delta z . \end{aligned} \quad (3-74)$$

Equation (3-73) can be put in the form

$$\underline{x}_{j+\frac{1}{2}}^i = \underline{R}_{j-\frac{1}{2}}^i \underline{x}_{j-\frac{1}{2}}^i + \underline{P}_{j-\frac{1}{2}}^i , \quad (3-75)$$

where

$$\underline{R}_j^i = (\underline{I} + \underline{D}_j^i)^{-1} (\underline{I} - \underline{D}_j^i)$$

$$\underline{P}_j^i = (\underline{I} + \underline{D}_j^i)^{-1} \underline{E}_j^i \quad (3-76)$$

For  $i = 1, 2$

$j = 1, 2, \dots, N.$

An examination of the coefficient matrices in Equation (3-75) reveals the following:

- a. The response matrix  $\underline{R}$  and the driving vector  $\underline{P}$  are dependent on a spatial index  $j$  and upon an index  $i$  that is associated with a given type of flow pattern.
- b. The elements of the driving vector,  $\underline{P}$  depend on the input noise source ( $\delta S$ ) which can be evaluated from the lumped parameter stochastic model developed in Section A.6 of this Chapter.
- c. All the elements of the response matrix  $\underline{R}$  are quantities that are related to the steady state solution which can be explicitly evaluated from the procedure of Section B.2 of this Chapter.

The solution of Equation (3-75) can be started by introducing the following boundary conditions (B.C.)

$$\underline{x}_2^i = \underline{0}, \quad (3-77)$$

for  $i = 1, 2$

where

$\underline{0}$  is the (2x1) null vector.

The use of this B.C. is, in effect, implying that at the entrance to the channel, no stochastic fluctuations exist.

4. Evaluation of the ASPD and the CPSD of the two-phase noise sources

As was previously pointed out, the purpose of this model is to develop expressions for the auto power spectral density (APSD) and the cross power spectral density (CPSD) of the void-age noise under various assumptions that pertain to the spatial correlation of the input noise sources. Clearly, Equation (3-75) which describes the dynamics of the noise vector,  $\underline{X}$  is not in the proper form. What must be done, in effect, is to cast this equation into a form where for any segment  $j$ , the contribution from the individual input noise vector  $\underline{P}$  are explicitly included from all the previous segments. A decoupling procedure, which was suggested by Singh and Stegemann [110] will be applied.

Starting with Equation (3-75), and setting  $j=1$  results in

$$\frac{\underline{x}_3^i}{2} = \frac{\underline{R}_1^i}{2} \frac{\underline{x}_1^i}{2} + \frac{\underline{P}_1^i}{2}. \quad (3-78)$$

Applying the B.C. of Equation (3-77) and dropping out the flow index  $i$ , yields

$$\frac{\underline{x}_3}{2} = \frac{\underline{P}_1}{2}. \quad (3-79)$$

Define

$$\underline{x}_{11} = \frac{\underline{P}_1}{2}. \quad (3-80)$$

Substituting back into Equation (3-79) gives

$$\frac{\underline{x}_3}{2} = \underline{x}_{11}. \quad (3-81)$$

Similarly, for  $j=2$  the result is

$$\frac{\underline{x}_5}{2} = \frac{R_3}{2} \frac{\underline{x}_3}{2} + \frac{P_3}{2} . \quad (3-82)$$

Substituting Equation (3-81) into the above equation, gives

$$\frac{\underline{x}_5}{2} = \underline{x}_{21} + \underline{x}_{22} = \sum_{k=1}^2 \underline{x}_{2k} , \quad (3-83)$$

where

$$\underline{x}_{21} = \frac{P_3}{2}$$

$$\underline{x}_{22} = \frac{R_3}{2} \underline{x}_{11} . \quad (3-84)$$

Proceeding in a similar manner, the  $j^{\text{th}}$  term is given by

$$\underline{x}_{j+\frac{1}{2}} = \sum_k \underline{x}_{jk} , \quad (3-85)$$

for  $k = 1, 2, \dots, j$

where

$$\underline{x}_{j1} = \underline{F}_{j-\frac{1}{2}}$$

$$\underline{x}_{jk} = \frac{R_{j-\frac{1}{2}}}{2} \underline{x}_{j-1,k-1} \quad (3-86)$$

for  $k = 2, 3, \dots, j$ .

By virtue of Equation (3-86), it can be shown, in general that

$$\underline{x}_{jk} = \frac{R_{j-\frac{1}{2}}}{2} \frac{R_{j-\frac{3}{2}}}{2} \cdots \frac{R_{N+\frac{1}{2}}}{2} \underline{x}_{N1} , \quad (3-87)$$

where

$$N = j-k+1 .$$

But according to Equation (3-86), the term  $\underline{x}_{N1}$  represents the input noise source at point  $N-\frac{1}{2}$ , it follows therefore that

$$\underline{x}_{jk} = \prod_{i=1}^{k-i} \underline{R}_{j-1+\frac{i}{2}} \underline{P}_{N-\frac{i}{2}} \quad (3-88)$$

In this form, the partial noise vector  $\underline{x}_{jk}$  contains explicitly the contribution from the input source at point  $j-k+\frac{1}{2}$ . Subsequently, Equation (3-85) is in the proper form for evaluating the APSD and the CPSD for input noise sources with different spatial correlation dependence. Since the main interest is to evaluate these quantities for the void fluctuations only, then in the foregoing treatment, only the second element of the fluctuation vector, namely  $\delta\alpha$  will be considered. Rewriting Equation (3-85) for this variable gives

$$\delta\alpha_{j+\frac{1}{2}} = \sum_k \delta\alpha_{jk}, \quad (3-89)$$

for  $k = 1, 2, \dots, j$ .

The spatial coherence of the noise sources can now be specified where the following three cases are considered:

- a. Noise sources are completely correlated in space. This arises in a situation where the interaction among the bubbles are nonexistent and thereby the channel acts as an ideal transmitter of any disturbance created in the channel, thus preserving "transit time" information of the bubbles. This situation is very unrealistic in an actual two-phase flow system, where bubble interactions are a common phenomenon.

The CPSD of the fluctuating voids is given by

$$\delta\alpha_{N+\frac{1}{2}, M+\frac{1}{2}}(\omega) = \sum_{jk} \delta^*\alpha_{Nj} \delta\alpha_{Mk}, \quad (3-90)$$

for  $j = 1, 2, \dots, N$

$k = 1, 2, \dots, M$ .

The L.H.S. of this equation is the CPSD between positions  $z_{N+\frac{1}{2}}$  and  $z_{M+\frac{1}{2}}$  at a given frequency  $\omega$ .

- b. Noise sources are completely uncorrelated in space. This arises in a situation where the interactions among the bubbles are so great as to render the noise sources to be completely independent of each other in the sense that their individual contribution to the noise field will not propagate upstream in the channel. Mathematically, this concept translates to the following expression

$$\delta \alpha_{N+\frac{1}{2}, M+\frac{1}{2}}(\omega) = \delta^* \alpha_{NN} \delta \alpha_{MM} . \quad (3-91)$$

- c. Noise sources are exponentially correlated in space. This implies that the contribution of the noise source at a given position is attenuated exponentially in the direction of flow. This loss of information is a direct consequence of the bubble interactions inside the channel. This assumption was shown to give the best fit to the experimental data obtained in a boiling water reactor coolant channel [110]. The expression for the CPSD in this case is given by

$$\delta \alpha_{N+\frac{1}{2}, M+\frac{1}{2}}(\omega) = \sum_{jk} \delta^* \alpha_{Nj} \delta \alpha_{Mk} e^{-(N+M-j-k)\mu\Delta Z} , \quad (3-92)$$

The evaluation of the APSD is accomplished by setting the indices M and N equal to each other in Equations (3-90) to (3-92). The corresponding results are

$$1. \quad P_{N+\frac{1}{2}}(\omega) = \sum_j |\delta \alpha_{Nj}|^2 , \quad (3-93)$$

for  $j = 1, 2, \dots, N$ .

$$2. \quad P_{N+\frac{1}{2}}(\omega) = |\delta \alpha_{NN}|^2 . \quad (3-94)$$

$$3. \quad P_{N+\frac{1}{2}}(\omega) = \sum_j |\delta \alpha_{Nj}|^2 e^{-(N-j)\mu\Delta Z} , \quad (3-95)$$

for  $j = 1, 2, \dots, N$ .

## 5. A simple model

The numerical procedures required to obtain the solutions to the various APSD's associated with bubble noise were outlined in the previous Section. In order to predict their

general frequency behavior expected in the test column, an analytical solution will be developed that is based on the following simplified assumptions

- a. The steady state variables  $\alpha$  and  $v$  are space independent along the channel.
- b. The stochastic variable,  $\delta v$  is assumed to be zero.

By virtue of the first assumption, the steady state gradient of both  $\alpha$  and  $v$  are zero and the slip ratio  $r$  is a constant. Introducing the above assumptions into Equation (3-54) yields

$$\frac{\partial}{\partial t}(\delta\alpha) + v\nabla(\delta\alpha) = - \frac{\delta s}{\rho} . \quad (3-96)$$

The R.H.S. of this equation represents the source term, and for the subsequent derivation, it is assumed to be a transit perturbation moving upstream with a speed  $v_o$ . Thus Equation (3-96) takes the form

$$\frac{\partial}{\partial t}(\delta\alpha) + v\nabla(\delta\alpha) = \delta(t - \frac{z}{v_o}) . \quad (3-97)$$

Taking the Laplace transform and simplifying gives

$$(\nabla + \frac{s}{v})\delta\alpha = \frac{e^{-sz/v_o}}{v} , \quad (3-98)$$

where  $s$  is the Laplace variable.

This equation is of a standard form and has the solution

$$\delta\alpha(z, s) = \frac{v_o}{s(v_o - v)} [e^{-sz/v_o} - e^{-sz/v}] . \quad (3-99)$$

The expression for the APSD is given by

$$P(z, \omega) = \frac{2v_o^2}{\omega^2(v_o - v)^2} [1 - \cos(\omega z \frac{v_o - v}{vv_o})] . \quad (3-100)$$

This expression has nulls at the following frequencies

$$f = \frac{\omega}{2n} = \frac{vv_o}{z(v_o - v)} \quad (i) \quad (3-101)$$

and the maxima at the following frequencies

$$f = \frac{v_o v}{2z(v_o - v)} (2i + 1) \quad (3-102)$$

for  $i = 0, 1, \dots$

The general shape of the APSD is depicted in Figure 3.2.

It exhibits sinks at frequencies given by Equation (101) and the peaks are enveloped by the curve  $1/\omega^2$ . If a bubble of slightly different speed is also present, it will contribute nulls and maxima to the APSD curve but at slightly different frequencies. The net effect will tend to smooth the total APSD curve. It follows that in the environment of an actual flow channel, where the speed of the bubbles is distributed around some mean value determined by the flow conditions, the shape of the APSD curve is expected to be much smoother than is shown in Figure 3.2.

Going back to Equation (3-102) and remembering that the slip ratio,  $r$  is constant, the position of the first maximum can be written as

$$f_{\max} = \frac{v_o}{2z(r-1)} \sim v_o . \quad (3-103)$$

This equation indicates that the position of the first maxima is shifted to a higher frequency as the bubble velocity is increased.

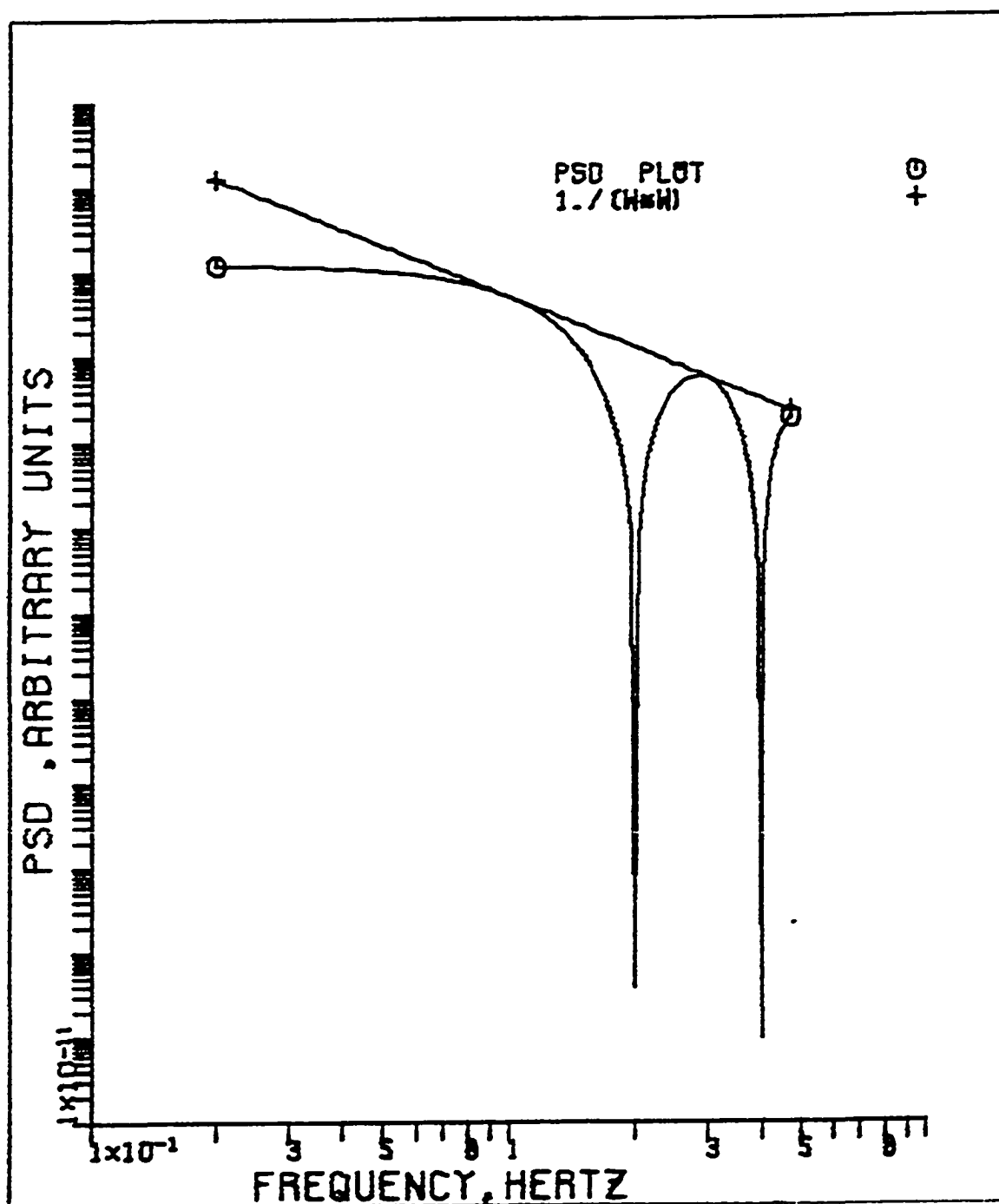


Figure 3.2. APSD, due to bubbles transport, as computed for a simple theoretical model

### C. Derivation of the Detector Response Model

Traditionally, the observed detector response to a disturbance introduced elsewhere in the system is obtained by what can be called a "two component response" method [4, 9, 27, 29, 60]. This technique involves the solution of the stochastic equations for the reactor in the adjoint space. The key feature is to cast the reactor equations in a two-group formulation. The resulting response is shown to be composed of two components with a long and a short relaxation length, respectively. The first component which is the global, reflects the coupled behavior of the neutron field caused by reactivity fluctuations in the immediate vicinity of the disturbance. Up to the present time, this technique is mostly applied to a simple one-dimensional homogeneous system. Analytical solutions were obtained for models using either the diffusion or the Fermi-age equation theory [4, 9].

The well-established methods for reactor transient calculations [31, 33, 34] may also be used to evaluate the detector response. Accordingly, the response in phase space may be modeled by nodal methods [48] in which the reactor is treated as a number of coupled regions, by modal methods [30] in which the response to a disturbance is analyzed in terms of flux eigenfunctions, and by series expansion of the Laplace transformed neutron balanced equations [113].

This section will describe a method first suggested by Cohn [23] to calculate the source transfer function in multi-groups, multi-dimensional approximations by using static techniques. Adapting this technique, the detector response is modeled through the adjoint space formalism to yield a system of equations that are Laplace transformed to a set of complex equations in phase space. Separating the equations into real and imaginary parts yields a system of coupled-inhomogeneous differential equations (two for each group). These can be solved by the well-established static techniques for the real and imaginary components of the complex amplitudes of the adjoint fluxes. The detector response can then be evaluated for a source having an arbitrary distribution. To check the validity of this concept, the one group diffusion model is first applied.

### 1. One-group diffusion model

The one group time dependent diffusion equations with six groups of delayed neutron are in the usual notations

$$\nabla \cdot D(\vec{r}, t) \nabla \phi(\vec{r}, t) - \sum_x (\vec{r}, t) \phi(\vec{r}, t) + (1-\beta) v \sum_f (\vec{r}, t) \phi(\vec{r}, t) + \sum_i \lambda_i C_i(\vec{r}, t) = v^{-1} \frac{\partial}{\partial t} \phi(\vec{r}, t) \quad (3-104a)$$

$$\beta_i v \sum_f (\vec{r}, t) \phi(\vec{r}, t) - \lambda_i C_i(\vec{r}, t) = \frac{\partial}{\partial t} C_i(\vec{r}, t) \quad (3-104b)$$

$i = 1, 2, \dots, 6.$

Random variation in reactor parameters will induce corresponding

fluctuations in the flux and precursor density. Accordingly, the time quantities in the above equations may now be resolved into a sum of a steady state part plus a fluctuating part

$$\begin{aligned}\phi(\vec{r}, t) &= \langle \phi(\vec{r}, t) \rangle + \delta\phi(\vec{r}, t) \\ C_i(\vec{r}, t) &= \langle C_i(\vec{r}, t) \rangle + \delta C_i(\vec{r}, t) \\ P(\vec{r}, t) &= \langle P(\vec{r}, t) \rangle + \delta P(\vec{r}, t),\end{aligned}\quad (3-105)$$

where the  $\langle \rangle$  stands for the expectation or the steady state value and  $P(\vec{r}, t)$  for the time dependent parameters ( $D$ ,  $\Sigma_r$ ,  $v\Sigma_f$ ).

It should be noted that the steady state components of Equation (3-105) satisfy Equation (3-104) with the time derivatives set to zero.

Substituting Equation (3-105) into Equation (3-104), subtracting the steady state parts and neglecting second order terms gives the linearized system of equations

$$\nabla \cdot \langle D \rangle \nabla \delta\phi - \langle \Sigma_r \rangle \delta\phi + (1-\beta) \langle v\Sigma_f \rangle \delta\phi + \sum_i \lambda_i \partial C_i = v^{-1} \frac{\partial}{\partial t} \delta\phi + S_0 \quad (3-106a)$$

$$\beta_i \langle v\Sigma_f \rangle \delta\phi - \lambda_i \partial C_i = \frac{\partial}{\partial t} \delta C_i + S_i \quad (3-106b)$$

where all the arguments are dropped for convenience, and

$$\begin{aligned}S_0 &= -\nabla \cdot \partial D(\vec{r}, t) \nabla \langle \phi \rangle + \partial \Sigma_r \langle \phi \rangle - (1-\beta) \langle \phi \rangle \partial (v\Sigma_f) \\ S_i &= -\beta_i \langle \phi \rangle \partial (v\Sigma_f).\end{aligned}\quad (3-106c)$$

Taking the Laplace transform of Equation (3-106b) and solving for  $\partial C_i$  gives

$$\partial C_i = [\beta_i \langle v \Sigma_f \rangle \partial \phi + \beta_i \partial (v \Sigma_r) \langle \phi \rangle] / (\lambda_i + j\omega) \quad (3-106d)$$

$i = 1, 2, \dots, 6.$

Taking the Laplace transform of Equations (3-106a) and (3-106b), substituting Equation (3-106d), and rearranging yields

$$[\nabla \cdot \langle D \rangle \nabla - (\langle \Sigma_r \rangle + \frac{j\omega}{v}) + \langle v \Sigma_f \rangle (1 - \beta + \sum_i \frac{\lambda_i \beta_i}{\lambda_i + j\omega})] \partial \phi = S, \quad (3-107a)$$

where

$$S = -\nabla \cdot \partial D(\vec{r}, \omega) \nabla \langle \phi \rangle + \partial \Sigma_r(\vec{r}, \omega) \langle \phi \rangle - v \partial \Sigma_f(\vec{r}, \omega) (1 - \beta + \sum_i \frac{\lambda_i \beta_i}{\lambda_i + j\omega}) \langle \phi \rangle, \quad (3-107b)$$

= noise source.

The noise source is attributed to the fluctuation of group constants in the system. Equation (3-107a) can be rewritten as

$$L \partial \phi(\vec{r}, \omega) = S \quad (3-108a)$$

where

$$L = \nabla \cdot \langle D \rangle \nabla - \langle \Sigma_r \rangle - j\omega v^{-1} + \langle v \Sigma_f \rangle (1 - \beta + \sum_i \frac{\lambda_i \beta_i}{\lambda_i + j\omega}). \quad (3-108b)$$

Using the definition of the adjoint operator [63] below

$$L^+ = L^{T*} \quad (3-108c)$$

the adjoint equation can be written immediately as

$$L^+ \psi(\vec{r}, \omega) + \Sigma_d(\vec{r}) = 0 \quad (3-109a)$$

where  $\Sigma_d(\vec{r})$  is the detector absorption cross section and plays the role of the adjoint source, and

$$L^+ = \nabla \cdot D \nabla - \langle \Sigma_r \rangle + j\omega v^{-1} + \langle v \Sigma_f \rangle (1 - \beta + \sum_i \frac{\lambda_i \beta_i}{\lambda_i - j\omega}), \quad (3-109b)$$

and where the group constants now refer to the steady state values.

Since the various quantities in Equations (3-109) are generally complex, while the usual procedures for solving such equations are designed for real quantities, the above formulation must be modified. The approach adopted here involves resolving the complex flux into the sum of a real plus imaginary parts, thus

$$\psi(\vec{r}, \omega) = \psi_1(\vec{r}, \omega) + j\psi_2(\vec{r}, \omega) , \quad (3-110)$$

where  $\psi_1$  and  $\psi_2$  are the in phase and quadrature components of the adjoint flux  $\psi$ . The substitution of Equation (3-110) into Equation (3-109) and equating the real and imaginary parts to zero, yields

$$D\nabla^2 \psi_1(\omega) - \Sigma_r^1(\omega) + \Sigma_{2-1}(\omega)\psi_2(\omega) + \Sigma_d = 0 , \quad (3-111a)$$

where for convenience, the argument  $r$  has been dropped and

$$\begin{aligned} \Sigma_r^1 &= \text{the modified removal cross section for the real group} \\ &= \Sigma_r - v \sum_f (1 - \beta + \sum_i \frac{\lambda_i^2 \beta_i}{\omega^2 + \lambda_i^2}) \end{aligned}$$

$\Sigma_{2-1}$  = the modified transfer cross section from the imaginary to the real group

$$= -\frac{\omega}{v} - v \sum_f \omega \sum_i \frac{\lambda_i \beta_i}{\omega^2 + \lambda_i^2}$$

$$D\nabla^2 \psi_2(\omega) - \Sigma_r^2(\omega)\psi_2(\omega) + \Sigma_{1-2}(\omega)\psi_1(\omega) = 0 , \quad (3-111b)$$

where

$$\Sigma_r^2(\omega) = \Sigma_r^1$$

$$\Sigma_{1-2}(\omega) = -\Sigma_{2-1}(\omega)$$

The coupled set of Equations (3-111) are inhomogeneous, due to the presence of the adjoint source  $\Sigma_d$ , and consequently can be treated by any static computer code that can handle up and down scattering and which has provision for an external source.

## 2. Two group model

The time dependent two-group telegrapher's equations, in the usual notations are

$$\begin{aligned} & \nabla \cdot D_1 \nabla \phi_1(\vec{r}, t) - \sum_{rl} \phi_1(\vec{r}, t) + (1-\beta) \sum_j v \Sigma_{fj} \phi_j(\vec{r}, t) + \sum_k \lambda_k C_k(\vec{r}, t) \\ & + S_1(\vec{r}, t) = (1+3D_1 \sum_{rl}) v_1^{-1} \frac{\partial}{\partial t} \phi_1(\vec{r}, t) + 3D_1 v_1^{-2} \frac{\partial^2}{\partial t^2} \phi_1(\vec{r}, t) \end{aligned} \quad (3-112a)$$

$$\begin{aligned} & \nabla \cdot D_2 \nabla \phi_2(\vec{r}, t) - \sum_{r2} \phi_2(\vec{r}, t) + \Sigma_{1-2} \phi_1(\vec{r}, t) + S_2(\vec{r}, t) \\ & = (1+3D_2 \sum_{r2}) v_2^{-1} \frac{\partial}{\partial t} \phi_2(\vec{r}, t) + 3D_2 v_2^{-2} \frac{\partial^2}{\partial t^2} \phi_2(\vec{r}, t) \end{aligned} \quad (3-112b)$$

$$\beta_k \sum_j v \Sigma_{fj} \phi_j(\vec{r}, t) - \lambda_k C_k(\vec{r}, t) = \frac{\partial}{\partial t} C_k(\vec{r}, t) \quad (3-113)$$

for  $j = 1, 2$

$k = 1, 2, \dots, 6$ .

In the above equations, all the group constants are assumed to be space and time dependent. Random fluctuations in the group constants induce random fluctuations in the state variables. The time dependent quantities can be written as

$$\begin{aligned}
 \phi_j(\vec{r}, t) &= \langle \phi_j(\vec{r}, t) \rangle + \delta\phi_j(\vec{r}, t) = \phi_j(\vec{r}) + \delta\phi_j(\vec{r}, t) \\
 C_k(\vec{r}, t) &= C_k(\vec{r}) + \delta C_k(\vec{r}, t) \\
 S_j(\vec{r}, t) &= S_j(\vec{r}) + \delta S_j(\vec{r}, t) \\
 D_j(\vec{r}, t) &= D_j(\vec{r}) + \delta D_j(\vec{r}, t) \\
 \Sigma_{xj}(\vec{r}, t) &= \Sigma_{xj}(\vec{r}) + \delta\Sigma_{xj}(\vec{r}, t) \\
 \Sigma_{fj}(\vec{r}, t) &= \Sigma_{fj}(\vec{r}) + \delta\Sigma_{fj}(\vec{r}, t) \\
 \Sigma_{1-2}(\vec{r}, t) &= \Sigma_{1-2}(\vec{r}) + \delta\Sigma_{1-2}(\vec{r}, t)
 \end{aligned} \tag{3-114}$$

for  $j = 1, 2$

$k = 1, 2, \dots, 6$ .

Substituting the above equations into Equations (3-112) and (3-113), subtracting the steady state and neglecting terms of second order, results in a linearized system of Equations that are identical to Equations (3-112) and (3-113) provided that the following interpretation is applied

- a. The state variables now represent the fluctuating parts only
- b. The source terms are now defined as

$$S_1(\vec{r}, t) = \nabla \cdot \delta D_1(\vec{r}, t) \nabla \phi_1(\vec{r}) - \delta \Sigma_{r1}(\vec{r}, t) \phi_1(\vec{r}) + \delta S_1(\vec{r}, t)$$

$$+ \sum_j v \delta \Sigma_{fj}(\vec{r}, t) (1-\beta) \phi_j(\vec{r})$$

= noise source for the fast group

$$S_2(\vec{r}, t) = \nabla \cdot \delta D_2(\vec{r}, t) \nabla \phi_2(\vec{r}) - \delta \Sigma_{r2}(\vec{r}, t) \phi_2(\vec{r})$$

$$+ \delta S_2(\vec{r}, t) + \delta \Sigma_{1-2}(\vec{r}, t) \phi_1(\vec{r})$$

= noise source for thermal group.

(3-115a)

Applying the Laplace transform of Equation (3-113) and solving for  $C_k$  yields

$$C_k(\vec{r}, \omega) = \sum_j v \delta \Sigma_{fj} \phi_j(\vec{r}, \omega) / (\lambda_k + i\omega) , \quad (3-115b)$$

where  $i = \sqrt{-1}$ .

Applying the Laplace transform to Equation (3-112) gives

$$(\nabla \cdot D_1 \nabla - \Sigma_{r1}) \phi_1 + (1-\beta) \sum_j v \delta \Sigma_{fj} \phi_j + \sum_k \lambda_k C_k + S_1$$

$$= [i\omega(1+3D_1\Sigma_{r1})/v_1 - 3D_1\omega^2/v_1^2] \phi_1 \quad (3-115c)$$

$$(\nabla \cdot D_2 \nabla - \Sigma_{r2}) \phi_2 + \sum_k \lambda_k C_k + S_2 = [i\omega(1+3D_2\Sigma_{r2})/v_2 - 3D_2\omega^2/v_2^2] \phi_2$$

(3-115d)

where the arguments  $\vec{r}$  and  $\omega$  are dropped out for convenience, and

$$S_1 = (\nabla \cdot \delta D_1 \nabla - \delta \Sigma_{r1}) \phi_1 + \sum_j v \delta \Sigma_{fj} \left( \frac{\lambda_k \beta_k}{\lambda_k + i\omega} \right) \phi_j$$

$$S_2 = (\nabla \cdot \delta D_2 \nabla - \delta \Sigma_{r2}) \phi_2 + \delta \Sigma_{1-2} \phi_1 . \quad (3-115e)$$

Eliminating  $C_k$  from Equation (3-115c) and rearranging yields

$$\begin{aligned} & [\nabla \cdot D_1 \nabla - \Sigma_{rl} + v \Sigma_{f1} (1 - \beta + \sum_k \frac{\lambda_k \beta_k}{\lambda_k + i\omega}) - i\omega (1 + 3D_1 \Sigma_{rl}) v_1^{-1} + 3D_1 \omega^2 v_1^{-2}] \phi_1 \\ & + v \Sigma_{f2} (1 - \beta + \sum_k \frac{\lambda_k \beta_k}{\lambda_k + i\omega}) \phi_2 + S_1 = 0 . \end{aligned} \quad (3-116a)$$

Rearranging Equation (3-115d) gives

$$[\nabla \cdot D_2 \nabla - \Sigma_{r2} - i\omega (1 + 3D_2 \Sigma_{r2}) v_2^{-1} + 3D_2 \omega^2 v_2^{-2}] \phi_2 + \Sigma_{l-2} \phi_1 + S_2 = 0 \quad (3-116b)$$

Rewriting Equation (3-116) in matrix form

$$\underline{L} \underline{\phi} + \underline{S} = \underline{0} , \quad (3-117a)$$

where

$$\underline{\phi} = [\phi_1(\vec{r}, \omega) \quad \phi_2(\vec{r}, \omega)]^T$$

$$\underline{S} = [S_1(\vec{r}, \omega) \quad S_2(\vec{r}, \omega)]^T$$

$$L_{11} = D_1 \nabla^2 - \Sigma_{rl} + v \Sigma_{f1} (1 - i\omega \sum_k \frac{\beta_k}{\lambda_k + i\omega}) - \frac{i\omega (1 + 3D_1 \Sigma_{rl})}{v_1} + \frac{3D_1 \omega^2}{v_1^2}$$

$$L_{12} = v \Sigma_{f2} (1 - i\omega \sum_k \frac{\beta_k}{\lambda_k + i\omega})$$

$$L_{21} = \Sigma_{l-2}$$

$$L_{22} = D_2 \nabla^2 - \Sigma_{r2} - \frac{(1 + 3D_2 \Sigma_{r2}) i\omega}{v_2} + \frac{3D_2 \omega^2}{v_2^2}$$

$$\underline{L} = \begin{bmatrix} L_{11} & L_{12} \\ L_{21} & L_{22} \end{bmatrix} . \quad (3-117b)$$

Transforming to adjoint space, the corresponding equation is

$$\underline{L}^+ \underline{\Psi} + \underline{\Sigma}_d = 0 , \quad (3-118a)$$

where

$$\underline{\Psi} = \text{adjoint flux vector} = [\Psi_1(\vec{r}, \omega) \quad \Psi_2(\vec{r}, \omega)]^T$$

$$\underline{\Sigma}_d = \text{adjoint source} [\Sigma_{d1}(\vec{r}) \quad \Sigma_{d2}(\vec{r})]^T . \quad (3-118b)$$

The adjoint operator is by definition

$$\underline{L}^+ = \underline{L}^{T*} . \quad (3-119)$$

Then applying the above definition to Equation (3-117) gives

$$\underline{L}^+ = \begin{bmatrix} L_{11}^* & L_{21}^* \\ L_{12}^* & L_{22}^* \end{bmatrix} \quad (3-120a)$$

where

$$L_{11}^* = D_1 v^2 - \Sigma_{r1} + v \Sigma_{f1} (1 + i\omega \sum_k \frac{\beta_k}{\lambda_k - i\omega}) + \frac{i\omega (1 + 3D_1 \Sigma_{r1})}{v_1} + 3D_1 \omega^2 v_1^{-2}$$

$$L_{21}^* = \Sigma_{1-2}$$

$$L_{12}^* = v \Sigma_{f2} (1 + i\omega \sum_k \frac{\beta_k}{\lambda_k + i\omega})$$

$$L_{22}^* = D_2 v^2 - \Sigma_{r2} + \frac{i\omega (1 + 3D_2 \Sigma_{r2})}{v_2} + \frac{3D_2 \omega^2}{v_2^2} . \quad (3-120b)$$

The complex quantities in Equation (3-118) can now be resolved as the sum of a real part plus an imaginary part to give

$$\underline{L}^+ = \underline{L}_R^+ + i \underline{L}_I^+ , \quad (3-121a)$$

where

$$\underline{\underline{L}}_R^+ = \begin{bmatrix} D_1 v^2 - \Sigma_{x1} + 3\omega^2 D_1 v_1^{-2} & \Sigma_{1-2} \\ + v \Sigma_{f1} (1 - \omega^2 \sum_k \frac{\beta_k}{\omega^2 + \lambda_k^2}) & \\ v \Sigma_{f2} (1 - \omega^2 \sum_k \frac{\beta_k}{\omega^2 + \lambda_k^2}) & D_2 v^2 - \Sigma_{x2} + 3D_2 \omega^2 v_2^{-2} \end{bmatrix}$$

$$\underline{\underline{L}}_I^* = \begin{bmatrix} \omega (v \Sigma_{f1} \sum_k \frac{\beta_k \lambda_k}{\omega^2 + \lambda_k^2} + (1 + 3D_1 \Sigma_{x1}) v_1^{-1}) & 0 \\ v \Sigma_{f2} \omega \sum_k \frac{\beta_k \lambda_k}{\omega^2 + \lambda_k^2} & \omega (1 + 3D_2 \Sigma_{x2}) v_2^{-1} \end{bmatrix}$$

and

$$\underline{\Psi} = \underline{\Psi}_R + i \underline{\Psi}_I ,$$

where

$$\underline{\Psi}_R = [\Psi_{x1} \quad \Psi_{x2}]^T$$

$$\underline{\Psi}_I = [\Psi_{I1} \quad \Psi_{I2}]^T . \quad (3-121b)$$

Substituting Equation (3-121) into Equation (3-118) and equating the real and imaginary parts to zero yields

$$\underline{\underline{L}}_R \underline{\Psi}_R - \underline{\underline{L}}_I \underline{\Psi}_I + \underline{\Sigma}_d = 0 \quad (3-122a)$$

$$\underline{\underline{L}}_R \underline{\Psi}_I + \underline{\underline{L}}_I \underline{\Psi}_R = 0 . \quad (3-122b)$$

Expanding Equation (3-122) and rearranging gives for real fast

$$A \Psi_{R1} + B \Psi_{I1} + \sum_{l=2} \Psi_{R2} = \Sigma_{d1} \quad (3-123a)$$

for imaginary fast

$$A \Psi_{I1} - B \Psi_{R1} + \sum_{l=2} \Psi_{I2} = 0 \quad (3-123b)$$

for real thermal

$$C \Psi_{R2} + F \Psi_{I2} + G \Psi_{R1} + H \Psi_{I1} = \Sigma_{d2} \quad (3-123c)$$

for imaginary thermal

$$C \Psi_{I2} - F \Psi_{R2} + G \Psi_{I1} - H \Psi_{R1} = 0 , \quad (3-123d)$$

where

$$\begin{aligned} A &= D_1 V^2 - \sum_{r1} + v \sum_{f1} (1 - \omega^2 \sum_k \frac{\beta_k}{\omega^2 + \lambda_k^2}) + \frac{3D_1 \omega^2}{v_1^2} \\ B &= -\omega (v \sum_{f1} \sum_k \frac{\lambda_k \beta_k}{\omega^2 + \lambda_k^2} + \frac{(1+3D_1 \sum_{r1})}{v_1}) \\ C &= D_2 V^2 - \sum_{r2} + \frac{3D_2 \omega^2}{v_2^2} \quad (3-123e) \\ F &= - \frac{(1+3D_2 \sum_{r2}) \omega}{v_2} \\ G &= v \sum_{f2} (1 - \omega^2 \sum_k \frac{\beta_k}{\omega^2 + \lambda_k^2}) \\ H &= \omega v \sum_{f2} \sum_k \frac{\lambda_k \beta_k}{\omega^2 + \lambda_k^2} . \end{aligned}$$

As will be shown later, it is more convenient to redefine the adjoint fluxes in the following manner, let

$$\psi_2 = \psi_{R1}$$

$$\psi_3 = \psi_{I1}$$

$$\psi_4 = \psi_{R2}$$

$$\psi_5 = \psi_{I2}$$

(3-124)

Equation (3-123) can be cast into the more familiar multi-group diffusion representation by defining the subsequent modified cross sections

$$\Sigma_2^r = \text{removal cross section} = \Sigma_{rl} - 3\omega^2 D_1 / v_1^2$$

$$\Sigma_{32} = -\frac{\omega}{v_1}(1+3D_1\Sigma_{rl}) - v\Sigma_{fl}\omega \sum_k \frac{\lambda_k \beta_k}{\omega^2 + \lambda_k^2}$$

$$\Sigma_{42} = \Sigma_{1-2}$$

$$\Sigma_{22} = v\Sigma_{fl}(1-\omega^2 \sum_k \frac{\beta_k}{\omega^2 + \lambda_k^2}) \quad (3-125)$$

$$v\Sigma_2^f = v\Sigma_{f2}(1-\omega^2 \sum_k \frac{\beta_k}{\omega^2 + \lambda_k^2})$$

$$D^2 = D_1$$

$$\Sigma_{52} = \chi_2 = 0 .$$

Equation (3-123a) can now be written in the more compact form as

$$D^2 \nabla^2 \psi_2 - \Sigma_2^r \psi_2 + \sum_{i=2}^5 (\Sigma_{i2} + \chi_2 v \Sigma_i^f) \psi_i = \Sigma_{dl} , \quad (3-126a)$$

Similarly, let

$$\begin{aligned}
 \Sigma_3^r &= \Sigma_{r1} - 3D_1\omega^2/v_1^2 \\
 \Sigma_{23} &= -\Sigma_{32} \\
 \Sigma_{33} &= \Sigma_{22} \\
 \Sigma_{53} &= \Sigma_{42} \\
 D^3 &= D_1 \\
 \Sigma_{43}^f &= v\Sigma_3^f = x_3 = 0 .
 \end{aligned} \tag{3-127}$$

Then, substituting Equation (3-127) into Equation (3-123b) and rearranging gives

$$D^3 v^2 \Sigma_3^r - \Sigma_3^r \Sigma_3^f + \sum_{i=2}^5 (\Sigma_{i3} + x_3 v \Sigma_i^f) \Sigma_i^r = 0 . \tag{3-126b}$$

For Equation (3-123c), let

$$\begin{aligned}
 \Sigma_4^r &= \Sigma_{r2} - 3D_2\omega^2/v_2^2 \\
 \Sigma_{34} &= -\omega v \Sigma_{f2} \sum_k \frac{\lambda_k \beta_k}{\omega^2 + \lambda_k^2} \\
 \Sigma_{54} &= -\omega(1+3D_2\Sigma_{r2})/v_2 \\
 D^4 &= D_2 \\
 x_4 &= 1 \\
 \Sigma_{24}^4 &= \Sigma_{44}^4 = v \Sigma_4^4 = 0 .
 \end{aligned} \tag{3-128}$$

Then substituting and rearranging, Equation (3-123c) is reduced to

$$D^4 \nabla^2 \Psi_4 - \Sigma_4^r \Psi_4 + \sum_{i=2}^5 (\Sigma_{i4} + \chi_4 v \Sigma_i^f) \Psi_i = \Sigma_{d2} . \quad (3-126c)$$

Finally, defining

$$\begin{aligned} \Sigma_5^r &= \Sigma_4^r \\ \Sigma_{25} &= -\Sigma_{34} \\ \Sigma_{35} &= v \Sigma_2^f \\ \Sigma_{45} &= -\Sigma_{54} \\ D^5 &= D_2 \\ \Sigma_{55} &= v \Sigma_5^f = \chi_5 = 0 . \end{aligned} \quad (3-129)$$

Using the above definitions, reduces Equation (3-123d) to the form

$$D^5 \nabla^2 \Psi_5 - \Sigma_5^r \Psi_5 + \sum_{i=2}^5 (\Sigma_{i5} + \chi_5 v \Sigma_i^f) \Psi_i = 0 . \quad (3-126d)$$

The set of Equations (3-126) represents four coupled inhomogeneous differential equations that can be solved by a multi-group, multi-dimensional static code that has provisions for

1. Up and down scattering from any group to all other groups.
2. External arbitrary source distributions.

The requirement for handling an external source can be obviated by introducing a dummy group. This trick is used in many diffusion codes [35, 47]. It has the advantage of a much faster convergence rate than for the original source problem.

For convenience, the first group is selected to be the dummy. Since the source terms appear in the second and fourth groups (refer to Equation (3-126)), these sources can be introduced by assigning an appropriate transfer cross section from the dummy group to the respective groups.

Normally the cross sections for the dummy group are chosen in such a way as to give a flat spatial flux distribution. In this situation, the source in a given group,  $j$  can be expressed by

$$s^j(\vec{r}) = \psi_1 \Sigma_{1j}(\vec{r}) = (\text{const.}) \Sigma_{1j}(\vec{r}) . \quad (3-130)$$

The above equation implies that the transfer cross section takes the same spatial form as the source distribution.

Introducing the above concepts, one can write, immediately for the dummy group

$$-\Sigma_1^r \psi_1 + \Sigma_{11} \psi_1 = 0 , \quad (3-131)$$

where the rest of this group parameters are set to zero. Note that in order for the above equation to have a solution,  $\Sigma_{11}$  must be set equal to  $\Sigma_1^r$ . Substituting Equation (3-131) and the definition (3-130) into Equation (3-126) yields

$$D_i \nabla^2 \psi_i - \Sigma_i^r \psi_i + \sum_j (\Sigma_{ji} + \chi_i v \Sigma_j^f) \psi_j = 0$$

for  $j = 1, 2, \dots, 5$

$$i = 1, 2, \dots, 5 . \quad (3-132)$$

The above equation is now in the standard form of the multi-group diffusion approximation. Many standard codes are available for its solution [35, 47]. It should be remembered that in this notation, the adjoint flux vector as a function of space and frequency is given by

$$\underline{\psi} = [\psi_2(\vec{r}, \omega) + j\psi_3(\vec{r}, \omega) \quad \psi_4(\vec{r}, \omega) + j\psi_5(\vec{r}, \omega)]. \quad (3-133)$$

#### D. Evaluation of the ASPD and CPSD of the detector response function

In the multi-group time dependent formalism, the operator  $\underline{L}$  is related to its adjoint operator  $\underline{L}^+$  through the following general relationship

$$\langle \underline{\psi}, \underline{L}\phi \rangle = \langle \underline{\phi}, \underline{L}^+ \underline{\psi} \rangle, \quad (3-134)$$

where the symbol  $\langle , \rangle$  stands for the inner product between two vectors and is defined as [63]:

$$\langle \underline{x}, \underline{y} \rangle = \int_{\vec{r}} \underline{x}^T \underline{y} d\vec{r}. \quad (3-135)$$

Substituting Equations (3-117) and (3-118) reduces Equation (3-134) to the form

$$\langle \underline{\psi}, \underline{S} \rangle = \langle \underline{\phi}, \underline{\Sigma}_d \rangle. \quad (3-136)$$

The R.H.S. of this equation is nothing more than the total reaction rate inside the detector, and consequently represents the detector response. In view of this fact and in order to make any sense of the L.H.S., one has to interpret the adjoint flux as representing the probability that a source, at a given

position, may contribute in terms of reaction rate to a detector placed elsewhere.

Apparently, the detector response can be evaluated with equal ease using either of the above operations. This conclusion, however, is not true in general, since in dealing with a given problem, it is usually more convenient to use one over the other. To elucidate this point, consider the following two problems

1. Evaluating the response of a fixed detector to an arbitrary source distribution
2. Evaluating the response of two or more detectors to a fixed source distribution.

Clearly, in the first case, it is easier to adopt the adjoint space approach, since the adjoint function needs to be evaluated only once. The detector response to any source can be evaluated from a simple integration over space. On the other hand, it's far more convenient for the second case to apply the regular flux space since the flux need be evaluated, for the given source, only once. The detector response at any position can be evaluated from a simple integration step.

In the treatment that follows, the objective is to determine the detector response in phase space subject to an arbitrary source distribution. It follows, that the more efficient approach is to use the adjoint space, namely

$$R(\vec{r}_d, \omega) = \langle \Psi(\vec{r}, \vec{r}_d, \omega), S(\vec{r}, \omega) \rangle . \quad (3-137)$$

where

$\underline{R}(\vec{r}_d, \omega)$  = Fourier transform of the detector response  
 $\vec{r}_d$  = position of the detector.

According to noise theory [25, 26, 116, 122] the CSPD between two detectors is given by

$$\begin{aligned}\underline{C}(\vec{r}_1, \vec{r}_2, \omega) &= \underline{R}^*(\vec{r}_1, \omega) \underline{R}(\vec{r}_2, \omega) \\ &= \langle \underline{\psi}(\vec{r}, \vec{r}_1, \omega), \underline{S}(\vec{r}, \omega) \rangle^* \langle \underline{\psi}(\vec{r}, \vec{r}_2, \omega), \underline{S}(\vec{r}, \omega) \rangle, \quad (3-138)\end{aligned}$$

where  $\underline{C}$  is a (2x1) vector, and the subscripts 1 and 2 refer to the first and second detector, respectively. Performing the complex conjugation reduces the above equation to

$$\underline{C}(\vec{r}_1, \vec{r}_2, \omega) = \langle \underline{S}(\vec{r}, \omega), \underline{\psi}(\vec{r}, \vec{r}_1, \omega) \rangle \langle \underline{\psi}(\vec{r}, \vec{r}_2, \omega), \underline{S}(\vec{r}, \omega) \rangle. \quad (3-139)$$

The APSD can be evaluated by setting  $r_1$  equal to  $r_2$  in Equation (3-139), the result is

$$\underline{P}(\vec{r}_1, \omega) = |\langle \underline{\psi}_1(\vec{r}, \vec{r}_1, \omega), \underline{S}(\vec{r}, \omega) \rangle|^2, \quad (3-140)$$

where

$\underline{P}$  is a (2x1) APSD vector.

So far nothing has been said about the source  $\underline{S}$  except that it arises from random fluctuations in the group constants and that its components are given by Equation (3-115e). This equation is simplified by noting that the experimental set-up is carried out in the vertical central stringer (VCS) of the reactor where the gradient terms are essentially zero.

Accordingly Equation (3-115e) reduces to

$$S_1(\vec{r}, \omega) = -\delta\Sigma_{r1}(\vec{r}, \omega)\phi_1(\vec{r}) \quad (3-141a)$$

and

$$S_2(\vec{r}, \omega) = -\delta\Sigma_{r2}(\vec{r}, \omega)\phi_2(\vec{r}) + \delta\Sigma_{12}(\vec{r}, \omega)\phi_1(\vec{r}). \quad (3-141b)$$

Let  $\Sigma_0$  stand for the value of any type of cross section when the void fraction is zero, then clearly for a void fraction  $\alpha$  the following holds

$$\Sigma = (1-\alpha)\Sigma_0 \quad (3-142)$$

and

$$\delta\Sigma = -\Sigma_0\delta\alpha. \quad (3-143)$$

Applying Equation (3-143) to Equation (3-141) gives

$$\underline{S} = [-\Sigma_{r1}\phi_1\delta\alpha(\vec{r}, \omega) \quad (-\Sigma_{r2}\phi_2 + \Sigma_{12}\phi_1)\delta\alpha(\vec{r}, \omega)]^T. \quad (3-144)$$

It should be remembered that the term  $\delta\alpha(\vec{r}, \omega)$ , which represents the noise source due to void fluctuations, has already been evaluated in Section B of this Chapter and is given by Equation (3-89).

It is interesting to note the sign difference in the thermal component of the source. On physical grounds, this could be explained by the fact that the presence of a void will reduce the density of the medium which in turn will induce a reduction in the cross sections  $\Sigma_{12}$  and  $\Sigma_{r2}$ . A reduction in  $\Sigma_{r2}$  allows more neutrons to reach the detector, while a

similar effect in the moderator cross section,  $\Sigma_{l2}$  causes fewer number of neutrons to be thermalized and, consequently, detected.

#### IV. EXPERIMENTAL SET-UP

As was previously pointed out, the purpose of the experimental investigation was to explore the possibility of identifying a two-phase flow regime, in a reactor channel, through some unique structure in the noise spectra. To this end a recirculating two-phase flow loop, containing water and nitrogen gas bubbles, was operated in the UTR-10 reactor. The neutron noise generated by the flowing bubbles was observed with two  $\text{BF}_3$  detectors.

##### A. The UTR-10 Reactor

The UTR-10 reactor is water and graphite moderated and water cooled. The basic element of the reactor is a 112 x 142 x 112 cm parallelepiped constructed of reactor grade graphite. The fuel is imbedded in two rectangular boxes separated by 45.7 cm of graphite. The test apparatus was located in the central vertical stringer (CVS). The reactor cooling system flows through the fuel elements and is totally independent of the experimental flow arrangements. A longitudinal section view of this reactor is shown in Figure 4.1.

##### B. Experimental Loop

The detailed design of this loop, along with the safety analysis is contained in the experiment's design and safety report [96]. A schematic diagram of the loop is shown in Figure 4.2 and the following is a general description of its

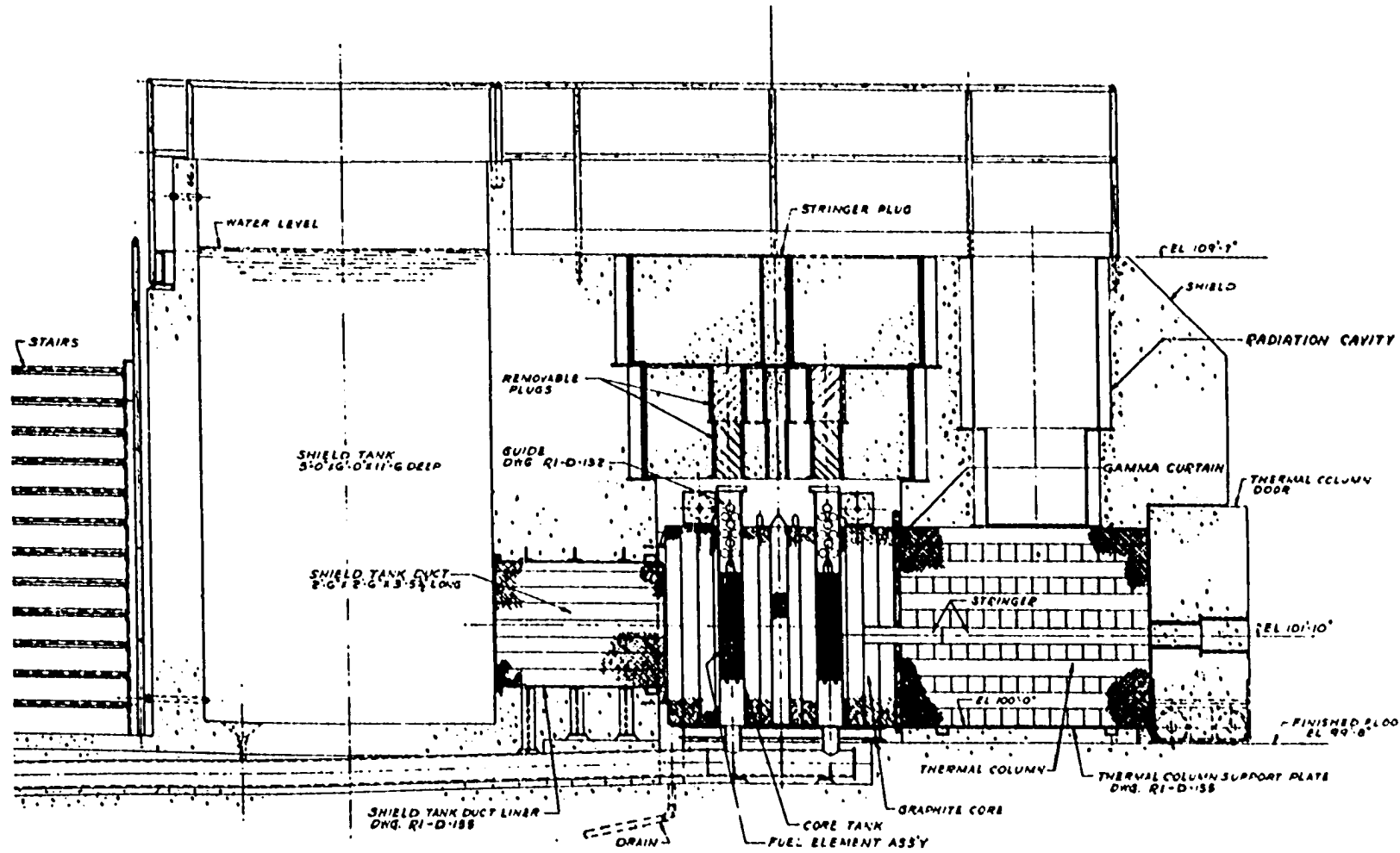


Figure 4.1. The longitudinal cross-sectional view of the UTR-10 reactor [96]

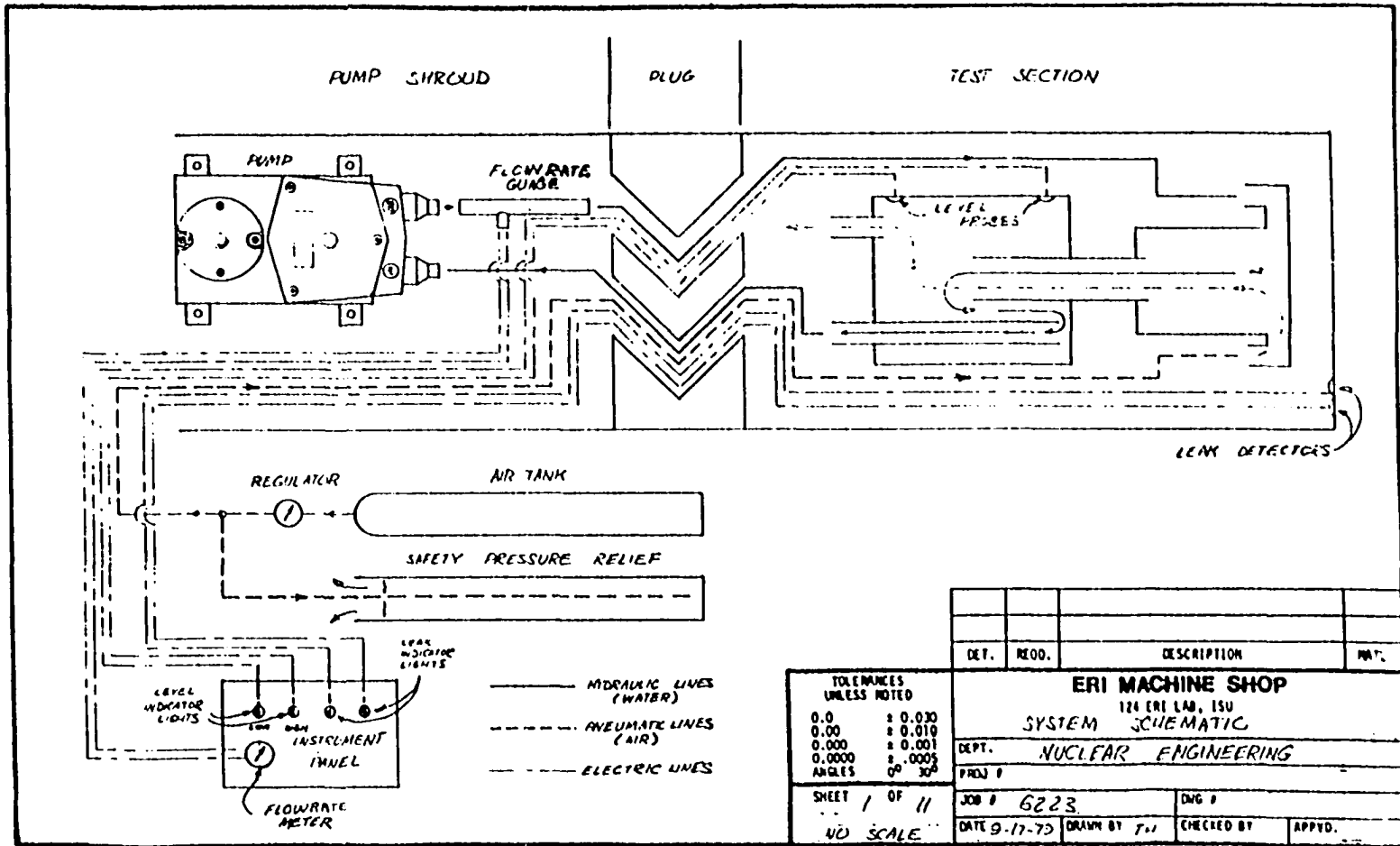


Figure 4.2. A schematic diagram of the experimental loop [96]

main components:

- a. The test section consists of two annular plexiglass tubes 30 cm long that are placed end to end. The lower section is 3.75 cm in diameter and the upper section is 1.85 cm. This change in cross section is intended to simulate a partially blocked coolant channel where two-phase flow is taking place.
- b. The water reservoir provides a continuous supply of water throughout the loop and also acts as a surge tank. By virtue of its special design, which can be examined in Figure 4.3, it acts as a separator that strips the gas from the two phase mixture.
- c. The air bubbler introduces purified nitrogen gas through a 0.1 cm diameter orifice (#54 drill) placed at the base of the test section. Nitrogen gas was chosen because of its low neutron activation cross section.
- d. The self-priming pump draws water from the reservoir and circulates it through the test section. The pump is of the U-shaped molded elastomer type (Model 760, Tat Engineering, Inc.) which is driven by a variable speed D.C. motor. Control of the water flow is accomplished through maintaining a constant driving D.C. voltage on the electric motor. Under this condition, the discharge pressure and flow rate are kept constant. The water flow rates are continuously monitored by a

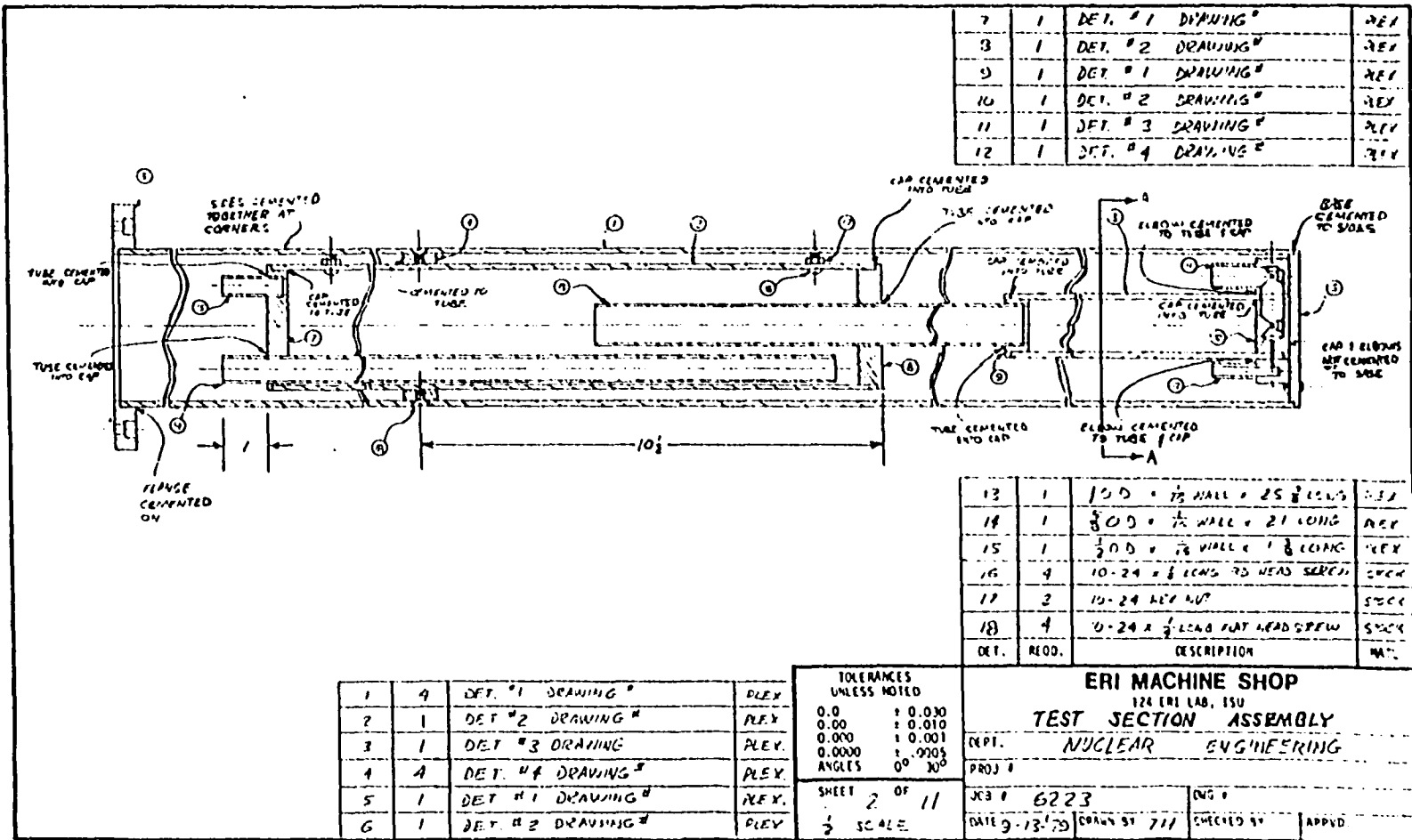


Figure 4.3. The detailed design of the test section assembly [96]

paddle-wheel type sensor (Model MK-315, Cole Parmer, Co.).

- e. Two water level sensors are placed inside the water reservoir to insure constant experimental conditions.
- f. A leak detector that is placed at the base of the loop is incorporated to activate the pump trip circuit in the event of a leak detection.
- g. Two  $\text{BF}_3$  neutron detectors (Type G-5-1, N. Wood Counters Lab., Inc.) are placed along the test section at a distance of 15 and 45 cm respectively from the bottom of the test channel. These minature detectors (2.5 cm long x 1.75 cm, dia.) are operated in the current mode as ion chambers. This is accomplished through maintaining the outer wall of the chamber (the cathode) at a -90 volts with respect to ground, while the central electrode (the anode) is left neutral as shown schematically in Figure 4.6.

Before the loop was installed, the regular 122 cm long graphite vertical central stringer (VCS) was removed and replaced with a 61 cm long stringer. The loop was then placed on top of the short stringer so that its lower end rested on a plane midway through the core. The materials of the loop which are inside the (VCS) region are made exclusively of plexiglass to minimize neutron activation. Other materials in the loop include water, nitrogen gas bubbles, neoprene, tygon tubing and co-axial signal cables. The loop is capped with a

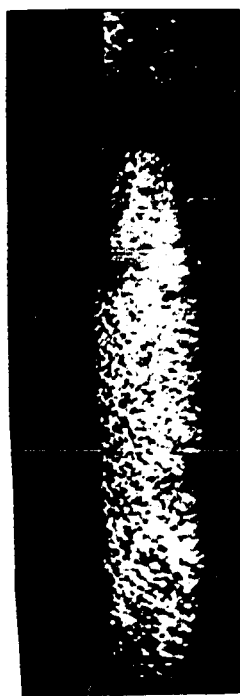
shielding plug, that is provided with two slanted conduits for cables and tubes. The exhaust nitrogen gas was collected at the top of the reservoir by a tygon tube and led through the shielding plug to an air monitor (Model AMS-2, Eberline Inst. Corp.).

An exact replica of the loop was also constructed for an out-of-core measurement. Basically, these measurements allow the flow conditions that exist in the reactor to be studied and photographed to provide identification of the flow regime associated with a particular neutron spectrum. 35 mm pictures were made for the flow conditions to be studied and representative samples are shown in Figure 4.4. The actual experimental loop is shown in Figure 4.5.

### C. The Signal Processing System

The signal processing system is shown schematically in Figure 4.6. Basically, the current from the detector is preamplified through a locally constructed FET input amplifier having a gain of  $10^6$ - $10^8$ , D.C. bias compensated, amplified and recorded on an FM tape recorder (PI-6200, Precision Inst., Inc.). The recorded signals were played back from the FM recorder for Fourier analysis. The signals were high-pass filtered to remove the drift, low-pass filtered to eliminate aliasing, which will be discussed in the next chapter, and amplified to  $\pm 5$  volts to provide optimum usage of the range of the analog-to-digital converter (ADC).

**Figure 4.4.** Examples of two-phase flow regimes created in the test section: (a) bubbly flow; (b) bubbly (lower section) and slug flow (upper section); (c) bubbly (lower) and slug and churn (upper); (d) churn (below) and slug and churn flow (upper)



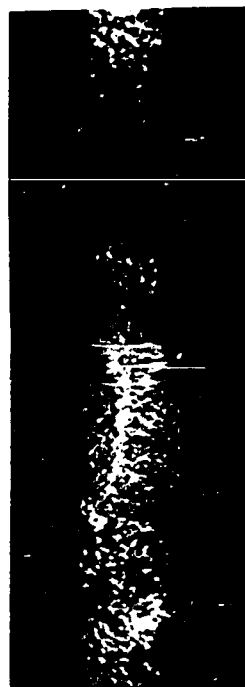
(a)



(b)



(c)



(d)

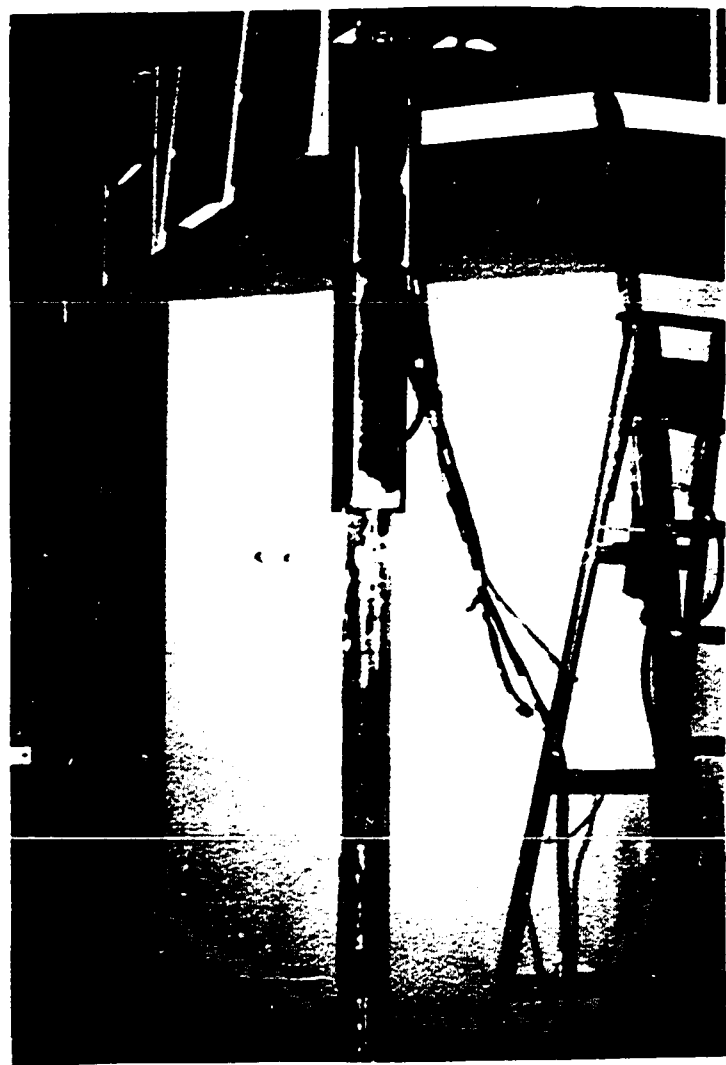


Figure 4.5. The experimental two-phase flow loop

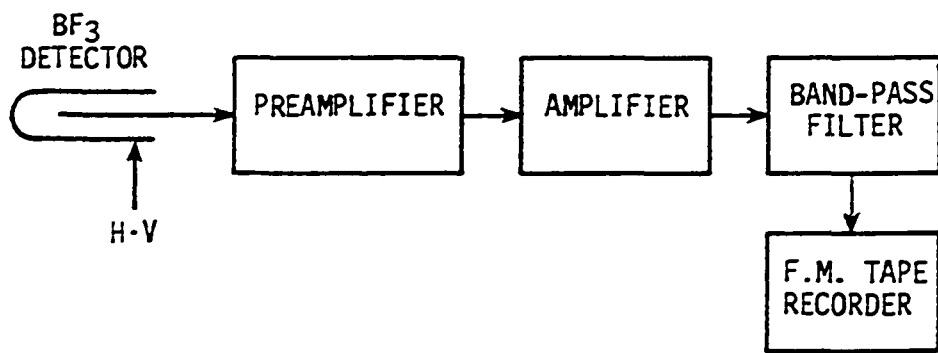


Figure 4.6. Block diagram of the reactor noise detection system

The digital data acquisition system is based around a 32K MSI-6800 micro-computer. The peripherals include a floppy disk drive and controller (FD-8, Midwest Scientific Inst., Co.), a hard copy terminal (Model 33, Teletype Corp.), a CRT control terminal (Model ADM, Information Display) and an interfaced ADC board (locally constructed) with up to 16 input channels. The ADC board is based on a Burr Brown MP-21 micro-chip. Its design permits the sampling rate to be controlled through software programming. The digitized data from the two detectors are transferred to the micro-computer and are stored in blocks of 512 words. These points are then Fourier transformed by a fast Fourier transform (FFT) algorithm that was specifically written for this system in Basic language. This program is capable of producing, simultaneously, the two auto spectra, the cross power spectral density and the coherence of the input signals. A flow chart of this program is shown in Figure 4.7. (More details and a complete listing of this program are presented in Appendix A). The actual data acquisition and analysis system is shown in Figure 4.8, while the block diagram is shown in Figure 4.9.

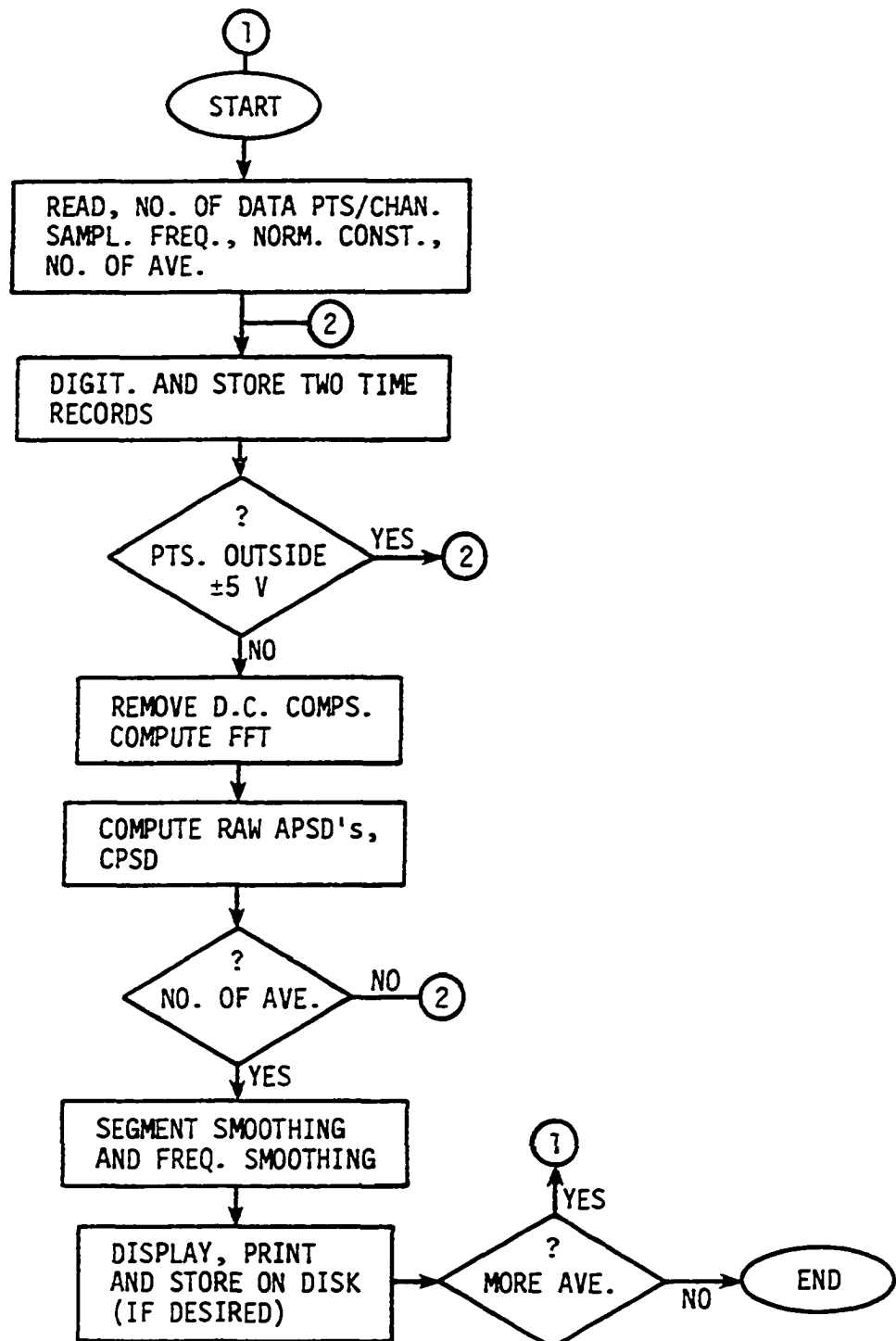


Figure 4.7. Flow diagram of the FFT program

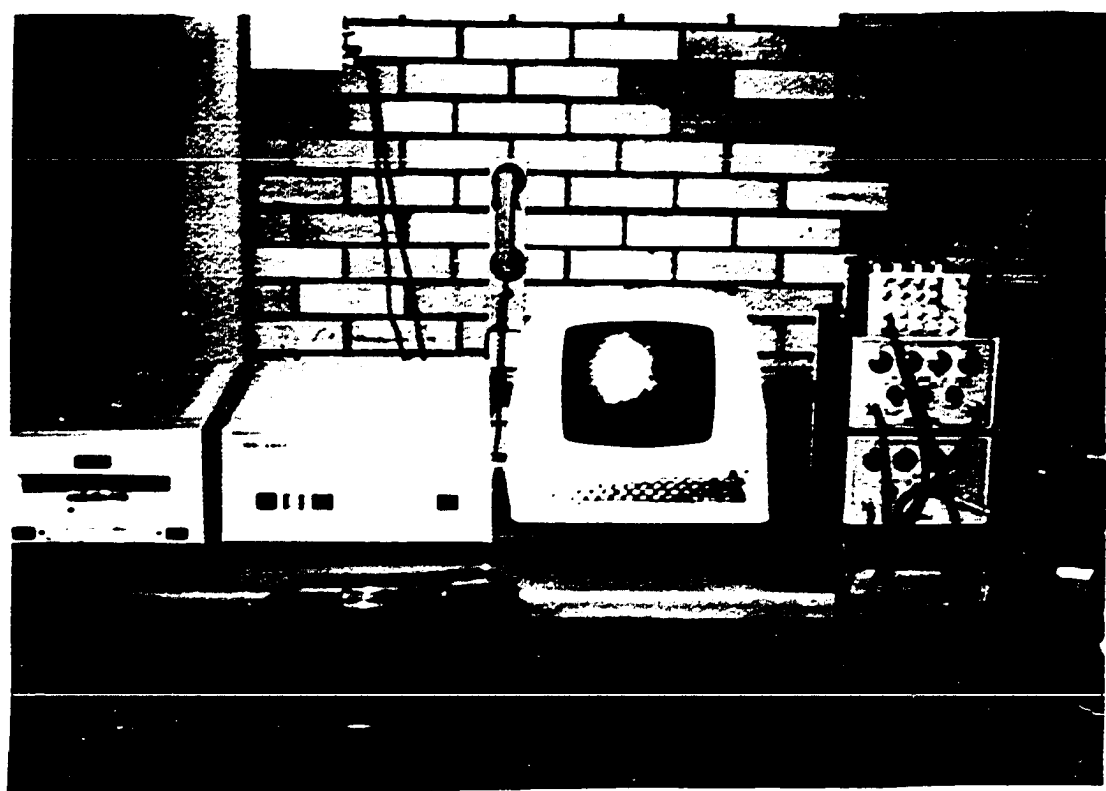


Figure 4.8. The data acquisition system

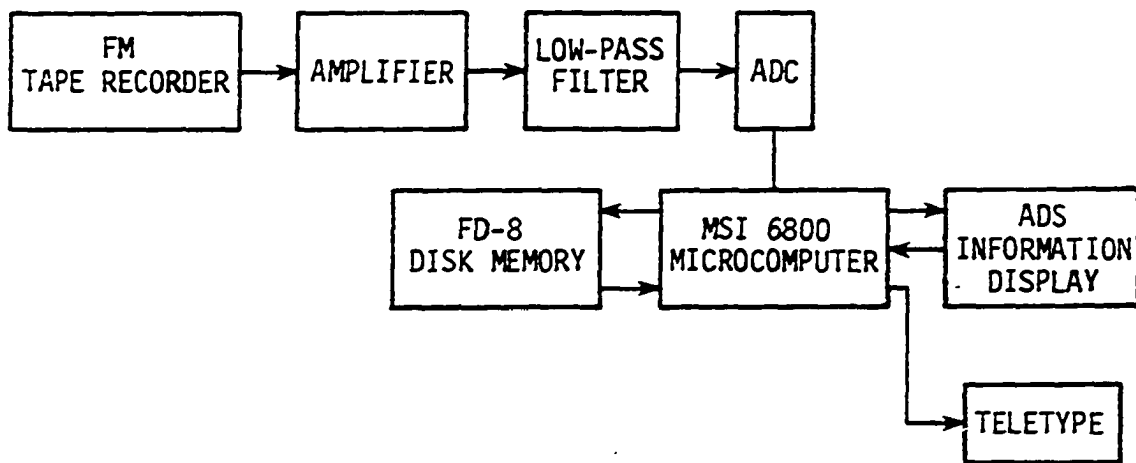


Figure 4.9. Block diagram of the data acquisition system

## V. EXPERIMENTAL PROCEDURES

Subsequent to the assembly and initial checkout for this system, a series of measurements was performed to determine the static reactivity worth of this loop and the dynamic reactivity with bubbling taking place. The total reactivity of the loop was obtained by noting the change in control rod position for criticality, with and without the loop. Its reactivity worth is approximately  $-26 \times 10^{-4} \Delta k/k$  and the corresponding worth for the voids is  $1.2 \times 10^{-5} \Delta k/k$  for a one-percent increase in the void fraction [96].

In order to determine the optimum power level for this experiment, a series of runs was performed. At each power level, two runs were conducted, one with bubbling, the other with no bubbling and the signal to noise ratio, defined as follows, was noted

$$\frac{S}{N} = \frac{\text{r.m.s. of the noise signal with bubbling}}{\text{r.m.s. of the noise signal with no bubbling}} \quad (5-1)$$

At a power level of 500 watts, this ratio was about five, and accordingly it was decided that at these conditions, the APSD of the detection noise is almost negligible (only about 4%) as compared to the total APSD of the noise with bubbling. Figure 5.1 shows the results for a typical run at 500 watts.

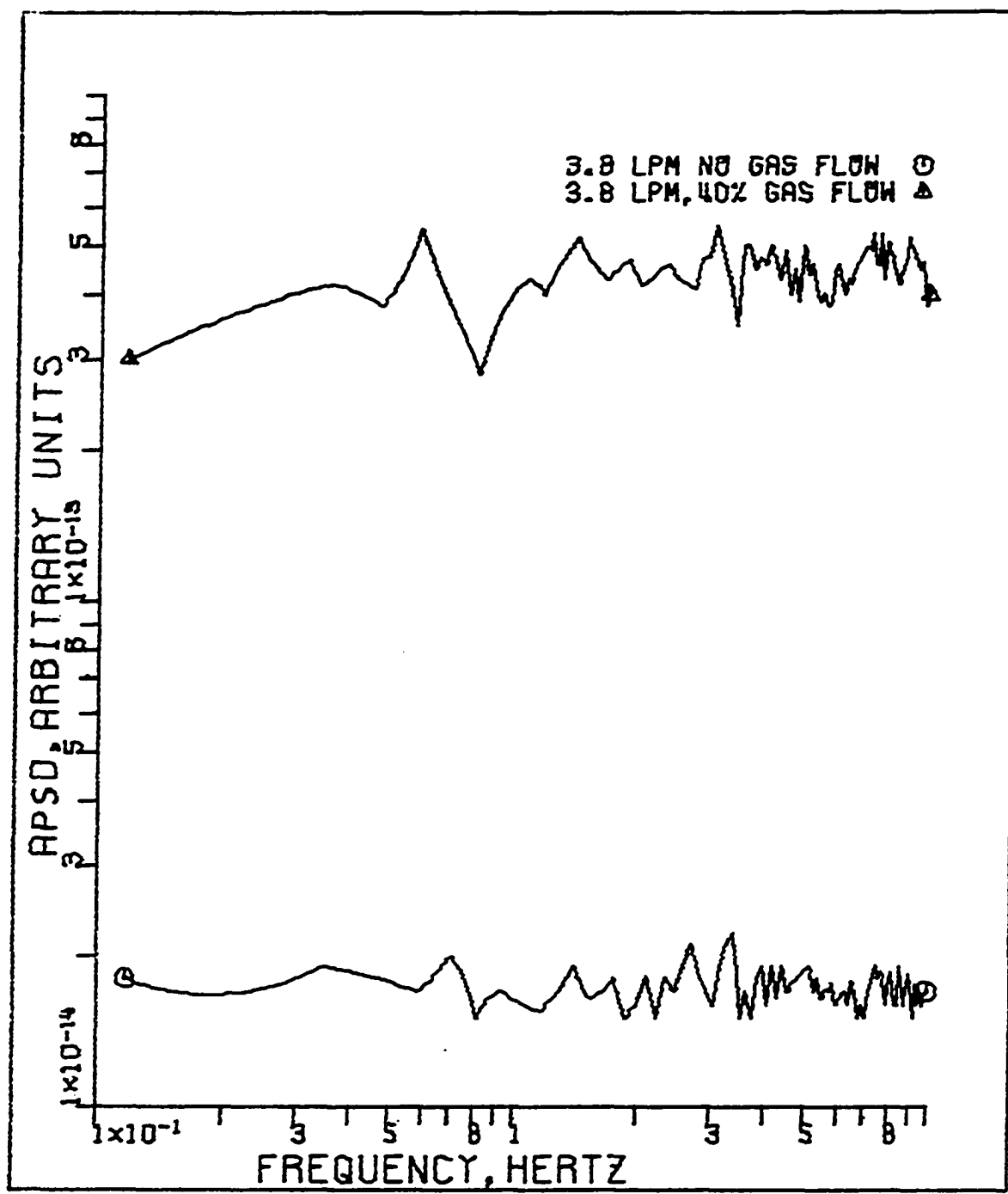


Figure 5.1. APSD at 500 W, observed at detector A, for the case of bubbly two-phase flow and liquid flow only

### A. Anti-aliasing Procedures

In sampling theory, the Nyquist frequency is defined as [12, 25, 56]

$$f_N = \frac{1}{2} f_s , \quad (5-2)$$

where  $f_s$  is the sampling rate of the ADC.

If the Nyquist frequency,  $f_N$ , is lower than the maximum frequency component in the signal, then the frequency components higher than  $f_N$  will fold back and contaminate the frequency spectrum below  $f_N$ . This phenomenon is called aliasing. According to Bendat and Piersol [12], the sampling frequency,  $f_s$  has to be at least twice the maximum frequency component present in the signal, in order to avoid aliasing. For good accuracy, however, it is suggested to use a sampling rate that is 2 - 2.5 times higher than  $f_{max}$ . Preliminary analysis indicated that the anticipated noise structure, due to bubbling is in the range of 1 - 10 Hertz. Accordingly, the low pass filter cutoff was set at 12.5 Hertz and the sampling rate at 30 per second.

### B. Electronics and Software Systems Checks

The data acquisition system was checked by a calibrated sine-wave generator (Model III, Wavetek, Inc.) to verify the accuracy of the sampling rate mechanism which, as mentioned earlier, is software controlled. All the expected lines in the spectra were seen to fill at the expected frequencies. Another check was performed, this time to verify the performance of the data analysis system. The system of Figure 5.2 was used to

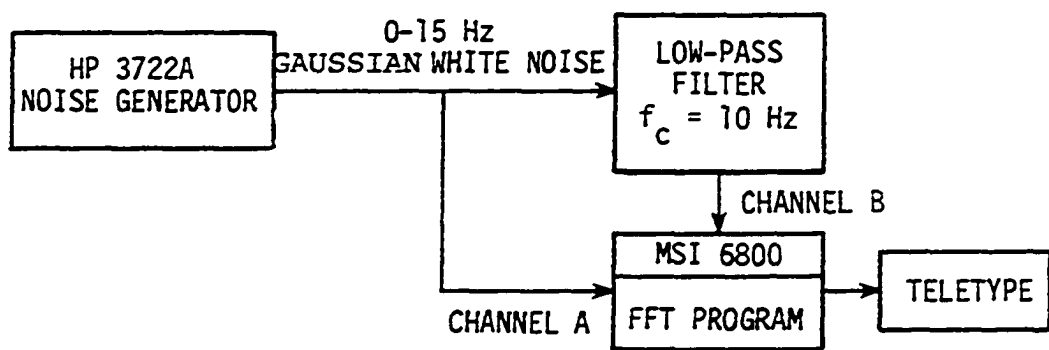


Figure 5.2. Block diagram of the system for evaluating the transfer function of a filter

evaluate the transfer function characteristics of a low pass filter. A white noise generator (Model 3722A, Hewlett Packard) was used in the experiment and the results compared well with the published data [81]. The results are shown in Figures 5.3 and 5.4. From these measurements it was concluded that the system was operating correctly.

The detection-analysis chain was verified by operating the reactor at low power (one watt) where the dominant noise source is the detection noise, which is a white spectrum [22]. The measured APSD is displayed in Figure 5.5 and clearly represents a white noise spectrum.

### C. Two-phase Flow Characteristics

A total of twenty-six experimental runs were performed with various air and water flow conditions present in the loop. Two parameters specify the flow conditions for each run. These are the water flow rate and the air flow rate. Due to the type of pump used, its operation introduced a repetitive component in the detector signal that corresponds to the harmonics of the basic RPM of the pump. These components will appear as a multi-peak structure in the APSD spectra corresponding to the first and higher harmonics of the pump. Obviously, these extra features have to be removed in order to avoid obscuring the noise structure due to two-phase flow characteristics. One way of doing this is to perform two runs for a given water flow condition, one with no voids being generated and the other with

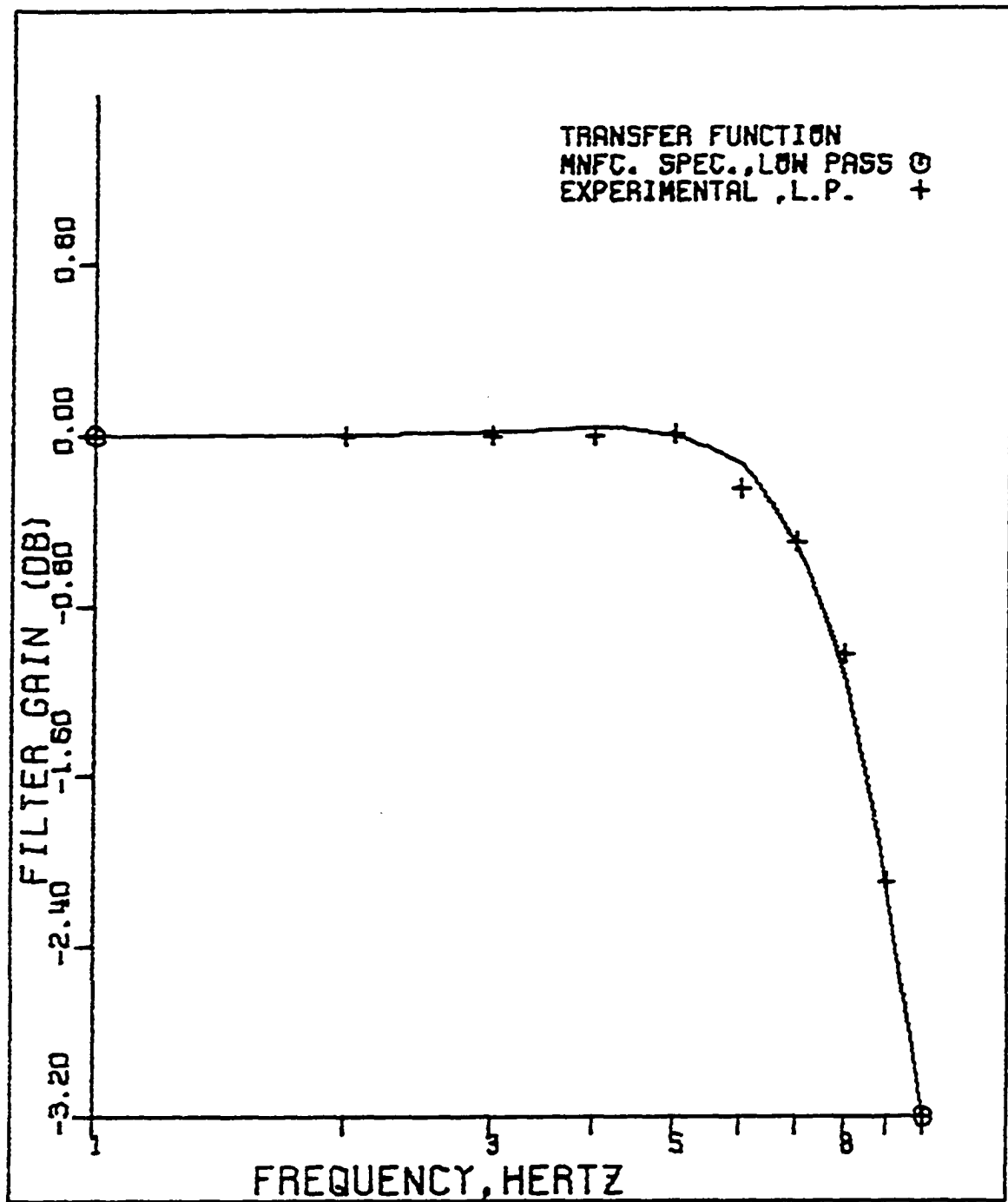


Figure 5.3. The magnitude of the transfer function of the anti-aliasing filter with cutoff frequency set at 10 Hz

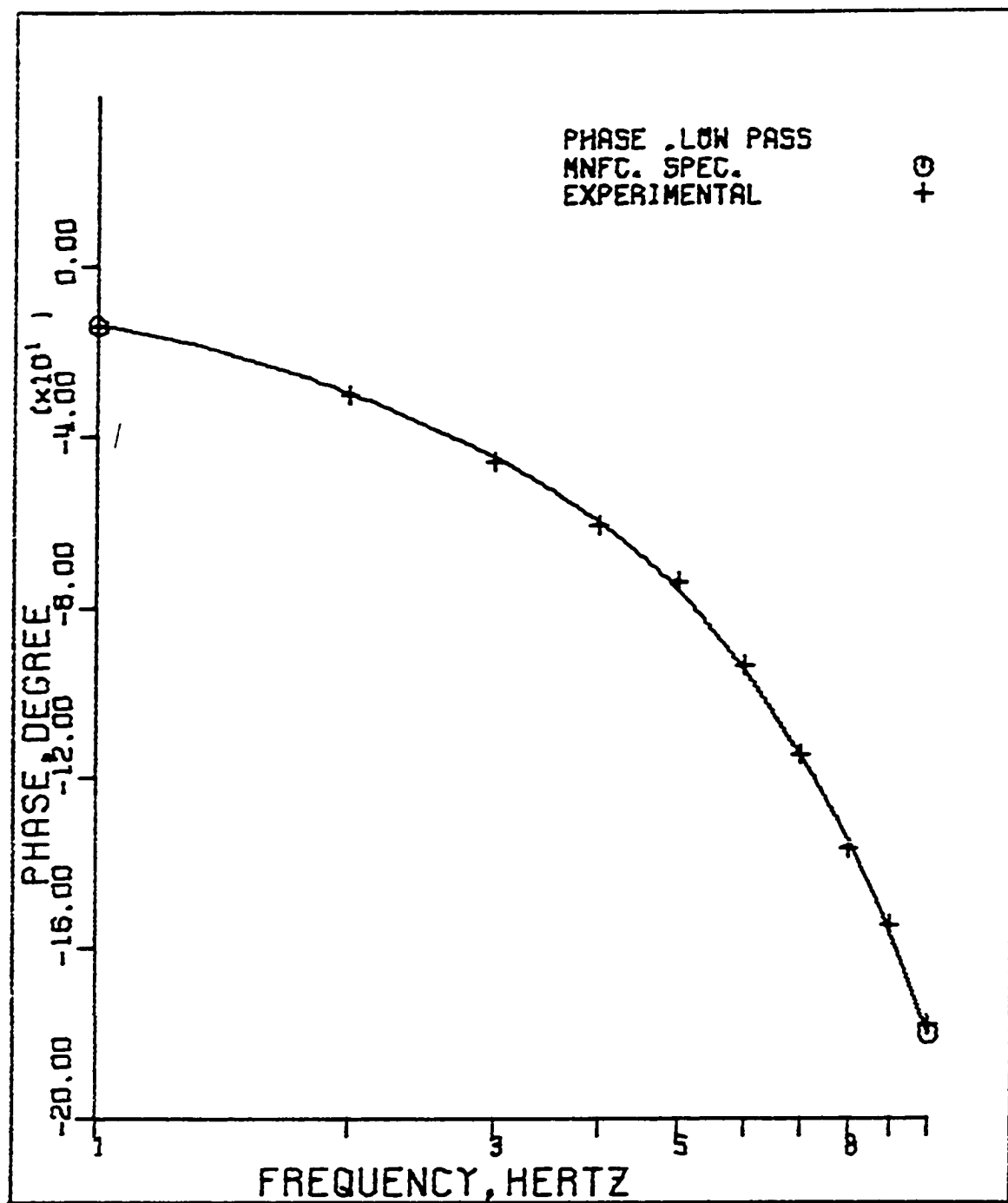


Figure 5.4. The phase characteristics of the anti-aliasing filter

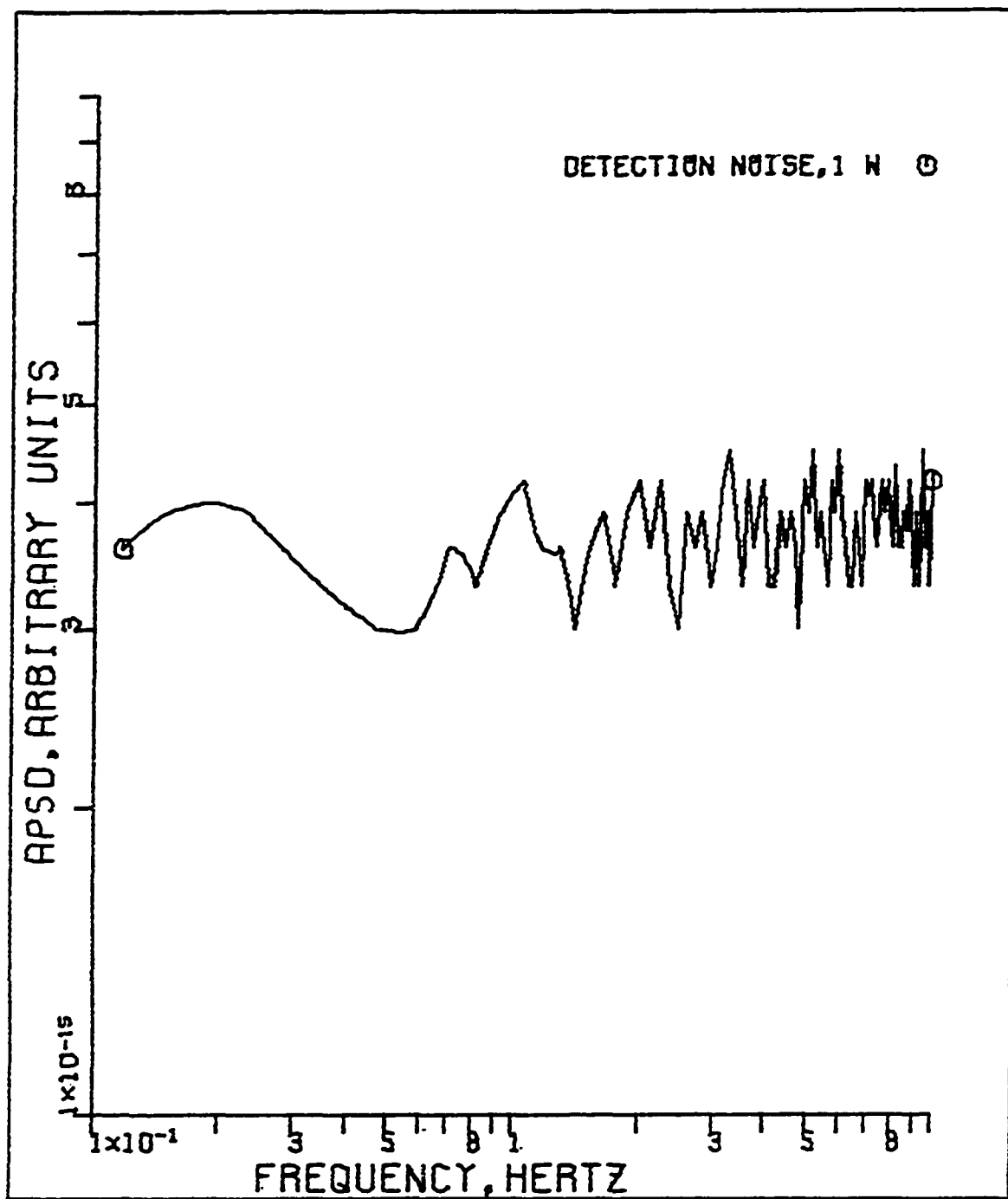


Figure 5.5. APSD of the reactor at one watt, observed at detector A

voids being generated. The first measurement will give the harmonics of the pump only and the other will give, in addition, the two-phase flow pattern structure. However, as it turned out that these harmonics appeared as very sharp peaks in the noise spectrum. It was found to be more practical to remove each peak by simply passing a straight line through its base and subtracting the peak. Figure 5.6 shows the APSD for a typical run. The sharp peaks correspond to the first and higher harmonics of the pump. The same curve is reproduced in Figure 5.7 after the peak removal procedures were applied.

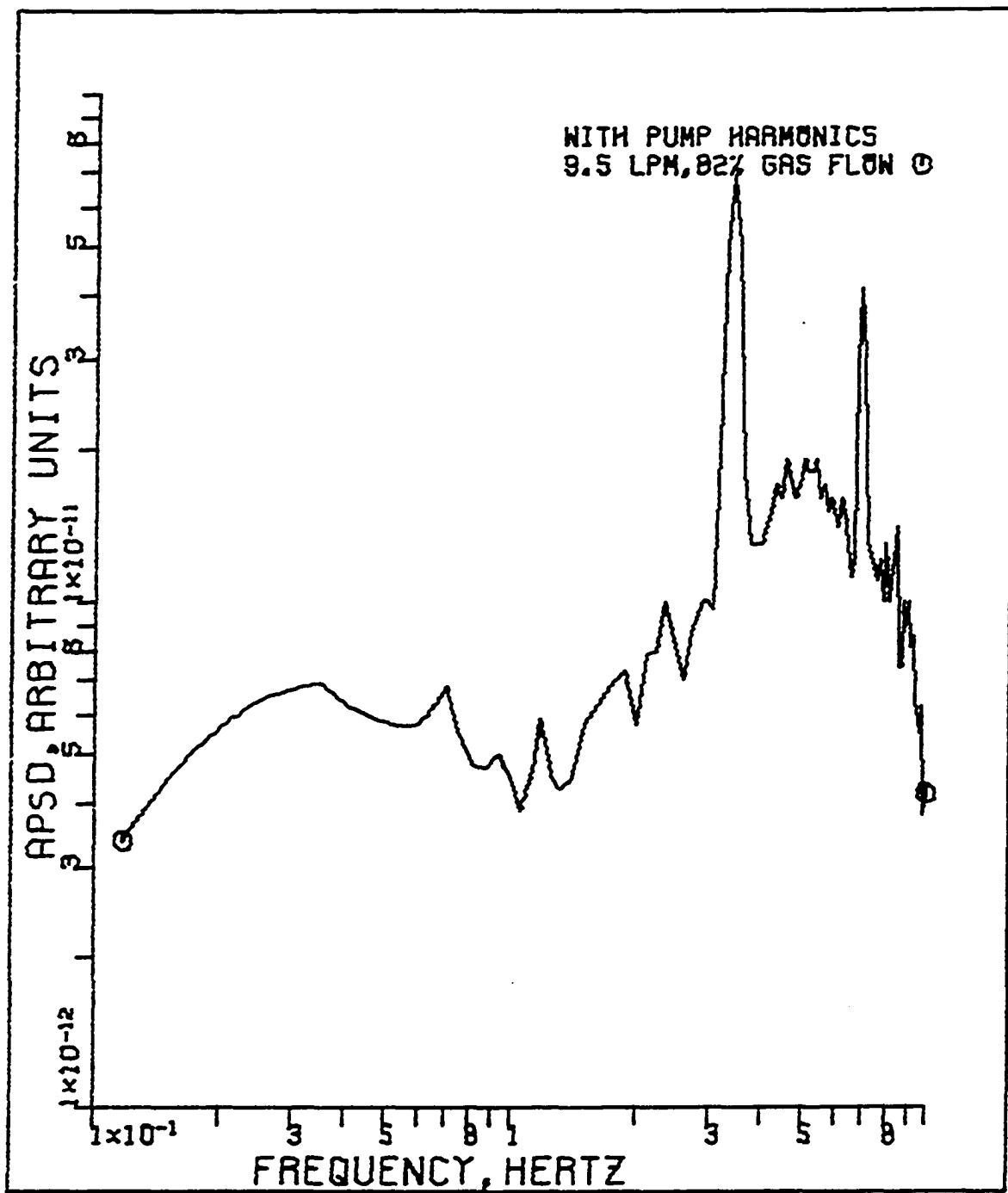


Figure 5.6. APSD for run 1-4-33 before the pump's harmonics were removed

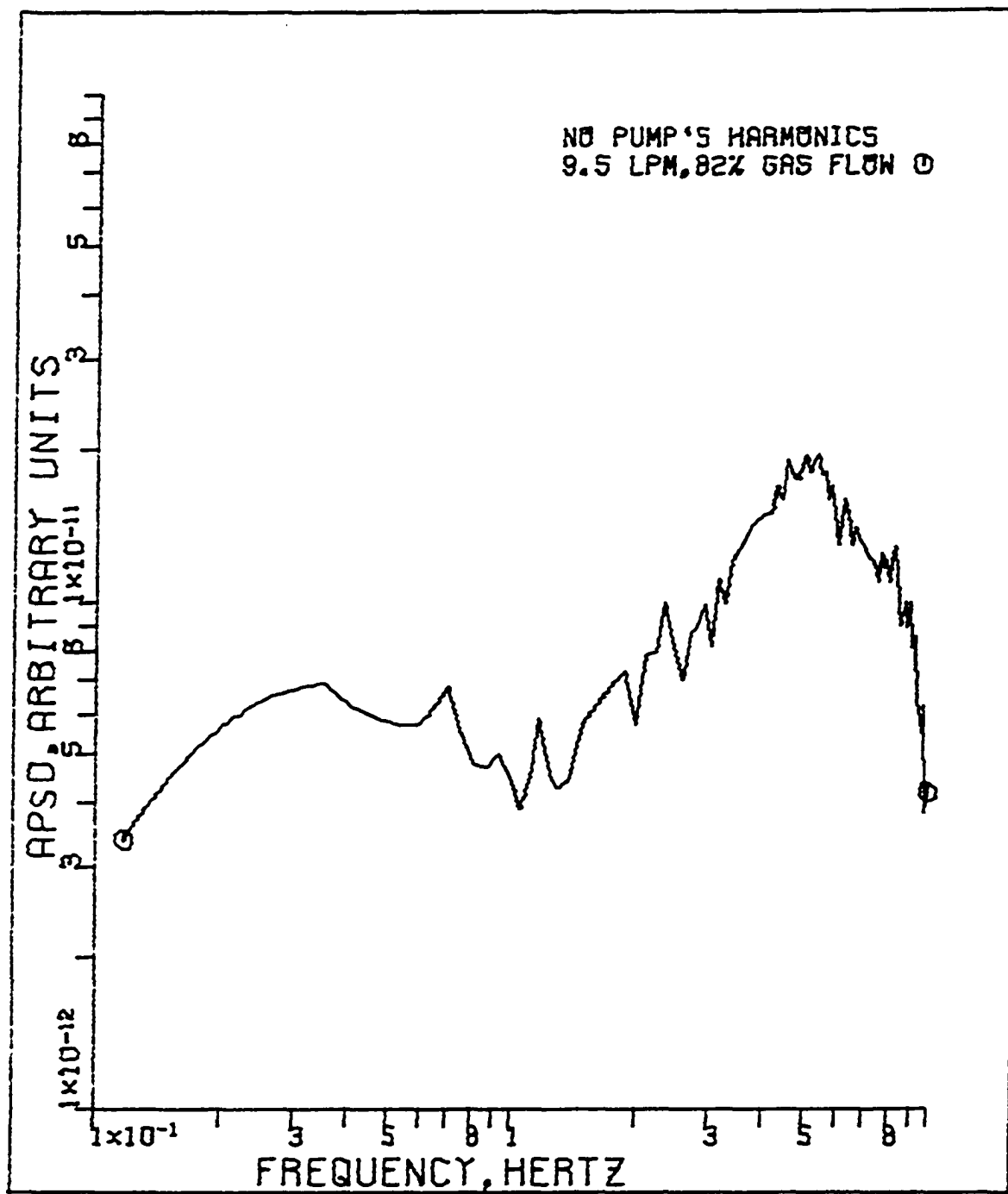


Figure 5.7. APSD for run 1-4-33 after the pump's harmonics were removed

## VI. RESULTS AND DISCUSSION

Measurements were performed, using the flow loop described in Chapter IV, with the objective of exploring the possibility of identifying a two-phase flow regime, in a reactor coolant channel through some unique structure in the noise spectra. To unravel the existence of these structures, a favorable signal to noise ratio must prevail throughout the measurements. It has been shown that the auto power spectral density (ASPD) for a delayed critical reactor [5, 15, 31, 104] consists of the detection noise which is proportional to the reactor power and the detector efficiency, the chain noise which is proportional to the reactor power and the square of the detector efficiency and the power noise which is proportional to the square of the product of the reactor power and detector efficiency. In this investigation, the power noise includes contributions from the bubble noise and the normal driving reactivities noise. In a low power reactor, such as the UTR-10, the driving reactivities should be small in the steady state situation [33, 40, 42]. It is possible then to create, through bubbling, a perturbation large enough to cause the bubbling noise to be dominant in the power noise component. The detection efficiency of the  $\text{BF}_3$  detectors employed is estimated to be approximately  $10^{-7}$  detection/fission and accordingly, the chain noise is negligible. In summary, the ASPD in a low power reactor consists essentially of the detection and the power noise components only

and that can be reduced to bubbling noise only.

Since the detection noise is proportional to the reactor power while the power noise is proportional to the square of the reactor power, at sufficiently high power the latter noise component will dominate. As outlined in Chapter V, this condition was met at a reactor power level of 500 watts.

#### A. Auto-power Spectral Density (APSD) Measurements

Tables 6.1 and 6.2 summarize the flow conditions for the experimental measurements. The velocity and void fractions of the gas phase that appear in Table 6.1 were calculated by means of the drift model [13, 121] as outlined in Chapter III. The flow regime descriptions in the test section were obtained from measurements in the out of pile test loop as described in Chapter IV.

Essentially, three distinct flow regimes were investigated, namely bubbly, churn and slug flow as were shown in Figure 4.4. Other important flow regimes such as annular and misty flow could not be reproduced in the present loop because it was found that to produce these flow conditions, an excessive pressure build-up in the gas flow lines was required.

Before proceeding to examine the individual APSD curves, it should be noted that detector A refers to the one near the lower portion while detector B refers to the one near the upper portion of the test section.

Table 6.1. Experimental two-phase flow data for the test loop

Run number	Water flow, LPM	Air flow, SLPM(%)	Calculated void velocity, cm/s lower sec	upper sec	Void fraction, % lower sec	upper sec
1-3-22	-	2.84(30)	12.8	26.8	.325	.618
1-3-23	-	7.66(80)	13.4	28.4	.481	.892
1-4-34	3.8	3.69(40)	20.7	58.9	.259	.367
1-4-35	3.8	7.66(80)	27.5	85.1	.410	.527
1-4-30	5.7	3.69(40)	24.1	72.0	.224	.299
1-4-31	5.7	7.66(80)	31.1	98.2	.366	.456
1-4-26	7.6	4.83(50)	29.3	92.7	.241	.304
1-4-27	7.6	8.23(85)	34.8	115.0	.345	.418
1-4-32	9.5	4.83(50)	32.1	103.9	.217	.281
1-4-33	9.5	7.95(82)	37.5	126.3	.308	.367

The measured APSD for run 1-3-22, 2.84 SLPM gas flow and no water flow, is shown in Figure 6.1. The standard error associated with the discrete points in this and all other subsequent spectra, which were based on thirty-six segment averages, is 16.67%. For this run, the flow was bubbly near detector A and slug near detector B. It should be noted that the spectrum for the bubbly flow, detector A, is essentially flat up to the break frequency of the reactor which is around 7 Hertz. However, as the flow changes to slug, as for detector

Table 6.2. Summary of experimental results

Run number	Flow regime		Peak position, Hz	
	lower section	upper section	lower section	upper section
1-3-22	MB+S <sup>a</sup>	MS+B	-	1.2±.3
1-3-23	S	S	1.2±.4	1.2±.3
1-4-34	B	MS+B	-	2.1±.4
1-4-35	MC+S <sup>b</sup>	MS+C	-	3.0±.5
1-4-30	C+B	C	-	-
1-4-31	MC+B	MS+C	-	3.6±.5
1-4-26	MC+B	MC+S	-	-
1-4-27	MC+S	MS+C	-	4.2±.7
1-4-32	B+C	MC	-	-
1-4-33	C	MS+C	-	4.9±1.

<sup>a</sup>B stands for bubbly flow and S for slug flow, while the prefix M in MB and MS, for example, characterizes the flow as mostly bubbly and mostly slug, respectively.

<sup>b</sup>C stands for churn flow.

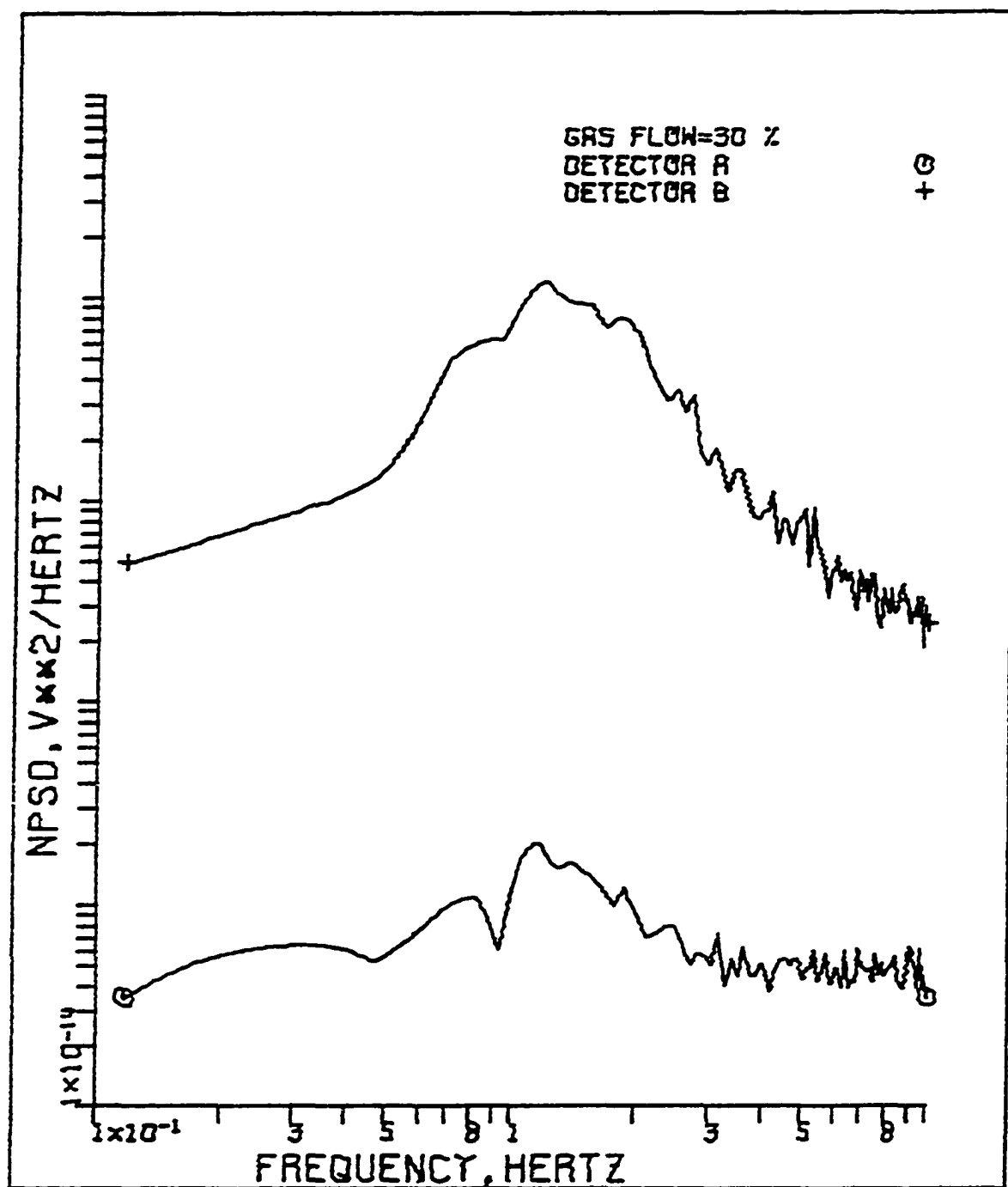


Figure 6.1. The measured APSD's, in stagnant water, for run 1-3-22

B, the spectrum appears to exhibit a broad response centered around 1.2 Hertz. When sufficient gas flow was introduced into the loop so that slug flow prevailed in the entire test section, the measured spectra from detectors A and B exhibited essentially the same broad response noted earlier for slug flow. These results are shown in Figure 6.2. The above results pertain to two-phase flow with the liquid phase being stagnant. Several measurements were also performed with forced circulation. The measured APSD for some typical runs are presented in Figures 6.3 - 6.5. The measured APSD for run 1-4-34, 3.8 LPM water flow and 3.69 SLPM gas flow, is shown in Figure 6.3. The flow was bubbly near detector A and mostly slug near detector B. The APSD for the bubbly flow is again flat and that for slug flow shows the familiar broad response that was associated with the slug flow of Figures 6.1 and 6.2. The peak, however, is shifted to a higher frequency of 2-3 Hz.

At this point it was felt essential to verify that the observed response was flow related and not due to other factors such as structures that may, for example, be associated with the pump harmonics. To this end, the APSD results from an experiment with forced circulation but no gas flow were compared to that with forced circulation and sufficient gas flow to produce a slug regime. Figure 6.6 displays the results obtained from detector B. The APSD associated with no gas flow shows a flat response that contrasts sharply with the

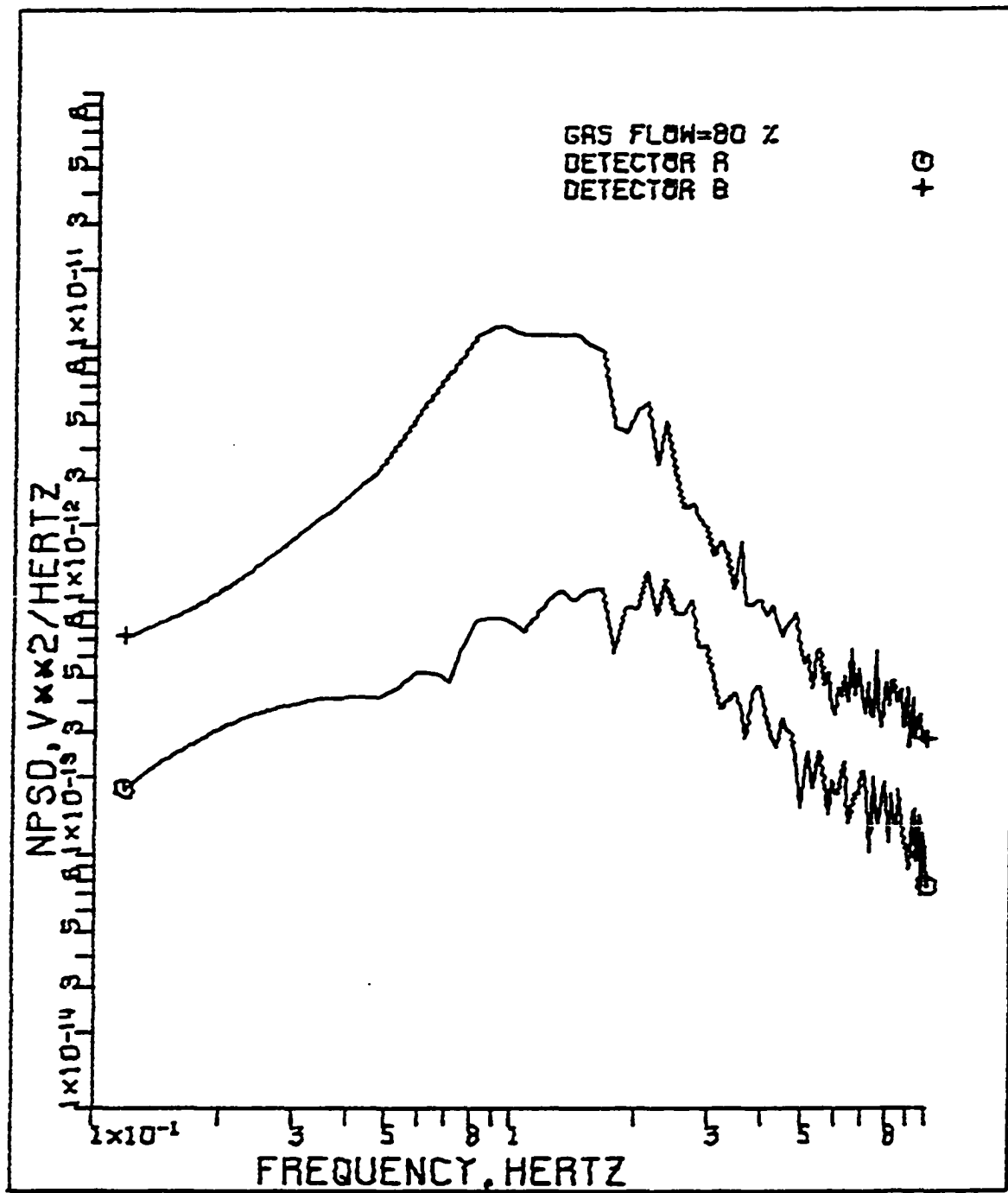


Figure 6.2. The measured APSD's, in stagnant water, for run 1-3-23

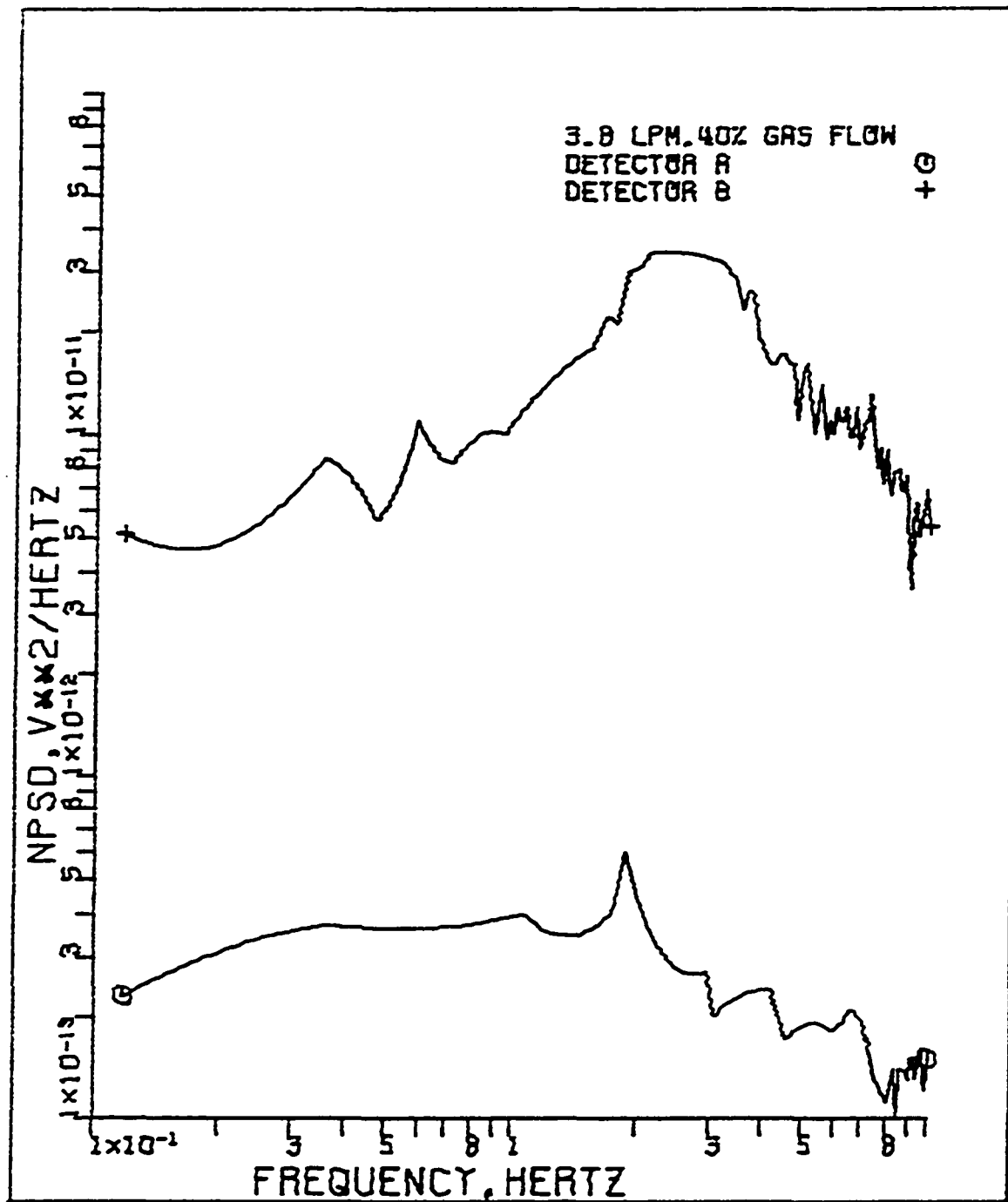


Figure 6.3. The measured APSD's, for forced circulation,  
for run 1-4-34

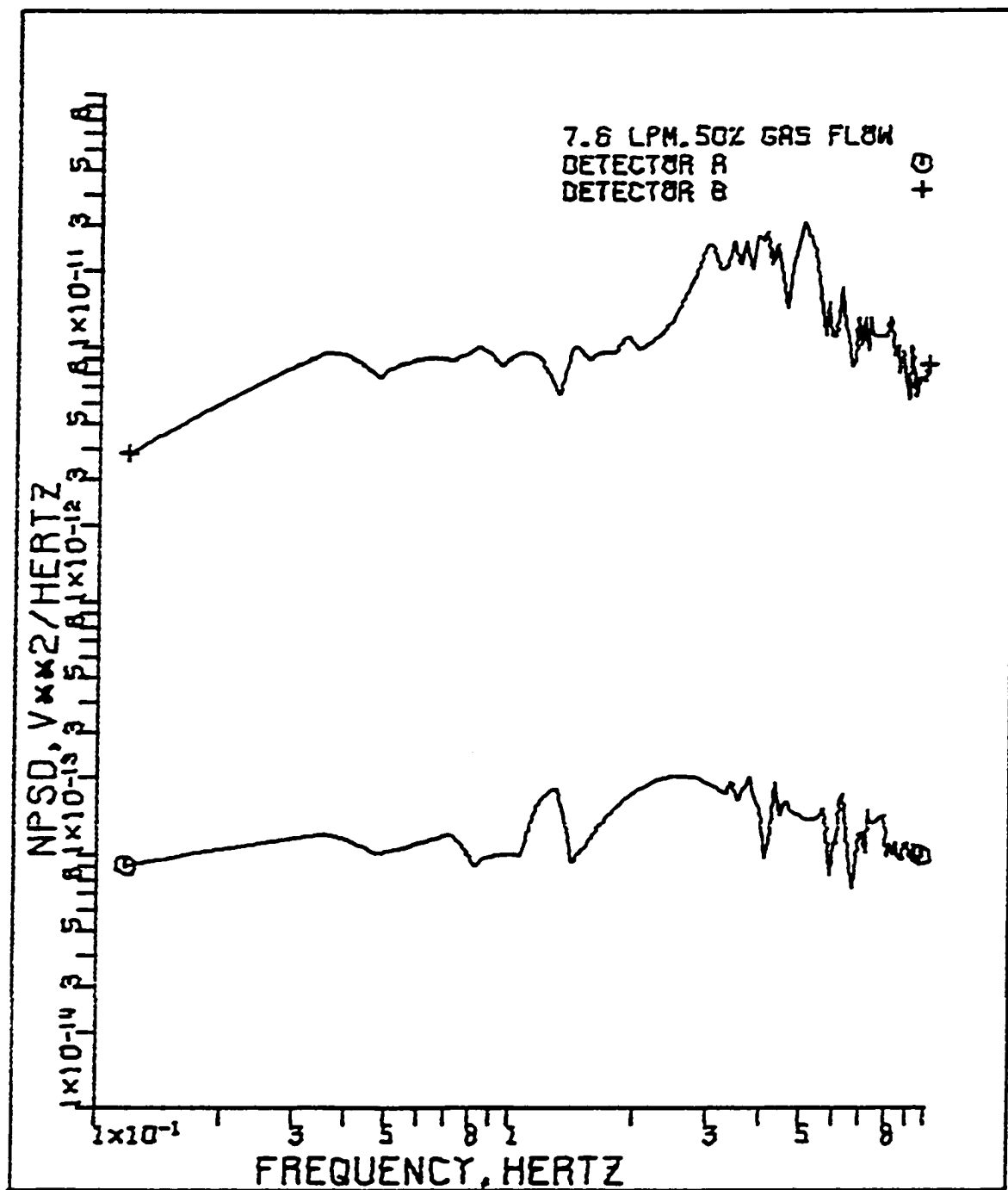


Figure 6.4. The measured APSD's, for forced circulation,  
for run 1-4-26.

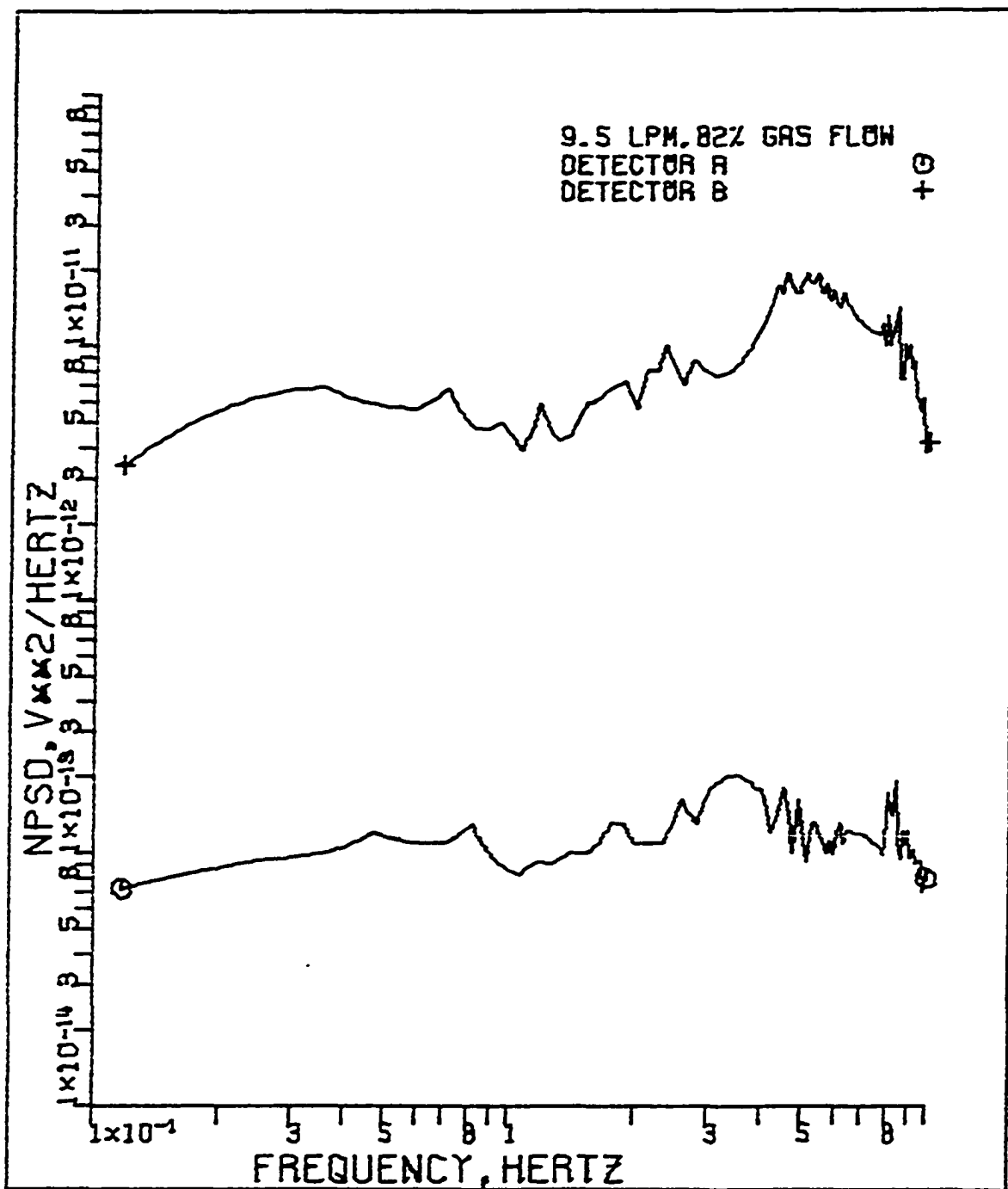


Figure 6.5. The measured APSD's, for forced circulation,  
for run 1-4-33

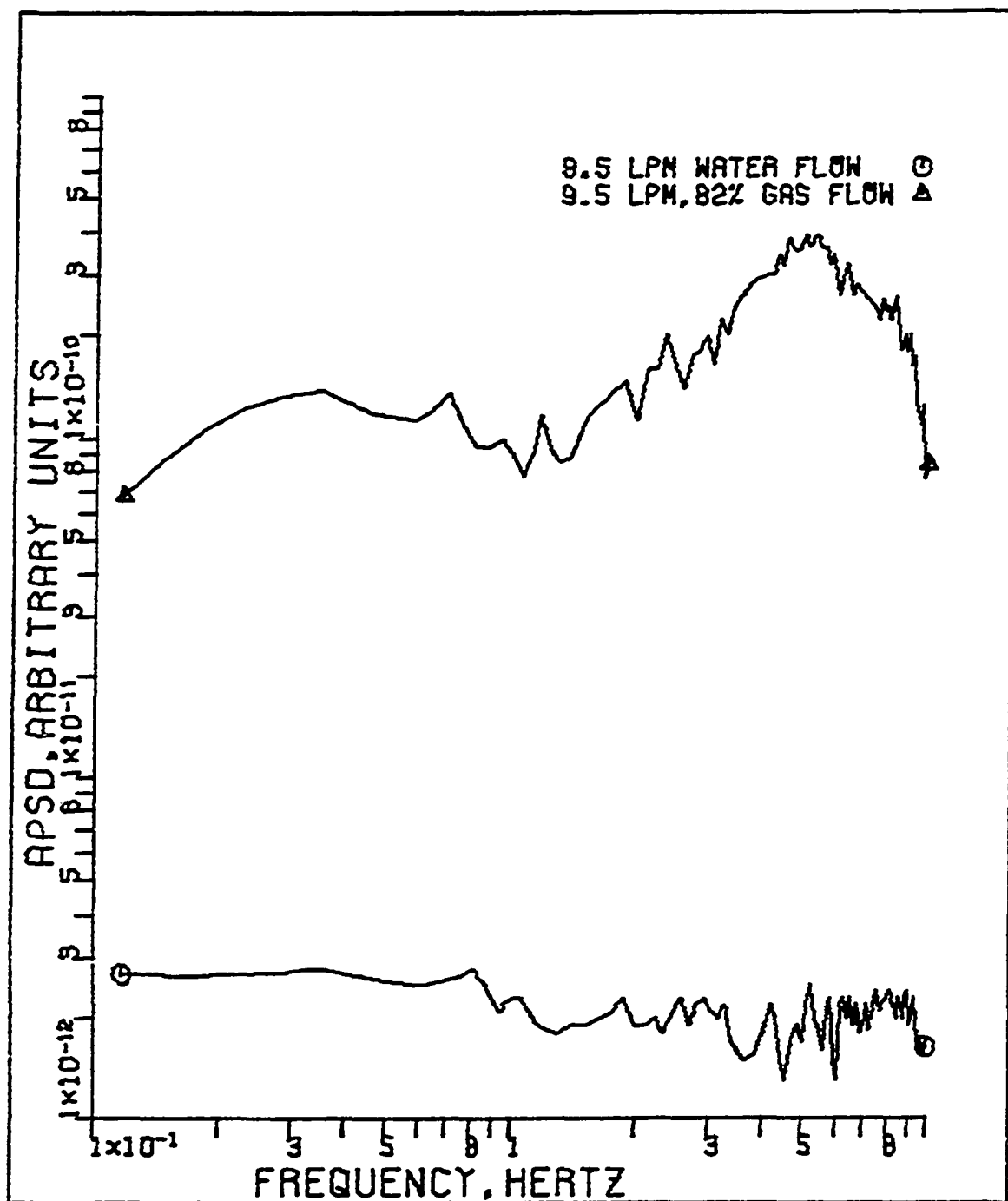


Figure 6.6. Comparison between the APSD's, for forced circulation, with and without void generation

prominent broad peaked response, centered around 4.9 Hertz, associated with that of gas flow. Consequently, it is concluded that the broad response is solely attributed to the presence of slug flow.

The results may now be presented in a more convenient form. The APSD curves for bubbly or a mixture of bubbly and churn flow are displayed in Figure 6.7. Evidently, the flat responses that were produced testify to the broad band characteristics of the noise field associated with these types of flow. The APSD curves for slug and a mixture of slug and churn flow are displayed in Figure 6.8, and show the unique broad peaked responses, that shifts to a higher frequency with increased fluid velocity, as discussed earlier. This behavior can be explained by the repetitive patterns that characterize slug flow, namely large cylindrical bubbles and liquid slugs passing alternately by the neutron detector. It is easy to imagine that the frequency response from such a pattern will be broad at low flow velocity and that it will tend to sharpen and shift to higher frequencies as the velocity of flow and hence the repetition rate is increased. The above findings may be summarized as follows:

The APSD that arises from bubbly and churn flow is, essentially, flat up to the break frequency of the reactor, while the APSD that arises from predominantly slug flow is characterized by a broad response centered around a frequency which is proportional to the voids velocity.

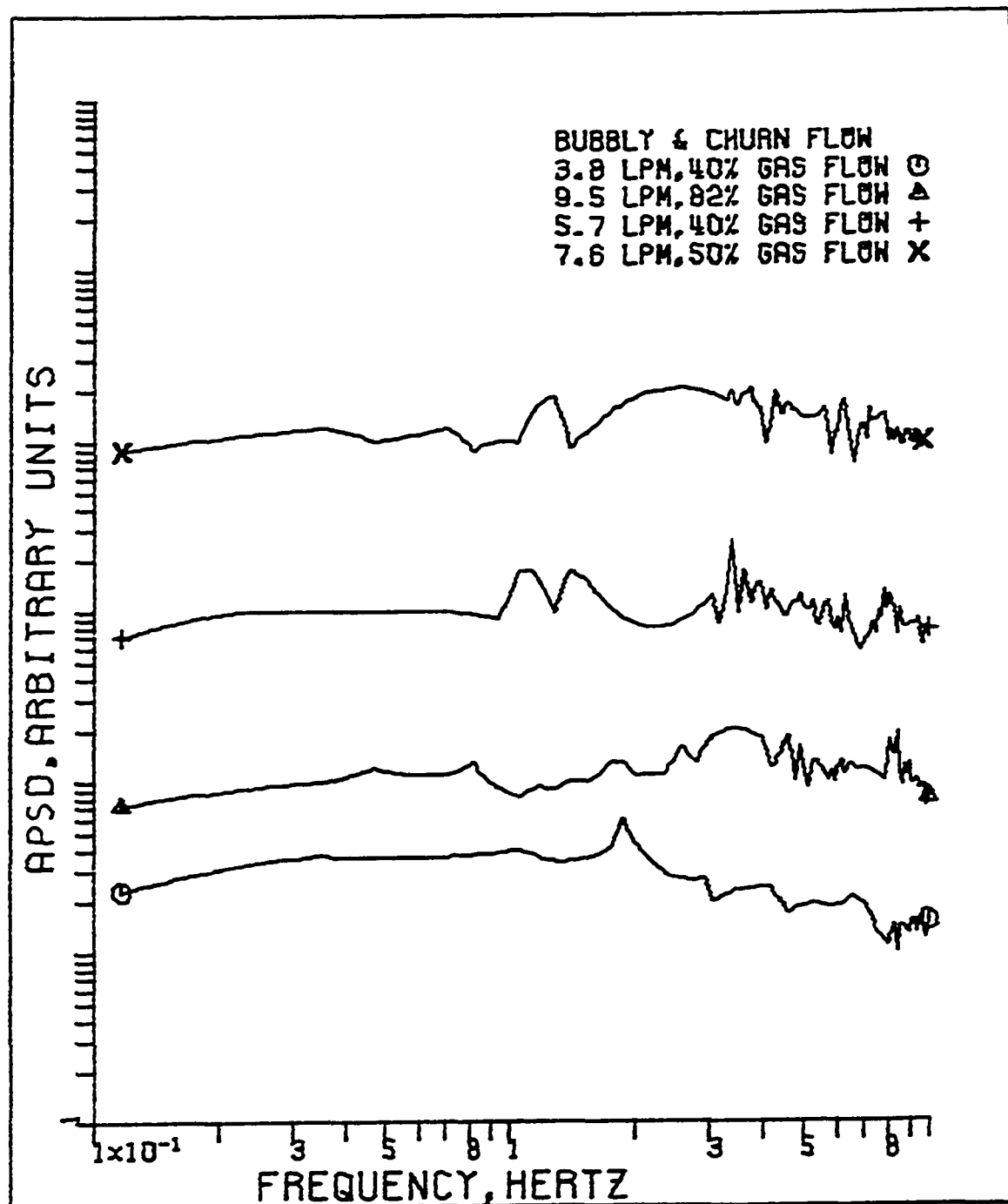


Figure 6.7. APSD's for predominantly bubbly flow at various water and gas flow rates

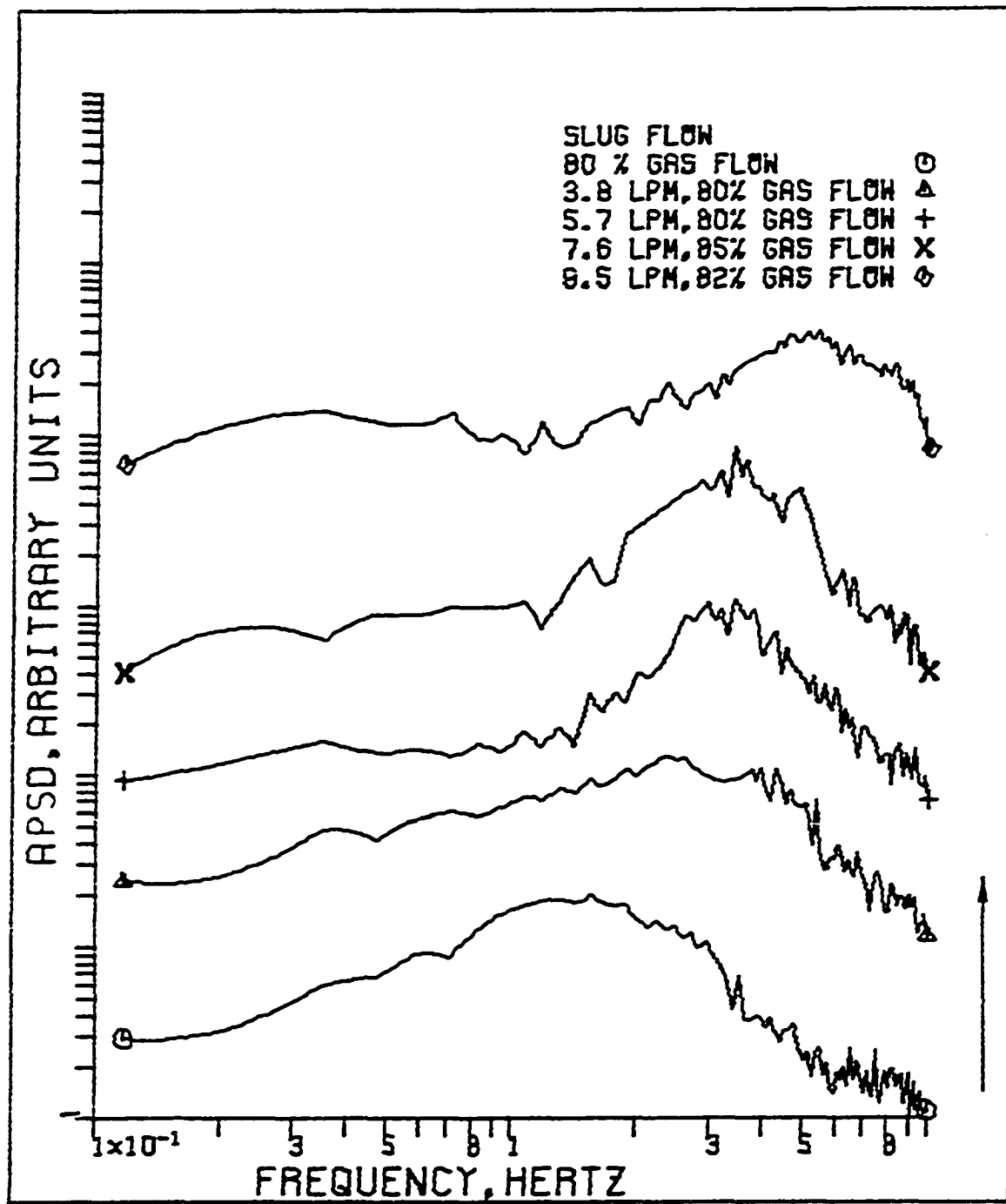


Figure 6.8. APSD's for predominantly slug flow at various water and gas flow rates

At this point, it was felt essential to investigate the origin, in the local-global context, of these flow related structures. To this end, run 1-4-31 was repeated with one detector, A, being replaced by a large Boron-lined compensated ion chamber that was placed in the south reflector, refer to Figure 4.1. The measured spectra are presented in Figure 6.9. The curves show that the broad peak, centered around 3.6 Hertz, is only seen by detector B which is near the test section, and not by the one in the reflector. This demonstrates clearly the local origin of the broad peaks. The localized flow related response of these detectors is significant in the sense that in-core ASPD measurements can be used to map the flow patterns inside a BWR reactor.

#### B. Comparison With Theory

Theoretical APSD computations were based on Equation (3-140). Essentially, two terms had to be evaluated before the indicated integration was carried out. The first term is the source term which was evaluated by the SOURCE code through programming Equations (3-90) through (3-95). A listing and description of the SOURCE code are presented in Appendix C. The second term is the frequency and space dependent adjoint function which was calculated by the CRAM code [47], a multi-group, multi-region, two-dimensional diffusion code. In applying this code, the complex adjoint equations were divided into a system for the real equations and a system for the

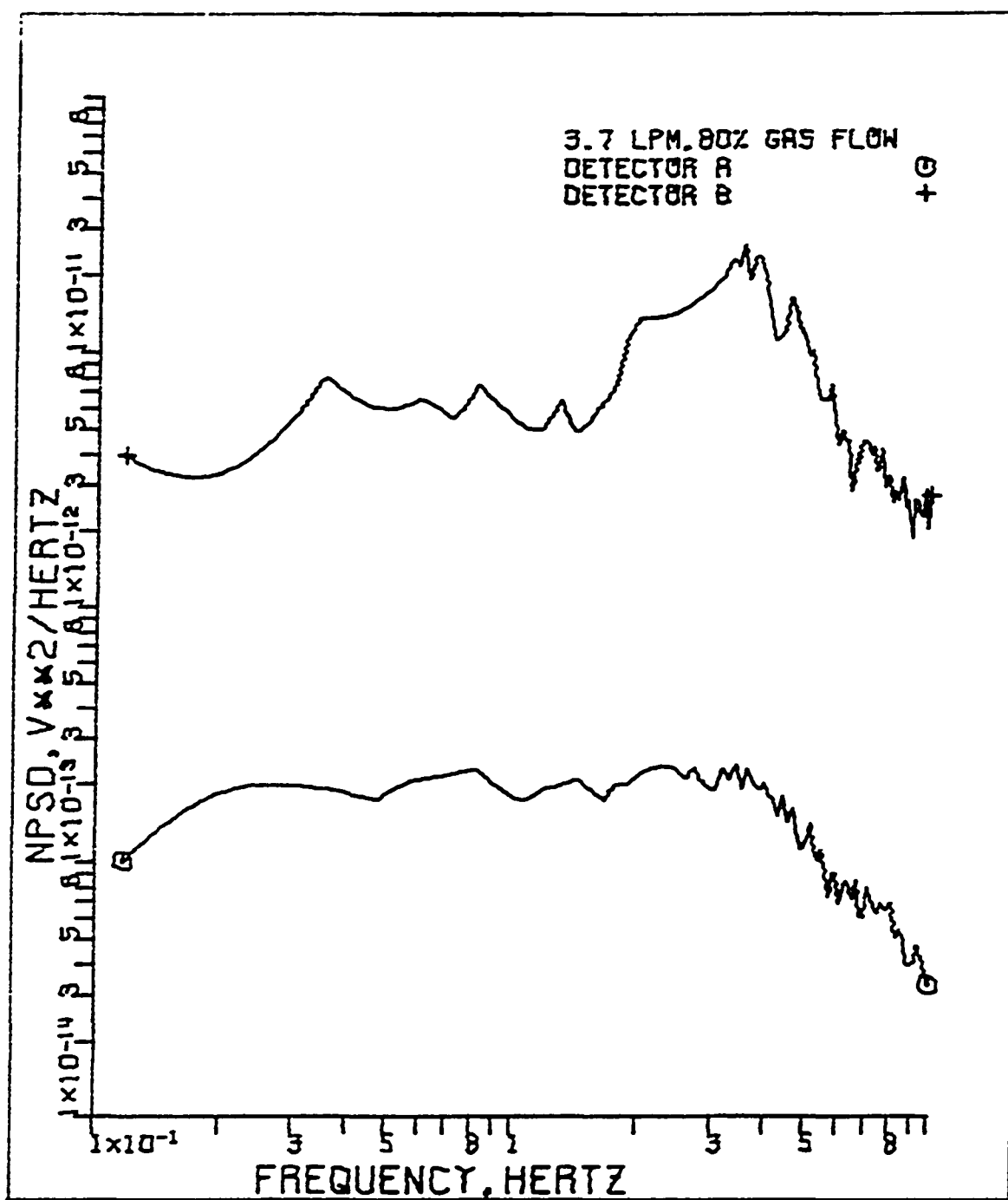


Figure 6.9. APSD's for slug flow as observed near the test section, detector B, and inside the south reflector of the UTR-10 reactor, detector A.

imaginary equations. The coupling terms from the real to the imaginary equations were treated as down scattering, and from imaginary to real as up scattering. Only the thermal adjoint source was considered and was simulated by a fictitious group as outlined in detail in Section C of Chapter III. Input data preparation, macroscopic cross sections, sample input data and results for the CRAM code are presented in Appendix B.

The theoretical APSD plots for slug flow at different void velocities are displayed in Figure 6.10. The general shapes of the theoretical and experimental APSD curves differ but both show the broad peak associated with the slug flow conditions. In order to examine the accuracy of the theoretical model in predicting the position of the broad peak for slug flow, these positions were plotted versus void velocity for both the theoretical and experimental results and are presented in Figure 6.11. The error (or deviation) bars indicate the estimated uncertainty margin in locating the experimental peak position. The close agreement, within the experimental error, between the experimental measurements and theoretical predictions are satisfactory. This observation suggests the possible accuracy that may be attained in establishing the void velocity of slug flow from the position of the peak in the measured APSD spectrum. In the environment of a BWR, the slip ratio can be accurately predicted [65, 102, 103]. Accordingly, once the void velocity has been established, the velocity

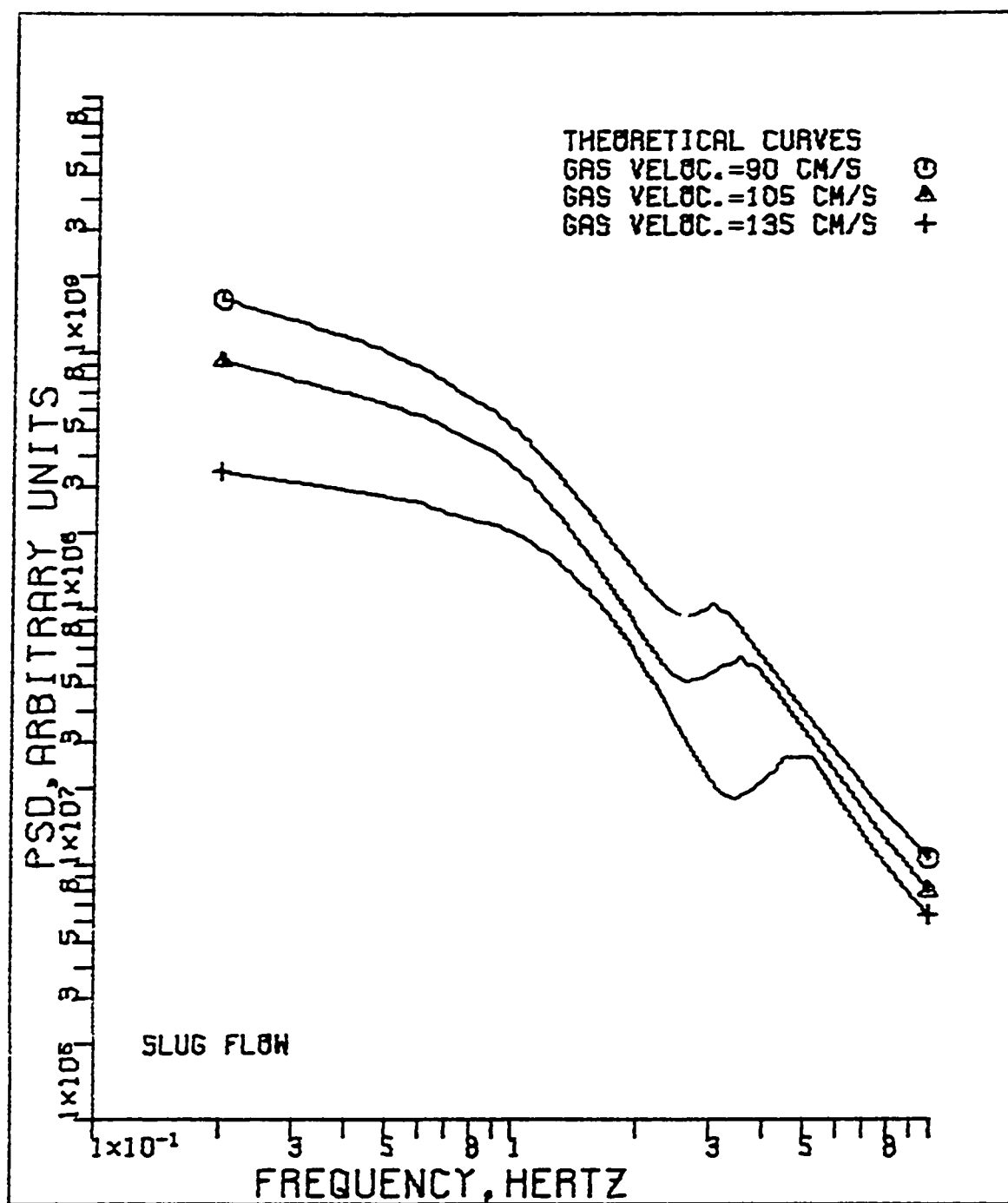


Figure 6.10. Theoretical APSD's for slug flow at various void velocities

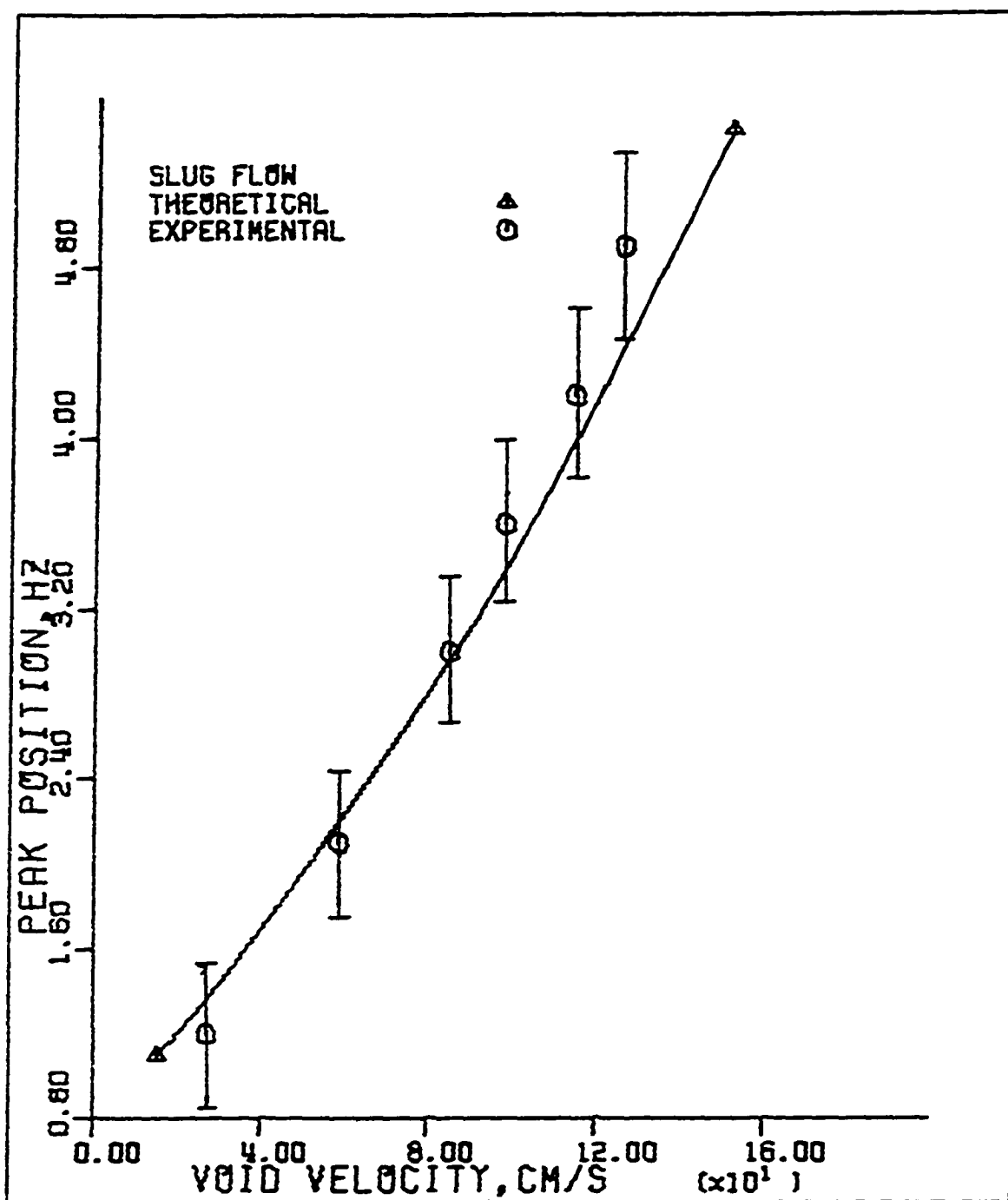


Figure 6.11. The peak position from the experimental and theoretical APSD's for different void velocities

of the liquid phase may be inferred. Applying a mass balance may thus yield another important flow parameter, namely the void fraction.

### C. The Cross-power Spectral Density (CPSD)

The magnitude and the phase of the CPSD for run 1-3-22 is shown in Figure 6.12. A reference to Table 6.2 reveals that for this run, slug flow prevailed in the entire test section. This fact explains the appearance of a prominent broad peak, around 1.2 Hertz, in the magnitude of the CPSD curve. This peak also attests to the strong correlation between the two detector signals over the frequency range subtended by the peak. However, the phase of the CPSD does not show any trend but in fact fluctuates randomly around zero. Similar behavior is in evidence in the theoretical CPSD's plots displayed in Figures 6.13 and 6.14. This is sharp contrast to the published results from BWR reactors [106, 112, 115, 117] which shows that the phase angle between two detectors, positioned along a coolant channel, are related linearly with frequency. The proportionality factor is in fact the transit time of the voids across the two positions. At this point, it should be noted that the phase of the CPSD of the voids, which was theoretically calculated and presented in Figure C.6 of Appendix C, show such linear dependence. This apparent discrepancy can be resolved in the following manner. According to Equation (3-139), the CPSD between two detectors is given by

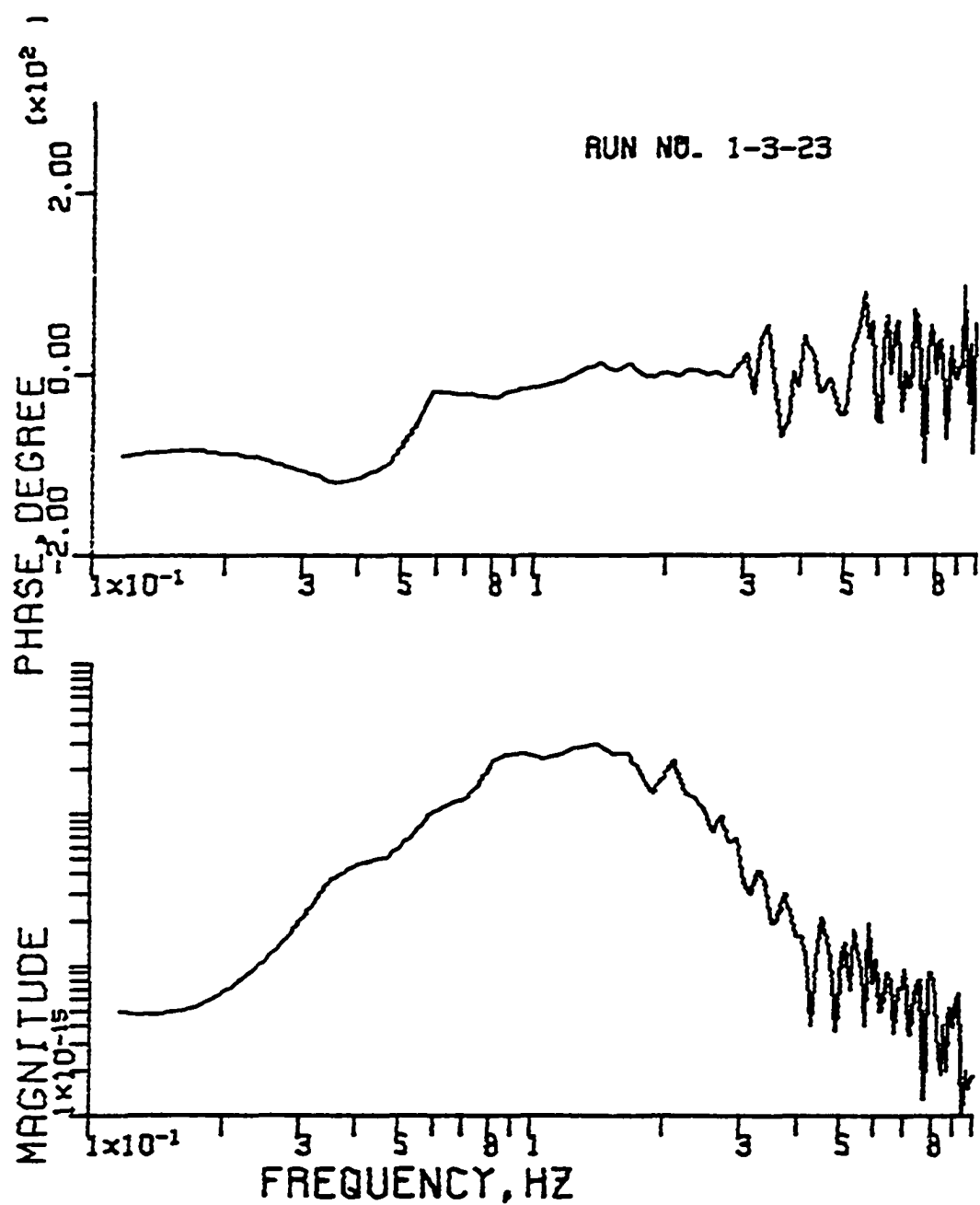


Figure 6.12. The magnitude and phase of the CPSD for run 1-3-23

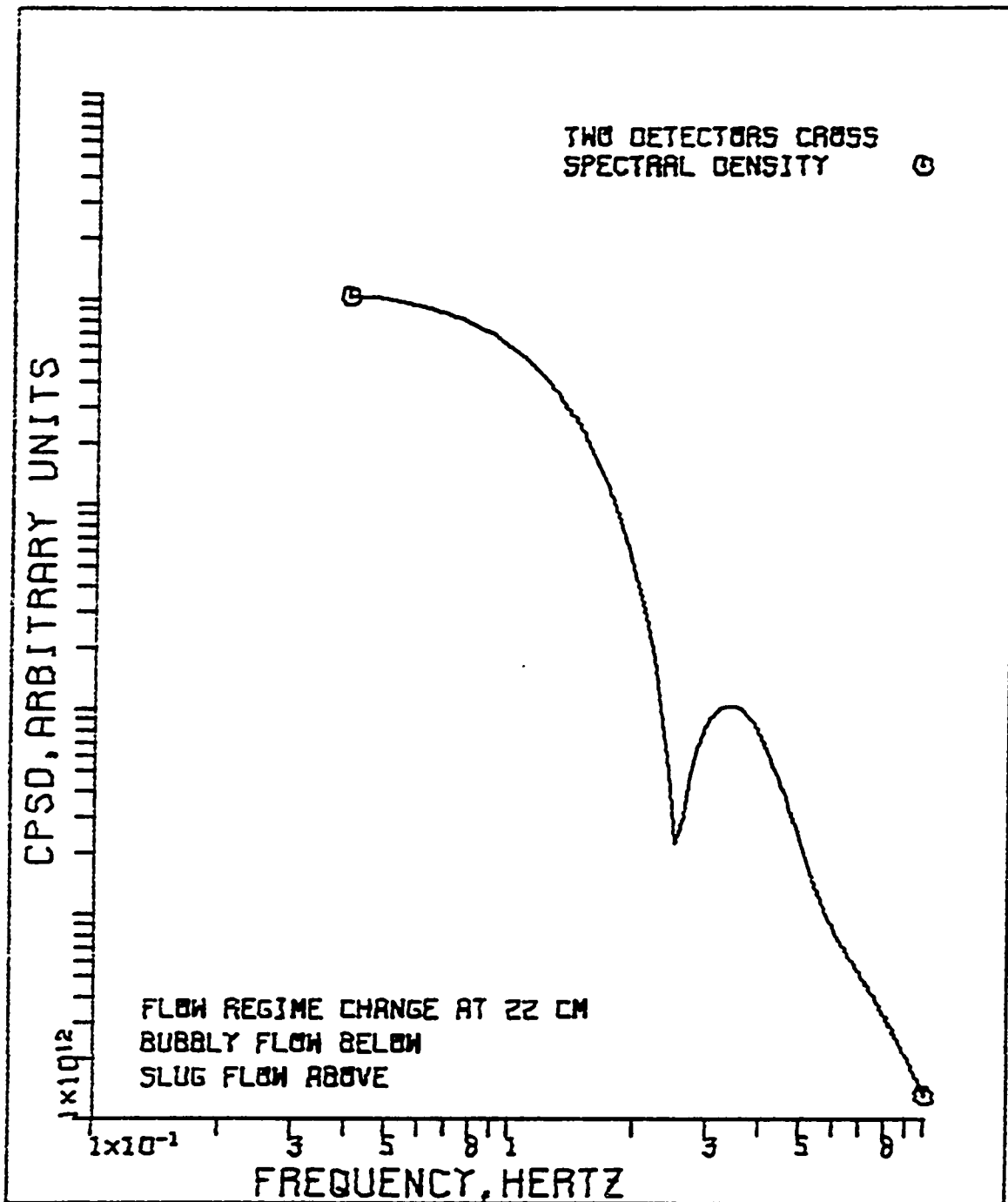


Figure 6.13. The magnitude of a typical CPSD calculation in the UTR-10 between two positions along the test section, 12 cm apart

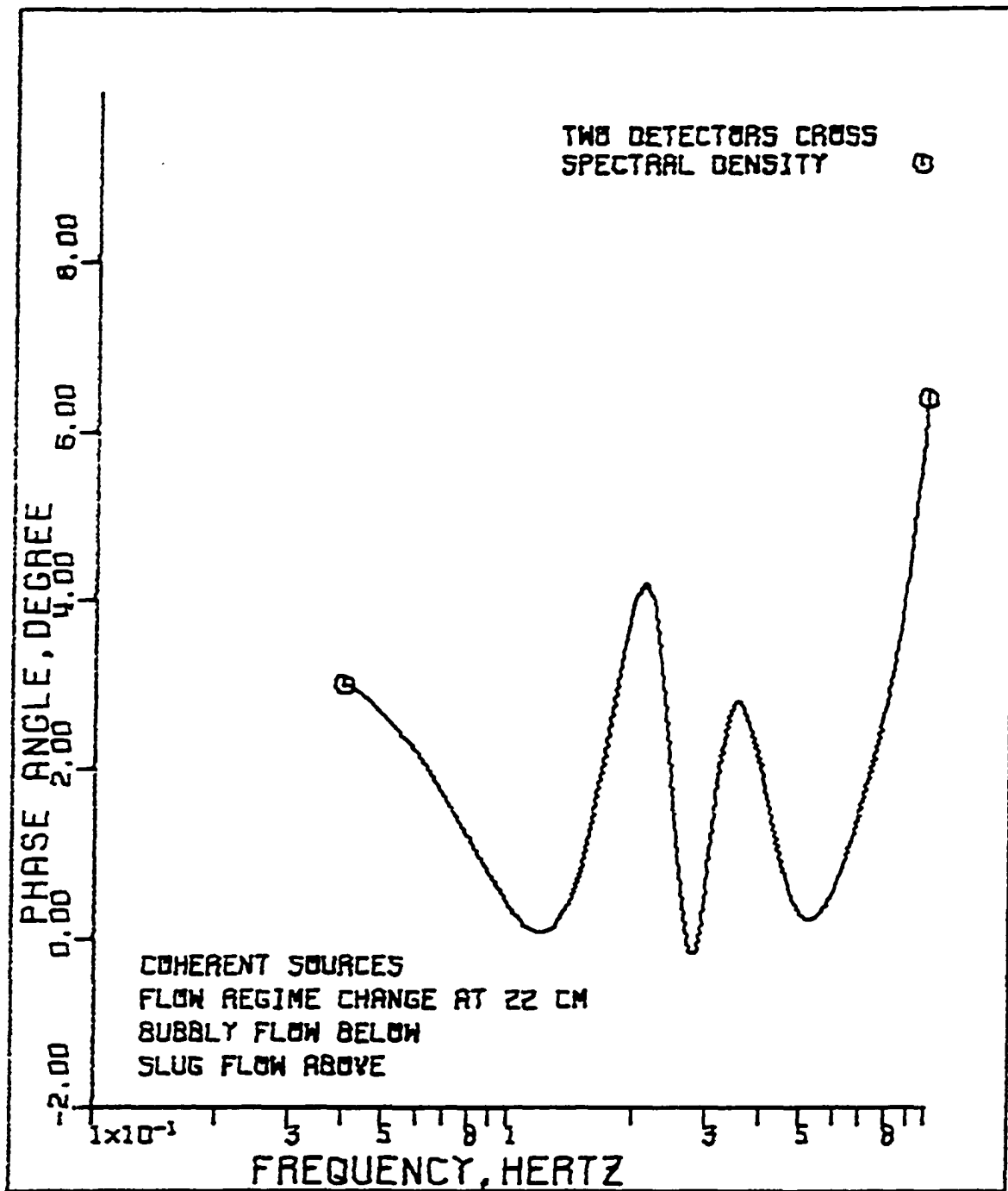


Figure 6.14. The phase angle of a typical CPSD calculation in the UTR-10 between two positions along the test section, 12 cm apart

$$C(\vec{r}_1, \vec{r}_2, \omega) = \langle S, \Psi_1 \rangle \langle \Psi_2, S \rangle \quad (6-1)$$

where  $\Psi_1$  and  $\Psi_2$  refer to the frequency and space dependent thermal adjoint functions of the reactor when the detector is in position 1 or 2. If the shape of the adjoint function peaks sharply at the detector position, then each of the inner products reduces essentially to the local component of the voids at the detector position. Accordingly, Equation (6-1) becomes

$$C(\vec{r}_1, \vec{r}_2, \omega) = S^*(\vec{r}_1, \omega) S(\vec{r}_2, \omega) = \text{The local CPSD of the voids.} \quad (6-2)$$

The above inequality becomes an equality if the adjoint shapes are delta functions at the detector positions. This relation indicates that the CPSD between two detectors should have the phase relation of the local CPSD component. The adjoint functions for this experiment are shown in Figure B.7 of Appendix B. Ignoring the small peaks at the detector positions, the shapes of the adjoint functions are essentially similar and peak at the center of the reactor. For this situation, Equation (6-2) becomes

$$C(\vec{r}_1, \vec{r}_2, \omega) \stackrel{\Delta}{=} |S(0, \omega)|^2. \quad (6-3)$$

This CPSD is a real number and consequently has no phase angle. The above argument provides a qualitative explanation of the absence of any phase information from the CPSD of Figures 6.12 and 6.14. A quantitative analysis [97] shows that for a transit perturbation, described by  $e^{-j\omega z/V}$  and

traveling with constant velocity,  $v$  in a one dimensional one group reactor, the CPSD between two detectors has a phase shift given by

$$\theta = -\omega\tau , \quad (6-4)$$

where  $\tau$  is the modified void transit time between the two detectors and is defined as

$$\tau = \frac{z_2 - z_1}{v} , \quad (6-5)$$

and where  $z_1$  and  $z_2$  refer to the position of the centroid for detector 1 and detector 2 adjoint functions respectively. An examination of Figure B.7 reveals that for the UTR-10 experiment,  $z_1$  and  $z_2$  are essentially equal and subsequently, the slope  $\tau$  is nearly zero as the experimental and theoretical curves of Figures 6.12 and 6.14 indicate.

## VII. CONCLUSIONS

The main objectives of this work were to investigate the possibility of identifying experimentally two-phase flow patterns in a coolant channel through the corresponding neutron noise spectra, and to provide a realistic model which describes the shapes of the noise spectra that arise from different flow regimes. It was found that the repetitive patterns, of large gas bubbles and water slugs, which are normally associated with slug flow, give rise to an PSD with a distinct broad peak that is centered around a given frequency. This frequency depends on the prevalent void flow velocity inside the channel. On the other hand, the observed spectra for bubbly and churn flow conditions were featureless up to the upper cut-off frequency of the experimental analysis (12.5 Hz). The theoretical model, which was developed for this investigation, is based on a more realistic treatment of the neutronic and flow hydraulics of the channel than those developed by other investigators [2, 9, 14, 16, 17, 28, 60, 69, 70, 78, 94, 102-104, 110, 120]. More specifically, the present model incorporates the following details:

1. The hydraulic modeling computations, along the channel, were based on a one-dimensional mass and momentum balance equations that explicitly dealt with either of two flow regimes; namely bubbly and churn or slug flow.
2. The neutronic modeling computations were based on a

two group, two-dimensional adjoint formulation. The resulting adjoint response, which was treated as a complex quantity, is both space and frequency dependent. The model also accounts for the location and size of the detectors and an arbitrary noise source distribution.

The main conclusions of the present work may be stated as follows:

1. Of the three reactor noise sources, detection, chain, and power noise, only the power noise prevails at sufficiently high power levels (for the UTR-10, and conditions for this experiment, this power is approximately 500 watts). By operating the reactor at a power level so that the power noise is dominant, a favorable signal to noise ratio (a value of 5) results, which increase the ease with which noise spectra from specific and controlled disturbances may be studied.
2. The two-phase bubbly flow has identical noise characteristics compared to the one-phase liquid flow, namely a white noise spectrum. However, as is clear in Figure 5.1, the magnitude of the APSD for bubbly flow is about ten times higher than that for liquid flow only. Accordingly, this fact may be used readily to distinguish between bubbly flow and liquid flow.

3. Slug flow can be easily detected from the presence or appearance of a distinct peak in the measured APSD. The position of the peak is very sensitive to the bubble velocity in the channel.
4. The theoretical model, that was developed, may be applied to compute a calibration curve for the position of the peak for slug flow versus bubble velocity. This curve can be used to map the velocity profile in a coolant channel.
5. A static multi-group, multi-dimensional code, such as the CRAM code, may be used successfully to predict the reactor response via the adjoint space formulation. If the calculations are carried out in the normal way, as opposed to the adjoint space, severe convergence problems will be encountered as reported by Cohn [23]. The different convergence rates for the two formulations can be explained as follows: The adjoint space formulation gives rise to the adjoint response which, for each energy group, has a positive phase angle. Thus, its inphase and quadrature components are both positive and the convergence rate is expected to be fast. On the other hand, the reactor response, which is related to the complex conjugation of the adjoint response, has a negative phase angle (indicating that the output response lags the input) which implies that its inphase and quadrature components are of opposite

signs and hence convergence is more difficult to achieve.

6. The phase information contained in the CPSD measurement in a small reactor (e.g. UTR-10), does not yield any useful parameters (due, as outlined in Section C of Chapter VI, to the fact that the adjoint response of either detector is not well-defined and hence the centroidal distance of either of the adjoint responses is essentially the same). This is in sharp contrast to the corresponding phase measurements in a large BWR reactor [67, 61]. Such measurements show a linear dependence, between phase and frequency, with a slope given by the transit time of the bubbles across the two positions. Thus, the velocity of the bubbles can be easily deduced.

## VIII. SUGGESTIONS FOR FUTURE WORK

In an effort to extend the scope, improve the methodology and avoid some of the pitfalls encountered in this work, the following suggestions are intended as a general guide to future work in this area:

1. The detector response model due to two-phase stochastic flow, predicted the correct peak position for slug flow but fell short in reproducing the observed shapes of the APSD's. A remedy to this situation may lie in improving the two phase hydraulic model. One such improvement may involve the development of a model that accounts for the size and shape of the bubbles, which implies a two dimensional model.
2. The loop design can be modified, appropriately, to create annular and misty flow regimes so that their spectra may be observed and studied.
3. The pump, which is presently employed in the loop, introduced undesirable harmonics in the APSD (in the frequency range 0-12 Hz). This can be easily remedied by replacing the pump with an impeller type, which has a characteristically high r.p.m. (>1800 r.p.m.), and thus all the pump harmonics will be well-beyond the frequency region of interest.
4. The versatility of the data acquisition system can be further extended with the following additions:

- a. The incorporation of a real time clock in the MSI-6800 computer to replace the present sampling rate mechanism which is software controlled. This addition will obviously result in a more accurate control over the sampling rate mechanism.
- b. Upgrading the MSI-6800 memory bank (by 8k at least) in order to double the maximum length of the time record with subsequent improvements in the frequency resolution and the computing efficiency of the FFT.
- c. Incorporating a compact high pass filter with a fixed cut-off frequency, in the signal conditioning portion of the electronics, in order to eliminate signal drift.
- d. Replacing the 8-bits analog to digital converter (ADC) to a 12-bits ADC. This addition will improve the dynamical range [26, 39, 56] of the system by one and a half times, from 54.4 to 78.3 db.

## IX. LITERATURE CITED

1. Akcasu, A. Z. 1960. Theoretical feedback analysis in boiling water reactors. USAEC Report ANL-6221. (Argonne National Laboratory, Lemont, Ill.)
2. Akcasu, A. Z., and R. K. Osborn. 1966. Application of Langevin's technique to space and energy dependent noise analysis. Nucl. Sci. Eng. 26:13-25.
3. Albrecht, R. W. 1972. The use of signal coherence for anomaly detection in nuclear reactors. Nucl. Technol. 14:208-217.
4. Analytis, G. T. 1978. Investigation of the space-dependent global component of the neutron to inlet coolant temperature fluctuations transfer function. Ann. Nucl. Energy 5:597-612.
5. Ando, Y., and N. Naito. 1975. Void detection in BWR by noise analysis. J. Nucl. Sci. Technol. 12(9):597-599.
6. Ashraf, A., J. E. Mott, and D. N. Fry. 1976. Determination of void fraction in BWRs using noise analysis. Trans. Am. Nucl. Soc. 22:466-468.
7. Ashraf, M. A., and D. N. Fry. 1978. Determination of void fraction profile in a boiling water reactor channel using neutron noise. Nucl. Sci. Engr. 66(2):264-268.
8. Beckjord, E. S. 1958. Dynamic analysis of natural circulation boiling water power reactors. USAEC Report ANL-5799. (Argonne National Laboratory, Lemont, Ill.)
9. Behringer, K., and G. Kosaly. 1979. Linear response of the neutron field to a propagating perturbation of moderator density (two-group theory of boiling water reactor noise). Nucl. Sci. Engr. 72:304-321.
10. Behringer, K., G. Kosaly, and L. Kostic. 1977. Theoretical investigation of the local and global components of the neutron noise field in a BWR. Nucl. Sci. Engr. 63: 306-318.
11. Bell, G. I., and S. Glasstone. 1970. Nuclear reactor theory. 1st ed. Van Nostrand Reinhold Company, New York. 637 pp.

12. Bendat, J. S., and A. G. Piersol. 1971. Random data: Analysis and measurement procedures. John Wiley and Sons, Inc., New York. 397 pp.
13. Binder, R. C. 1973. Fluid mechanics. Prentice-Hall, Inc., Englewood Cliffs, N.J. 400 pp.
14. Binford, F. T. 1965. Boiling detection experiment. Pages 30-34 in Oak Ridge Research Reactor Quarterly report, April, May, June 1965. ORNL-TM-1290. (Oak Ridge National Laboratory, Oak Ridge, Tenn.)
15. Blevins, R. D. 1977. Flow induced vibration. Van Nostrand Reinhold Company, New York. 363 pp.
16. Blomberg, P. E., and F. Akerhielm. 1975. A contribution to the experience of noise measurements and analysis in BWR power plants. Annals of Nuclear Energy 2:323-331.
17. Bonnet, J. A., Jr., and R. K. Osborn. 1971. Neutronic-acoustic detection of the onset of bulk boiling in liquid sodium. Nucl. Sci. Engr. 45:314-320.
18. Boure, J. A., A. E. Bergles, and L. S. Tong. 1973. Review of two phase flow instability. Nucl. Engr. Design 25: 165-192.
19. Boyd, L. R. 1956. Detection of nucleate boiling by flux variation measurement. USAEC Report KALP-M-LRB-3. (Knolls Atomic Power Laboratory, Schenectady, N. Y.)
20. Butterworth, D., and G. F. Hewitt. 1977. Two-phase flow and heat transfer. Oxford University Press, New York. 514 pp.
21. Clark, M., Jr., and K. F. Hansen. 1964. Numerical methods of reactor analysis. 1st ed. Academic Press, New York. 340 pp.
22. Cohn, C. E. 1960. A simplified theory of pile noise. Nucl. Sci. Engr. 7:472-475.
23. Cohn, C. E. 1966. Calculating space-dependent reactor transfer functions using statics techniques. Nucl. Sci. Engr. 26:198-206.
24. Colomb, A. L., and F. T. Binford. 1962. The detection of boiling in a water-cooled reactor. ORNL-TM-274. (Oak Ridge National Laboratory, Oak Ridge, Tenn.)

25. Cooley, J. W., and J. W. Tukey. 1965. An algorithm for machine calculation of complex Fourier series. *Math. Computations* 19:144-154.
26. Cooper, G. R., and C. D. McGillen. 1971. Probabilistic methods of signal and system analysis. Holt Rinehart and Winston, Inc., New York, N.Y. 142 pp.
27. Dam, H. V. 1975. A perturbation method for analysis of detector response to parametric fluctuations in reactors. *Atomkernenergie* 25:70-71.
28. Dam, H. V. 1976. Neutron noise in boiling water reactors. *Atomkernenergie* 27:8-14.
29. Dam, H. V. 1977. On adjoint space in reactor noise theory. *Ann. Nucl. Energy* 4:185-188.
30. Danofsky, R. A. 1969. A space-dependent reactor-noise formulation utilizing model expansions. *Nucl. Sci. Engr.* 36:28-38.
31. Debosscher, A. F., and W. L. Dutre. 1979. Exact statistical analysis of nonlinear dynamic power reactor models by the Fokker-Planck method-II,III. *Nucl. Sci. Engr.* 69:347-353, 354-362.
32. DeShong, J. A., Jr., and W. C. Lipinski. 1958. Analysis of experimental power-reactivity feedback transfer functions for a natural circulation boiling water reactor. USAEC Report ANL-5850. (Argonne National Laboratory, Lemont, Ill.)
33. Dutre, W. L., and A. F. Debosscher. 1977. Exact statistical analysis of nonlinear dynamic nuclear power reactor models by the Fokker-Planck method-part I: Reactor with direct power feedback. *Nucl. Sci. Engr.* 355-363.
34. Fleck, J. A. 1960. The dynamic behavior of boiling water reactors. *J. Nucl. Energy* 11:114-130.
35. Fowler, T. R., M. L. Tobias, and D. R. Vondy. 1965. Exterminator-A multigroup code for solving neutron diffusion equations in one and two dimensions. USAEC Report ORNL-TM-842 (Oak Ridge National Laboratory, Tenn.)
36. Fry, D. N. 1971. Experience in reactor malfunction diagnosis using on-line noise analysis. *Nucl. Technol.* 10: 273-281.

37. Fuge, R., and J. Valko. 1977. Measurement of the local and global effect on bubbles in a water moderated reactor. *Ann. Nucl. Energy* 4:161-167.
38. Gebureck, K., O. Singh, and D. Stegemann. 1977. Experimental and theoretical noise analysis investigations in boiling water reactors. *Progress in Nucl. Energy* 1:187-203.
39. Gelb, A., ed. 1975. Applied optimal estimation. 1st ed. The MIT Press, Cambridge, Mass.
40. Genoud, J. P. 1979. Importance of the noise sources in the coupling medium of a coupled core system. *Ann. Nucl. Energy* 6:489-493.
41. Greenspan, E. 1976. On the adjoint space in reactor theory. *Ann. Nucl. Energy* 3:323-327.
42. Greenspan, E. 1976. Perturbation theory and importance functions in integral transport formulations. *Nucl. Sci. Engr.* 61:170-179.
43. Griffin, C. W., and R. L. Randall. 1963. At power, low-frequency, reactor-power-spectrum measurements and comparison with oscillation measurements. *Nucl. Sci. Engr.* 15: 131-138.
44. Hannaman, G. W., and R. A. Danofsky. 1975. In-core neutron detector response model based on basic principles. *Transactions of the American Nuclear Society* 21:479.
45. Harms, A. A., and C. F. Forrest. 1971. Dynamic effects in radiation diagnosis of fluctuating voids. *Nucl. Sci. Engr.* 46:408-413.
46. Harms, A. A., S. Lo, and W. T. Hancox. 1971. Measurement of time-average voids by neutron diagnosis. *J. Appl. Physics* 42(10):4080-4082.
47. Hassitt, A. 1962. A computer program to solve the multi-group diffusion equations. UKAEC Report TRG-229(R). (United Kingdom Atomic Energy Authority, Risley.)
48. Hendrickson, R. A., and G. Murphy. 1968. Cross-spectral density measurements in a coupled-core reactor. *Nucl. Sci. Engr.* 31:215-221.
49. Hetrick, D. L. 1971. Dynamics of nuclear reactors. 1st ed. The University of Chicago Press, Chicago, Ill. 542 pp.

50. Hildebrand, F. B. 1965. Methods of applied mathematics. 2nd ed. Prentice Hall, Inc., Englewood Cliffs, N. J. 537 pp.
51. Houghton, G. 1961. Some theoretical aspects of vapor void formation in heated vertical channels. Nucl. Sci. Engr. 11:121-128.
52. Houghton, G. 1962. An analysis of vapor profiles in heat channels. Nucl. Sci. Engr. 12:390-397.
53. Hsu, Y., and R. W. Graham. 1976. Transport processes in boiling and two-phase systems. 1st ed. McGraw Hill, San Francisco. 493 pp.
54. Huang, L. R. 1979. Use of adjoint space models for predicting the response of a neutron detector to core parametric fluctuations. Unpublished Ph.D. thesis. Ames, Iowa, Library, Iowa State University.
55. Jordon, E. L. 1966. Detection of in-core void formation by noise analysis. Am. Nucl. Soc., Trans. 9:317-318.
56. Kerlin, T. W. 1974. Frequency response testing in nuclear reactors. 1st ed. Academic Press, New York. 231 pp.
57. Kleiss, E., and H. V. Dam. 1977. Analysis of neutron detector response to bubbles in a water moderated reactor. Ann. Nucl. Energy 6:385-398.
58. Kosaly, G. 1973. Remarks on a few problems in the theory of power reactor noise. Nucl. Energy 14(3):67-73.
59. Kosaly, G., and L. Mesko. 1976. Theory of the auto-spectrum of the local component of power-reactor noise. Ann. Nucl. Energy 3(4):233-236.
60. Kosaly, G., L. Kostic, and G. Varadi. 1977. Investigation of the local component of the neutron noise in a BWR and its application to the study of two-phase flow. Progress Nucl. Energy 1:99-117.
61. Kosaly, G., L. Morati, and L. Mesko. 1975. A simple space dependent theory of the neutron noise in a boiling water reactor. Ann. Nucl. Energy 2:315-321
62. Lahey, R. T., Jr., and F. J. Moody. 1978. The thermal hydraulics of a boiling water nuclear reactor. 1st ed. American Nuclear Society, LaGrange Park, Ill. 433 pp.

63. Landau, L. D., and E. M. Lifschitz. 1977. Quantum Mechanics. 3rd revised edition. Biddles Ltd., Surrey. 473 pp.
64. Lax, M. 1960. Fluctuations from the nonequilibrium steady state. *Rev. Mod. Phys.* 32:25-57.
65. Levy, S. 1967. Forced convection subcooled boiling-prediction of vapor volumetric fraction. *Inter. J. Heat and Mass Transfer* 10:951-965.
66. Lewins, J. 1965. Importance - The adjoint function. 1st ed. Pergamon Press, New York. 311 pp.
67. Lewins, J. 1978. Reactor noise theory as a Markov process. *Atomkernenergie* 31(4):223-229.
68. Lu, J. T., R. A. Danofsky, and R. Struss. 1975. Diagnostics of void fluctuations in a reactor coolant channel using neutron noise techniques. Pages 21-1-21-28 in T. W. Kerlin, ed. *Proceedings of the Second Power plant dynamics, Control and Testing Symposium*. University of Tennessee, Knoxville, Tenn.
69. Matsubara, K. 1977. Experimental studies of core flow fluctuations and neutron noise in a BWR. *Progress Nucl. Energy* 1:137-149.
70. Matsubara, K., and R. Oguma. 1978. Experimental studies of core flow fluctuations as noise source in BWR. *J. Nucl. Sci. Technol.* 15(4):249-262.
71. Matthey, M. 1977. Description of void effects in a large BWR by means of a stochastic theory and simulation in a zero-power reactor. *Progress Nucl. Energy* 1:151-162.
72. Matthey, M. 1979. Quantization of stochastic variables: Description and effects on the input noise sources in a BWR. *Ann. Nucl. Energy* 6:345-353.
73. Miyazaki, K. A. 1978. Temperature fluctuation of sodium in annular flow channel heated by single-pin with blockage. *J. Nucl. Sci. Technol.* 15(1):10-23.
74. Mogil'ner, A. I. 1971. Noise associated with inhomogeneities in the heat carrier of a reactor. *Soviet Atomic Energy* 30:629-634.
75. Morishima, N. 1973. Theory of stochastic fluctuations in a power reactor. *J. Nucl. Sci. Technol.* 10:29-44.

76. Morishima, N. 1979. High-frequency structure of space-dependent neutron fluctuation spectra in a coupled-core reactor. *Ann. Nucl. Energy* 6:553-559.
77. Nabavian, M. 1977. Interpretation of neutron noise spectra measured in the presence of fluctuating voids. Unpublished Ph.D. thesis. Ames, Iowa, Library, Iowa State University, 1977.
78. Nomura, T. 1968. Noise analysis of boiling water reactor. Pages 197-210 in *Proceedings of Japan-United States Seminar on Nuclear Reactor Noise Analysis*, Tokyo and Kyoto, Japan.
79. Nowark, N. J. 1957. *Reactor Physics of UTR-10*, ASAE-19.
80. Operating and maintenance manual for solid state variable tuning filter. Krohn-Hite Corp., Cambridge, Mass. 1970.
81. Operating manual for UTR-10 reactor. ATL-1361. Advanced Technology Laboratories, Mountain View, California. 1959.
82. Otnes, R. K., and L. Enochson. 1972. *Digital time Series analysis*. 1st ed. John Wiley and Sons, Inc., New York, N.Y. 347 pp.
83. Pacilio, V. M., M. Vincenzo, J. F. Narelli, and R. Mosiello. 1976. Toward a unified theory of reactor noise analysis techniques. *Ann. Nucl. Energy* 3:239-251.
84. Pazsit, I. Two-group theory of noise in reflected reactors with application to vibrating absorbers. *Ann. Nucl. Energy* 5:185-196.
85. Rajagopal, V. 1963. Reactor noise measurements on Saxton reactor. Pages 427-448 in *Proceedings of AEC Symposium on Noise Analysis in Nuclear Systems*, Gainesville, Fla.
86. Rehsenow, W. M., ed. 1964. *Developments in Heat Transfer*. 1st ed. The MIT Press, Cambridge, Mass.
87. Rothman, P. 1973. Neutron noise in boiling reactors. *Atomkernenergie* 21(2):113-118.
88. Saito, K. 1967. On the noise equivalent source in a zero power reactor. *Nucl. Sci. Engr.* 28:452-456.
89. Saito, K. 1969. Noise equivalent source in nuclear reactors. *Nucl. Sci. Engr.* 28:384-396.

90. Saito, L. 1969. Temperature noise in low-power reactors. Nucl. Sci. Engr. 37:316-321.
91. Saito, K. 1969. Input-noise source of at-power reactors with temperature feedback effect. Nucl. Sci. Engr. 37:380-396.
92. Saito, K. 1972. Analysis of temperature and power noise in operating nuclear reactors. Nucl. Sci. Engr. 48:467-474.
93. Saito, K. 1973. Analytical study of operating reactor noise on a single channel and single flow model-I,II. J. Nucl. Sci. Technol. 10:259-267, 348-352.
94. Saito, K. 1974. On the theory of power reactor noise-I, II,III. Ann. Nucl. Energy 1:31-48, 107-128, 209-221.
95. Saleh, M., R. Danofsky, R. A. Hendrickson, and R. G. Struss. 1978. Response of a neutron detector to local coolant void distributions. Trans. Am. Nucl. Soc. 30: 507-508.
96. Saleh, M. M. 1979. Two phase flow blockage identification using neutron noise (Experimental plan for the UTR-10 reactor). Nuclear Engineering Departmental Report. Iowa State University, Ames, Ia.
97. Saleh, M. M., R. A. Danofsky, and R. A. Hendrickson. 1980. Detector adjoint shape characteristics as related to steam velocity measurements inferred from two-detector noise measurements. To be published in Nucl. Sci. Engr.
98. Saxe, R. F. 1966. Detection of boiling in water-moderated nuclear reactors. Nucl. Safety 7(4):452-456.
99. Saxe, R. F. 1967. Survey of boiling detection methods in reactors. Pages 41-57 in Proceedings of Conference on Incipient Failure Diagnosis for Assuring Safety and Availability of Nuclear Power Plants, Gatlinburg, Tenn.
100. Saxe, R. F. 1976. Transform and filtration methods in fluctuation analysis. Ann. Nucl. Energy 3:471-475.
101. Saxe, R. F., C. W. Mayo, and T. Saxe. 1976. Dynamic analysis of a pressurized water reactor. Ann. Nucl. Energy 3:477-488.
102. Schwalm, V. D. 1971. Identification of multiple-input multiple output linear systems by correlation methods. Int. J. Control 13(6):1131-1135.

103. Schwalm, V. D. 1972. Some remarks on failure detection in nuclear power reactors by noise measurements. Atomkernenergie 19:263-270.
104. Seifritz, W. 1970. At power reactor noise induced by fluctuation in the coolant flow. Atomkernenergie 16: 29-34.
105. Seifritz, W. 1972. An Analysis of the space dependent neutron flux density fluctuations at the Lingen boiling water reactor (KWL) by methods of stochastic processes. Atomkernenergie 19(4):271-279.
106. Seifritz, W., and F. Cioli. 1973. On-load monitoring of local steam velocity in BWR cores by neutron noise analysis. Am. Nucl. Soc., Trans. 17:451-453.
107. Sha, W. T. 1971. A generalized local boiling void model for light water reactor system. Nucl. Sci. Engr. 44:291-300.
108. Sheff, J. R., and R. W. Albrecht. 1966. The space dependence of reactor noise-I,II. Nucl. Sci. Engr. 24:246-259, 26:207-221.
109. Sheff, J. R. 1968. Neutron fluctuations at full power. Pages 113-121 in Proceedings of the Japan-United States Seminar on Nuclear Reactor Noise Analysis, Tokyo and Kyoto, Japan.
110. Singh, O. P., and D. Stegemann. 1978. Theoretical treatment of noise analysis in boiling water reactors. Atomkernenergie 31:74-82.
111. Stegemann, D., P. Chebureck, A. T. Mikulski, and W. Seifritz. 1973. Operating characteristics of a boiling water reactor deduced from in-core measurements. Pages 15-1-15-17 in T. W. Kerlin, ed. Power Plant Dynamics, Control and Testing Symposium. University of Tennessee, Knoxville, Tenn.
112. Techy, Z., and L. Szabados. 1974. A theoretical basis of bubble motion in reactor channels. Atomkernenergie 23:225-230.
113. Thie, J. A. 1959. Dynamic behavior of boiling reactors. ISAEC Report ANL-5849. (Argonne National Laboratory, Lemont, Ill.)

114. Thie, J. A. 1968. Noise in power reactor - a review of experiment, analysis, and theory. *Reactor and Fuel Processing Technology* 11(4):167-171.
115. Thie, J. A. 1975. Instrumentation integrity and response time testing utilizing system noise. Pages 10-1 10-18 in T. W. Kerlin ed. *Proceedings of the Second Power Plant Dynamics, Control and Testing Symposium*, University of Tennessee, Knoxville, Tenn.
116. Uhrig, R. E. 1970. Random noise techniques in nuclear reactor systems. *Ronald Press Co.*, New York.
117. Uhrig, R. E. 1973. State of the art of noise analysis in power reactors. CONF-730304 (ANS National Topical Meeting on Water Reactor Safety, Salt Lake City, Utah). 24 pp.
118. Uitert, G. C., and H. V. Dam. 1977. Analysis of pool-type reactor noise. *Progress in Nucl. Energy*. 1:649-662.
119. Utsuro, M., and T. Shibata. 1967. Power noise spectra of water reactor in low frequency region. *J. Nucl. Sci. Tech.* 4(6):267-272.
120. Wach, D., and G. Kosaly. 1974. Investigation of the joint effect of local and global driving sources in in-core neutron noise measurements. *Atomkernenergie* 23(4): 244-250.
121. Wallis, G. B. 1969. One dimensional two phase flow. 1st ed. *McGraw-Hill Book Company*, New York.
122. Williams, M. M. R. 1974. Random processes in nuclear reactors. 1st ed. *Pergamon Press*, Oxford.
123. Williams, C. L., and A. C. Peterson, Jr. 1978. Two-phase flow patterns with high-pressure water in a heated four-rod bundles. *Nucl. Sci. Engr.* 68:155-169.

#### X. ACKNOWLEDGMENTS

The author is indebted to his major professors, Dr. R. A. Danofsky and R. A. Hendrickson for their helpful discussions, suggestions, insight and encouragement during the various phases of this research. In addition, the author wishes to express his special appreciation to Dr. D. M. Roberts for reviewing the safety analysis of the experiment; to the reactor staff of the ISU UTR-10 reactor for assistance in reactor operation, to the ERI machine shop staff for building the experimental loop and finally to my wife Malahat for her patience and understanding through the years of study.

Funds for the equipment were provided by an educational and research grant from the Iraqi Ministry of Higher Education (IMHE) which was awarded to the author.

XI. APPENDIX A: COMPUTATION OF THE SPECTRA  
VIA FFT CALCULATIONS

As explained in Chapter IV, the time series data were processed through a 32k-MSI micro-computer. This memory size limited the number of time samples,  $N$ , from either channel to 256 words. As outlined in Chapter IV, the anti-aliasing filters were set at 12.5 Hz, and the associated sampling rate,  $f_s$ , was set at 30 samples per second, which defines the Nyquist frequency at 15 Hz. The above data indicates that the length of each time record,  $T$ , in either channel is 8.5333 seconds. According to Bendat and Piersol [12] and Otnes and Enochson [82], the discrete spectral points are separated by a resolution bandwidth given by

$$B_e = \frac{1}{T} = 0.11719 \text{ Hz} . \quad (\text{A-1})$$

A. The Algorithm For Calculating the APSD's of Two Channels and Their Associated CPSD

The mean value of each data record was calculated and subtracted from the data to obtain a time series with zero mean. An option for applying a window function to the data, in order to reduce the amplitude of side bands in the calculated spectra, is available. A cosine squared window was chosen and is given by [12]

$$\omega(t) = \cos^2(\pi t/T) . \quad (\text{A-2})$$

This window is applied to the first and last ten percent of the data record as suggested by Bendat and Piersol [12].

In this case, only the first and last three points of the time record were tapered by the window. The window option was applied to several white noise data records, the result revealed that this type of window enhanced the part of the spectrum below 0.2 Hz. Accordingly, it was decided not to use this option in all the subsequent experimental analyses.

The Fourier transform of the two real-valued records is computed simultaneously by inserting one record  $x(n)$  as the real part and one record  $y(n)$  as the imaginary part of a complex record  $z(n)$ , thus

$$z(n) = x(n) + j y(n) , \quad (A-3)$$

$$n = 1, 2, \dots, N.$$

The Fourier transform of  $z(n)$  is computed through the FFT to give the transforms

$$Z(k) \text{ for } k = 0, 1, 2, \dots, N-1 .$$

The two real-valued records  $S(n)$  and  $Y(n)$  have Fourier transforms  $x(n)$  and  $y(n)$  respectively given by

$$X(k) = [Z(k) + Z^*(N-k)]/2 , \quad (A-4)$$

and

$$Y(k) = [Z(k) - Z^*(N-k)]/2 , \quad (A-5)$$

where the Nyquist frequency occurs when  $k = \frac{N}{2}$ , so that unique results occur only for  $k = 0, 1, 2, \dots, \frac{N}{2}$ .

The raw APSD estimates are given by

$$R_x(k) = |X(k)|^2 , \quad (A-6)$$

and

$$R_y(k) = |Y(k)|^2 . \quad (A-7)$$

The raw CPSD estimate is given by

$$R_{xy}(k) = X^*(k)Y(k) = S(k) - j T(k) . \quad (A-8)$$

The transforms  $X(k)$ ,  $Y(k)$  and  $Z(k)$  can be expressed in terms of their real and imaginary parts as:

$$\begin{aligned} X(k) &= A(k) + j B(k) , \\ Y(k) &= C(k) + j D(k) , \\ Z(k) &= E(k) + j F(k) . \end{aligned} \quad (A-9)$$

Substituting Equations (A-9) into Equations (A-4) and (A-5) and equating the real and imaginary parts, give

$$\begin{aligned} A(k) &= [E(k) + E(N-k)]/2 , \\ B(k) &= [F(k) - F(N-k)]/2 , \\ C(k) &= [F(k) + F(N-k)]/2 , \\ D(k) &= [E(N-k) - E(k)]/2 . \end{aligned} \quad (A-10)$$

Substituting the above equations into Equations (A-6) through (A-8), give the following raw estimates

$$\begin{aligned}
 R_x(k) &= A^2(k) + B^2(k) , \\
 R_y(k) &= C^2(k) + D^2(k) , \\
 S(k) &= A(k)C(k) + B(k)D(k) , \\
 T(k) &= B(k)C(k) - A(k)D(k) .
 \end{aligned} \tag{A-11}$$

The above raw estimates are governed by a  $\chi^2$  distribution with two degrees of freedom [12].

To reduce statistical errors, the results from  $q$  separate time records of length  $T$  are averaged. The time segment averaged spectra are then given by

$$\hat{R}(k) = \frac{1}{q} [R_1(k) + R_2(k) + \dots + R_q(k)] , \tag{A-12}$$

where  $\hat{R}$  refers to  $R_x$ ,  $R_y$ , or  $R_{xy}$ .

The quantity  $R$  is a  $\chi^2$  variable with  $2q$  degrees of freedom, and normalized standard error of

$$\varepsilon = \sqrt{1/q} . \tag{A-13}$$

Since all the experimental analyses were carried out for  $q = 36$ , the normalized standard errors for the computed spectra were 16.67%.

Finally, the spectra are normalized by using the following normalization factors

$$\begin{aligned}
 N_x &= F \frac{1}{AF^2} \frac{1}{DC_x^2} \frac{1}{G_x^2} T , \\
 N_y &= F \frac{1}{AF^2} \frac{1}{DC_y^2} \frac{1}{G_y^2} T , \\
 N_{xy} &= F \frac{1}{AF^2} \frac{1}{DC_x} \frac{1}{DC_y} \frac{1}{G_x G_y} T ,
 \end{aligned} \tag{A-14}$$

where

$F = 1$  for no window

$F = 2$  for cosine squared window

$T = \text{transformation factor} = \frac{2h}{N}$

and  $AF$  is the analog to digital converter conversion factor,  
 $DC_x$  and  $DC_y$  are the DC voltages of the signals  $x$  and  $y$ ,  $G_x$   
and  $G_y$  are the amplification gains of signals  $x$  and  $y$ .

The normalized spectra are given by

$$R_{\text{norm}}^i(k) = N_i \hat{R}_i(k) , \tag{A-15}$$

for  $i = x, y$  or  $xy$  .

The phase of the CPSD is found from the relation

$$\text{PHASE}(k) = \frac{180}{\pi} \tan^{-1} [T(k)/S(k)] . \tag{A-16}$$

The correct quadrant is determined from the signs of  $T$  and  $S$ .

The input-output transfer function is found from the  
relation

$$TRFN(k) = \frac{R_{xy}(k)}{R_x(k)} \tag{A-17}$$

The coherence function is found from the relation

$$\text{COH}(k) = \frac{R_{xy}(k)}{R_x(k)R_y(k)} . \quad (\text{A-18})$$

#### B. Program Listing

A flow chart diagram of this program was given in Chapter IV (Figure 4.7). Given below is a complete listing of the program that was used in the calculation of the spectra.

```
DIM A(512),S(130),8(130),C(130),R8(130),I8(130)

DIM 89,I,I1,I2,I3,I4,I5,J,A8,C8,B6,C6,I6,R6,M,B8,D8,D,R,
     D1,D4

DIM D9,D2,D3,S1,L,K,K2,K3,A1,A2,A4,A4,A5,A6,A$(1),N,N1,
     N2,N7,N8

DIM N9,N$(1),X,Y,Y1,Y2,Y9,Y$(1),V,C1,C3,O,G1,G2,P1,P2,P3
     L9,R9

DIM E1,E2,F,F2,F3,F6,F$(1),H8,T8,B5

DIM TDEL,DEL,Z5,Z6,Z7,V5,V6,T9

DIM C5,FILNAMES(8),FILIDS(72)

DIM M1,K1,Q1,Q2,FMT$(62)

FMT$="#.# #.###.## #.###.## #.###.## #.###.## -#.# #.###.## #.###.##

Z6=PINT9=0

PRINT"ENTER TOTAL DELAY,DELAY" INPUT\TDEL,DEL
ON ERROR GOTO 114

14 INPUT"ENTER,IN PERCENT,THE TAPER LENGTH ON EACH SIDE"Z5
Z5=Z5/100

A6=180/PI\N9=1\Y=0 PRINT "DO YOU WANT TO OUTPUT PRE/. RUN"
INPUT Y$\IF Y$="Y" THEN 1320

INPUT"DO YOU WANT TO ADD MORE AVE TO PREVIOUS RUN"Y$
IF Y$="Y" THEN 119

FOR I=0 TO 127\B(I)=0\C(I)=0\R8(I)=0\I8(I)=0\NEXT I
119 GOSUB 700

1111 GOSUB 1000
```

```

IF Y=1 THEN GOSUB 820\Y=0\GOTO 1111

GOSUB 900

20 IF Z5<>0 THEN GOSUB 1200

GOSUB 100\IF N9-C3=0 THEN 64

N9=N9+1\PRINT"PASS #";N9-1\GOSUB 820\GOTO 20

36 FOR K=1 TO N/4\I=N1-K\M=K+K\U=L+L\A8=A(M)+A(J)

B8=A(M)-A(J)\C8=A(M+1)+A(J+L)\D8+A(M+1)-A(J+1)

B6=A8*A8+D8*D8\B(K)=B(K)+B6\C6=C8*C8+B8*B8\C(K)=C(K)+C6

I6=-A8*B8-D8*C8\R6=A8*C8-B8*D8

R8(K)=R8(K)+R6\I8(K)=I8(K)+I6\NEXT K\RETURN

64 GOSUB 1300\PRINT"DO YOU WANT TO CONTINUEE Y OR N"

INPUT A$\IF A$="Y" THEN 14

STOP

100 V=0\N1=N/2\N2=N/4+2\L=N2+1\D=0\R=PI/N1\IF N9<>1 THEN

131

S(1)=0\DI=1\S(N2-1)=1\DI=SIN(R)\S(2)=DI\DI=COS(R)

FOR I=3TON/8+1\R=DI*D2\DI=R-D\S(L-I)=DI\DI=R+DI

S(I)=DI*D2\NEXT I

131 IF V=2 THEN 220

IF V=3 THEN 149

A5=1/N1\FOR I=1 TO N\A(I-1)=A(I-1)*A5\NEXT I

149 J=1\FOR I=1 TO N STEP 2

IF J>1 THEN GOSUB 300

K=N1

160 IF J>K THEN GOSUB 400

```

```

IF J>K THEN 160

J=J+K\NEXT I\I3=2\I=2\I1=N1

170 I4=I+I\I2=1\FOR J=1 TO I STEP 2\S1=-S(I2)\IFV=3 THEN

    S1=-S1

C1=S(N2-I2)\IF J =I3 THEN GOSUB 500

IF J<I3 THEN I2=I2+I1

FOR K=J TO N STEP I4\L=K+I\A1=C1*A(L-1)-S1*A(L)

A2=C1*A(L)+S1*A(L-1)\A(L-1)=A(K-1)-A1\A(L)=A(K)-A2

A(K-1)=A(K-1)+A1\A(K)=A(K)+A2\NEXT K\NEXT J\I3=I+1\I=I4

I1=I1/2\IF I<=N1 THEN 170

IF V=1 THEN 290

IF V=3 THEN 290

REM THE REAL SUB. IS NOT TRANS.

220 PRINT "INVERSE IS NOT COMPUTED"

290 GOSUB 36\RETURN

300 A1=A(J-1)\A2=A(J)\A(J-1)=A(I-1)\A(J)=A(I)

A(I-1)=A1\A(I)=A2\RETURN

400 J=J-K\K=K/2\RETURN

500 I2=I2-I1\C1=-C1\RETURN

600 A(1)=A5+A(N+1\A(2)+A5-A(N+1)\=3\GOTO 149\RETURN

7000=I\INPUT"# OF DATA POINTS/CHAN. "N\N=N*2

PRINT "SAMPLING RATE/SEC"\INPUT Y9\PRINT "# OF SAMPLES TO

BE A/E. "

INPUT CB\PRINT"ENTER D.C CH. A"\INPUT Y1\PRINT Y1

T9=T9+C3

```

```

PRINT"ENTER D.C CH. B"\INPUT Y2\PRINT Y2
PRINT"ENTER GAIN CH.A"\INPUT G1\PRINT G1
PRINT"ENTER GAIN CH. B"\INPUT G2\PRINT G2
C1=N*Y9*256\C1=100/C1\P1=Y1*Y1*G1*G1-P1=C1/P1
P2=Y2*G2\P2=P2*P2\P2=C1/P2\P3=Y1*Y2*G1*G2\P3=C1/P3
P1=P1/.875\P2=P2/.875\P3=P3/.875
D9=INT(1000000/Y9)D9=D9-TDEL\D9=D9/DEL
L9=INT(D9/255)\R9=INT(D9-L9*256)
REM PUT SAMPLING DELAY AT LOC. F01C
POKE :F01C,L9\POKE :F01D,R9
REM PUT # OF POINTS/SAMPLE AT F012
L9=INT(N/256)\R9=INT(N-L9*256)\POKE :F012,L9\POKE :F013,R9
REM SET START ADDR. OF DATA TO :6200,PUT IN LOC. F01E
POKE :F01E,:62\POKE :F01F,0
820 REM START DATA CONVERSION & STORAGE
CALL DCOLEC
REM TRANSFER DATA TO MATRIX A
B9=:6200\FOR I=0 TO N-1\A(I)=PEEK(B9+I)
NEXT I\RETURN
REM EXTRACT D.C FROM SIGNAL
Y=0\x=0\FOR I=0 TO N-1 STEP 2\x=X+A(I)\Y=Y+A(I+1)\NEXT I
N1=N/2\Y=Y/N1\x=X/N1\FOR I=0 TO N-1 STEP 2\A(I)=A(I)-X
A(I+1)=A(I+1)-Y\NEXT I\RETURN
1000 E1=0\E2=0\FOR I=0 TO N-1 STEP 2\IF A(I)=0 THEN E1+E1+1
IF(A(I)-256=0 THEN E1=E1+1
IF(A(I+1)-256)=0 THEN E2=E2+1

```

```

IF A(I+1)=0 THEN E2=E2+1

NEXT I\IF (E1+E2)=0 THEN RETURN

PRINT "# OF EXTREMA HIT IN CH.A=";E1

PRINT "# OF EXTREMA HIT IN CH. B=";E2

PRINT "RE-ENTER DATA Y OR N"\INPUT Y$\IF Y$="Y" THEN

Y=01\RETURN

REM APPLY COS SQR WINDOW TO RAW DATA

1200 K=INT(N1*Z5)\IF F<3 THEN K=3

D9=Z6/(4*K-4)\A(0)=0\A(1)=0\A(N-1)=0 A(N-2)=0 K2=2*K-4

K3=N-4 FOR I= 2 TO K2 STEP 2 X=SIN(D9*I) A(I)=A(I)*X

A(I+1)=A(I+1)*X A(K3)=A(K3)*X A(K3+1)=A(K3+1)*X

K3=K3-2\NEXT I\RETURN

1300 IF N9>1 THEN PRINT "PASS #";N9

1320 F6=Y9/N1\N$="Y"\PRINT "DO YOU WANT TO PRINT OUTPUT?"

INPUT A$\IF LEFT$(A$,1)<> N$ THEN 1500

PRINT "ENTER START FREQ."\INPUT F2\PRINT F2

PRINT "ENTER FINAL FREQ."\INPUT F3\PRINT F3

INPUT "ENTER THE # OF FREQ. AVE." Z7\R=(Z7-1)*F6*.5

111 PRINT "      "

PRINT "FREQ. ";TAB(8); "PSD";TAB(17); "PSD";TAB(26); "CPSD";

TAB(35):

PRINT "PHASE";TAB(43); "TRANSF";TAB(52); "COHERN"

PRINT TAB(8); "CH A";TAB(17); "CH B";TAB(35); "DEGR"

IF Q1=P1 THEN RETURN

I1=INT(F2/F6)\I2+INT(F3/F6)\IF I2>N/4 THEN I2=N/4

```

```

I5=0\I6=0\F=0\B5=0\B5=0\C5=0\H8=0\T8=0\N8=0\IF I1=0
THEN I1=1
F=F6*(I1-1)\V5=0\V6=0
N7=.25/T9\FOR Q1=T1 TO I2\I=Q1
V5=V5+8(I)\V6=V6+C(I)
GOSUB 1400\GOTO 1120
1400 X+I8(I)*I8(I)+R8(I)*R8(I)
H8=H8+X/(B(I)*C(I))\X=SQR(X)
I5=I5+X\T8=T8+X/B(I)
Y=90\IF R8(I)<>0 THEN Y=A6*ATN(I8(I)/R8(I))\Y=ABS(Y)
IF I8(I)>=0 THEN IF R8(I) >0 THEN N8=N8+Y-360
IF I8(I) >=0 THEN IF R8(I) <0 THEN N8=N8-Y-180
IF I8(I) <0 THEN IF R8(I) <0 THEN N8=N8+Y-180
IF I8(I) <0 THEN IF R8(I) >0 THEN N8=N8-Y
B5=B5+B(I)\C5=C5+C(I)
RETURN
1120 F=F+F6\I6=I6+1\IF I6<Z7 THEN NEXT Q1
IF I6<Z7 THEN 1321
Y=1/Z7\B5=B5*P1*N7\C5=C5*P2*N7\I5=I5(P3*N7
T8=T8*Y\H8=H8*Y\N8=N8*Y
PRINT USING FMT$,F-R,B5,C5,I5,N8,T8,H8
I6=0\B5=0\C5=0\I5=0\T8=0\H8=0\N8=0\NEXT Q1\GOTO 1321
V5=V5*P1*N7\V6=V6*P2*N7
1321 PRINT"VARIANCE A= ";V5*F6;" VARIANCE B = ";V6*F6\
GOTO 1320

```

```
1500 INPUT"DATA SAVED?"Y$\IF Y$<>"Y" THEN RETURN
PRINT"ENTER FILE NAME:UP TO 8 CHAR."\"INPUT FILNAME$\PRINT
FILNAME$

INPUT "ENTER FILE I.D:UP TO 72 CHAR."FILID$\PRINT FILID$
FILNAME$=LEFT$(FILNAME$,LEN(FILNAME$))

CREATE #01,FILNAME$

PRINT #01,FILID$

F=0\FOR Q1=0 TO N/4-1\I=Q1\GOSUB 1400
WRITE #01,F,B5,C5,I5,N8,T8,H8
F=F+F6\NEXT Q1\CLOSE #01\PRINT"DO YOU WANT TO READ BACK
FROM DISK"

INPUT Y$\IF Y$<>"Y" THEN RETURN
INPUT"ENTER FILE NAME" FILNAME$\PRINT FILNAME$
FILNAME$=LEFT$(FILNAME$,LEN(FILNAME$))

OPEN #01,FILNAME$

INPUT#01,FILID$\PRINT FILID$
Q1=PI\GOSUB 111\Q1=0\FOR I=0 TO N/4-1\READ#01,F,A1,A2,
Q1,A3,Q2,A4\
PRINT USING FMT$,F,A1,A2,Q1,A3,Q2,A4
NEXT I CLOSE #01
RETURN
114 PRINT"ERROR #=";ERR GOTO 14
END
```

\*The following machine code, initiates the ADC, samples the two input streams and stores the digitized data in memory

```
SRATE EQU $F01C
SDATA EQU $F01E
NDATA EQU $F012
DCOLEC LDX NDATA
STX NPTS
LDX SDATA
STX TSTART
START LDX SRATE
DELAY DEX
BNE DELAY
LDX #$C000
LDA A 0,X
NOP
NOP
LDA A 0,X
COM A
LDX #$C001
LDA B 0,X
NOP
NOP
LOA B 0,X
COM B
NOP
```

LDX SDATA  
STA A 0,X  
STA B 1,X  
INX  
INX  
STX SDATA  
LDX NDATA  
DEX  
DEX  
STX NDATA  
BNE START  
LDX NPTS  
STX NDATA  
LDX TSTART  
STX SDATA  
RTS  
TSTART RMB 2  
NPTS RMB 2  
END  
READY

## XII. APPENDIX B: EVALUATION OF THE ADJOINT RESPONSE USING THE CRAM CODE

### A. Two-Dimensional Modeling of the UTR-10

According to Equation (3-139), the evaluation of the APSD and CPSD involves the use of the frequency and spatially dependent adjoint response. The adjoint state equations for two-dimensional geometry in a two-group reactor system were derived as Equation (3-118). Since the various amplitudes are complex, while the usual procedure for solving such equations is designed for real quantities, the above formulation was transformed into a form more suitable for practical computations. This form, given as Equation (3-126) represents an inhomogeneous set due to the presence of the thermal adjoint source  $\Sigma_d$ . As explained in detail elsewhere (Section C of Chapter III), the adjoint source term was conveniently introduced as a scattering term from a fictitious energy group. This improvisation was necessary since the available diffusion code, CRAM, does not explicitly handle an external source. Introducing the fictitious energy group resulted in Equation (3-132). The original two-dimensional inhomogeneous adjoint equations in phase space  $(\vec{r}, \omega)$  were transformed into a set of homogeneous differential equations in five groups which could then be numerically solved, through the use of the CRAM code, for the UTR-10 reactor. A brief description of the UTR-10

reactor was given in Section A of Chapter IV. A schematic cross-sectional diagram for the UTR-10 in quarter symmetry is shown in Figure B.1. Four distinct regions, indicated as I, II, III and IV, were considered. The regions consist of graphite, water and air for region I, fuel and graphite for region II, water and graphite for region III and graphite only for region IV. The group constants for the different regions are presented in Tables B.1 through B.3 and were based on Huang data [54]. The group constants for each region were obtained, by averaging over the y direction, as follows [1, 11]

$$C_{i,k} = \sum_j v_j \bar{\phi}_{j,k} C_{i,k,j}, \quad (B-1)$$

where

$C_{i,k}$  = the average group constant for region i and energy k

$v_j$  = the volume fraction for material j

$\bar{\phi}_{j,k}$  = the average value of the normalized flux for material j in energy group k (a cosine flux shape was assumed for both energy groups)

$C_{i,k,j}$  = the group constant for material j in region i and energy group k.

The calculated two group macroscopic constants for different regions are summarized in Table B.4.

#### B. Checking the CRAM Code

To check the operation of the CRAM code and to provide data for the APSD and CPSD calculations, the two-dimensional

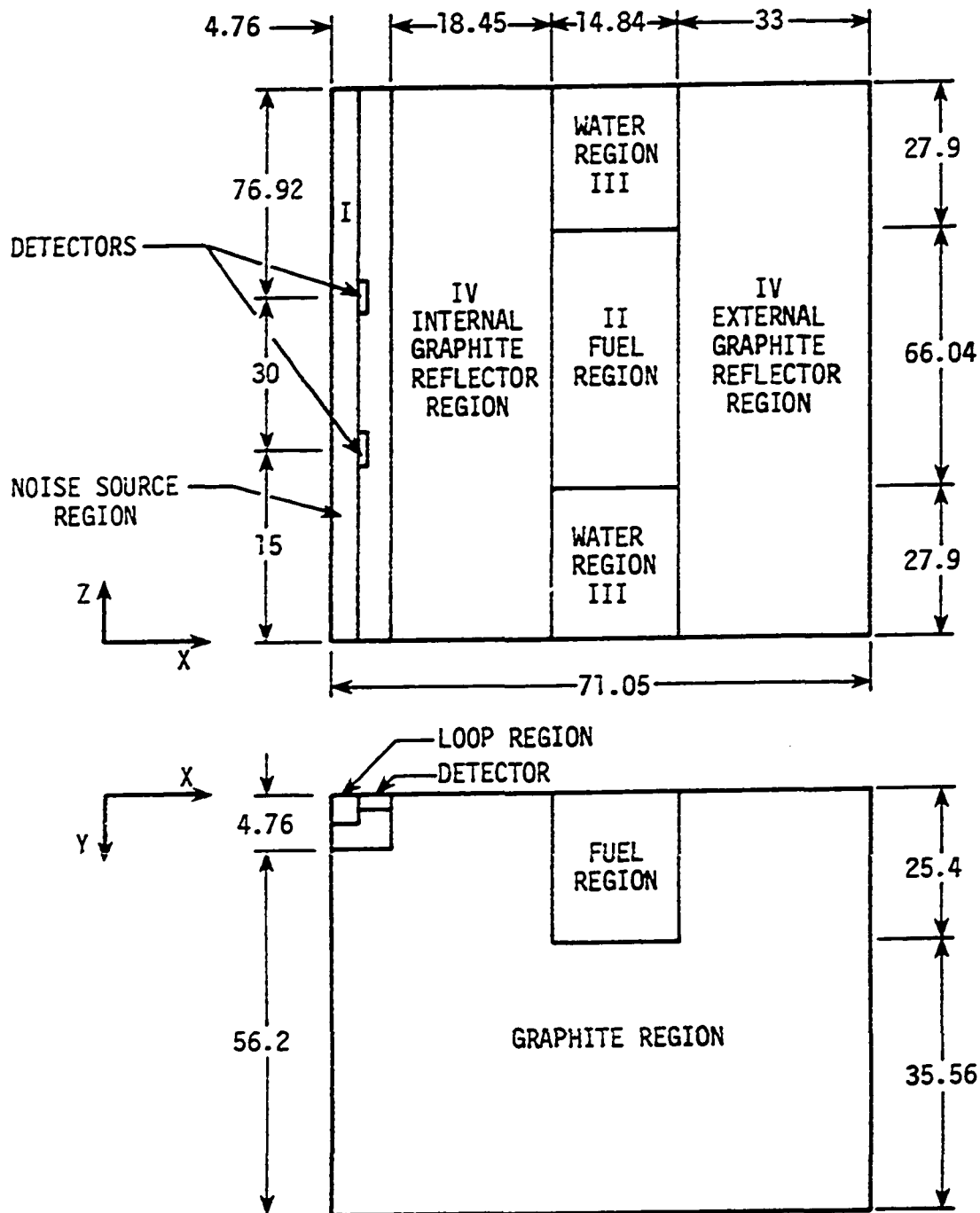


Figure B.1. Schematic cross-sectional diagram for the UTR-10 reactor (all units are in centimeters)

Table B.1. Macroscopic parameters for the fuel region of the UTR-10 at a coolant temperature of 32°C

Energy group	D	$(\Sigma_s)_{i \rightarrow i+1}$	$\Sigma_a$	$v\Sigma_f$
1st group	2.30947	0.0813495	0.0016907	0.00026532
2nd group	1.163952	0.1066567	0.00024492	0.0003347
3rd group	0.774892	0.1047691	0.0045654	0.00510796
Combined fast group	1.421447	0.341292	0.0019626	0.00186632
Thermal group	0.231576		.0524102	0.07640672

Table B.2. Macroscopic parameters for the graphite reflector region of the UTR-10

Energy group	D	$(\Sigma_s)_{i \rightarrow i+1}$	$\Sigma_a$	$v\Sigma_f$
1st group	2.2393188	0.2388177	0.63324E-7	0.0
2nd group	1.0509005	0.00103966	0.61602E-7	0.0
3rd group	0.9314399	0.0057416	0.88038E-7	0.0
Combined fast group	1.152864	0.0028736	0.53263E-7	0.0
Thermal group	0.991810		0.30661E-3	0.0

Table B.3. Macroscopic parameters for water at a temperature of 32°C

Energy group	D	$(\Sigma_s)_{i+i+1}$	$\Sigma_a$	$v\Sigma_f$
1st group	2.20644	0.10518	0.13949E-2	0.0
2nd group	1.09302	0.14949	0.12605E-4	0.0
3rd group	0.59154	0.15061	0.94565E-3	0.0
Combined fast group	1.32259	0.04837	0.797165E-3	0.0
Thermal group	0.15523		0.18785E-1	0.0

Table B.4. Two-group macroscopic parameters for the regions of the UTR-10

Region <sup>a</sup>	Energy group	D	$\Sigma_r$	$\Sigma_{1-2}$	$v\Sigma_f$
I	fast	1.16019	0.38159E-2	0.31697E-2	0.0
	thermal	0.98123	0.97201E-3	0.0	0.0
II	fast	1.32744	0.024465	0.0231897	0.121311E-2
	thermal	0.49766	0.034174	0.0	0.49664E-1
III	fast	1.26318	0.03296	0.032444	0.0
	thermal	0.44804	0.01232	0.0	0.0
IV	fast	1.15286	0.28737E-2	0.28736E-2	0.0
	thermal	0.99182	0.30661E-3	0.0	0.0

<sup>a</sup>Refer to Figure B.1.

reactor model presented in the previous section was used in a critical buckling search. In this search, a total of 506 mesh points (23 in the X direction and 22 in the Y direction) in two energy groups were used. The value of the buckling (in the Y direction) was obtained as ( $3.374 \times 10^{-4} \text{ cm}^{-2}$ ) which is reasonably close to the geometrical buckling of ( $6.6310 \times 10^{-4} \text{ cm}^{-2}$ ). The calculated steady state flux distribution for different axes across the UTR-10 reactor are shown in Figures B.2 through B.4. It is found from Figure B.2 that the flux shapes, for the fast and the thermal groups, are similar to those obtained by the one-dimensional results of Nowark [79] and three-dimensional results of Huang [54].

Prior to the two-dimensional adjoint calculations, a one-dimensional one group adjoint calculation was performed using the CRAM code. The results were compared to the exact results obtained from the Green's function solution [8, 15, 40, 50]. The results of the comparison are shown in Figures B.5 through B.6. These plots reveal an excellent agreement between the CRAM and the exact Green's function solutions that support the notion of using the CRAM code as a valid means to calculate the frequency response characteristics of a reactor.

### C. CRAM Results

The two group constants presented in Table B.4 were used to calculate the five group frequency dependent constants that

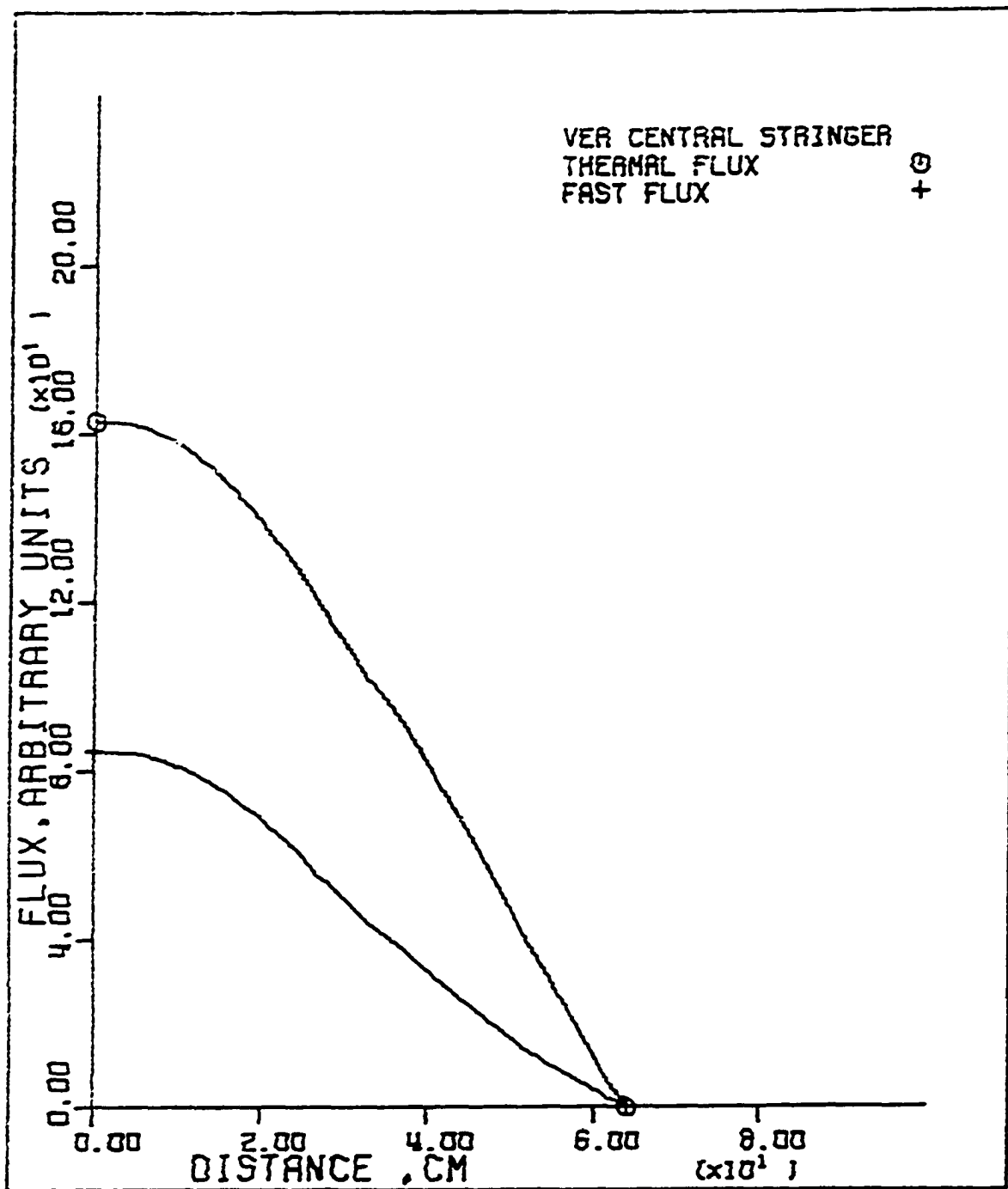


Figure B.2. Fast and thermal flux distribution along the z-axis crossing the internal graphite reflector region

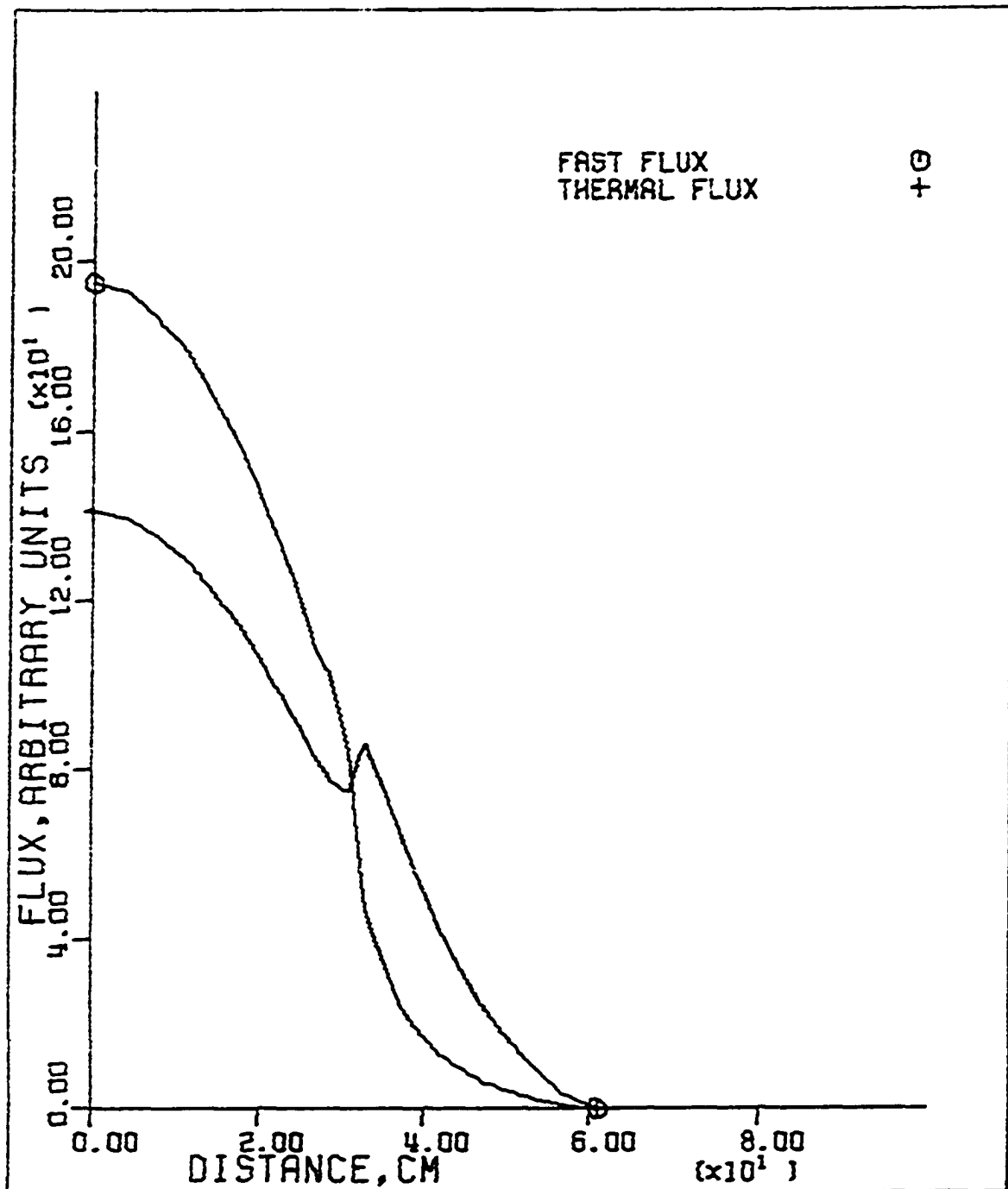


Figure B.3. Fast and thermal flux distribution along the Z-axis ( $X = 23.6$ ,  $y = 0$ ) crossing the fuel and water regions

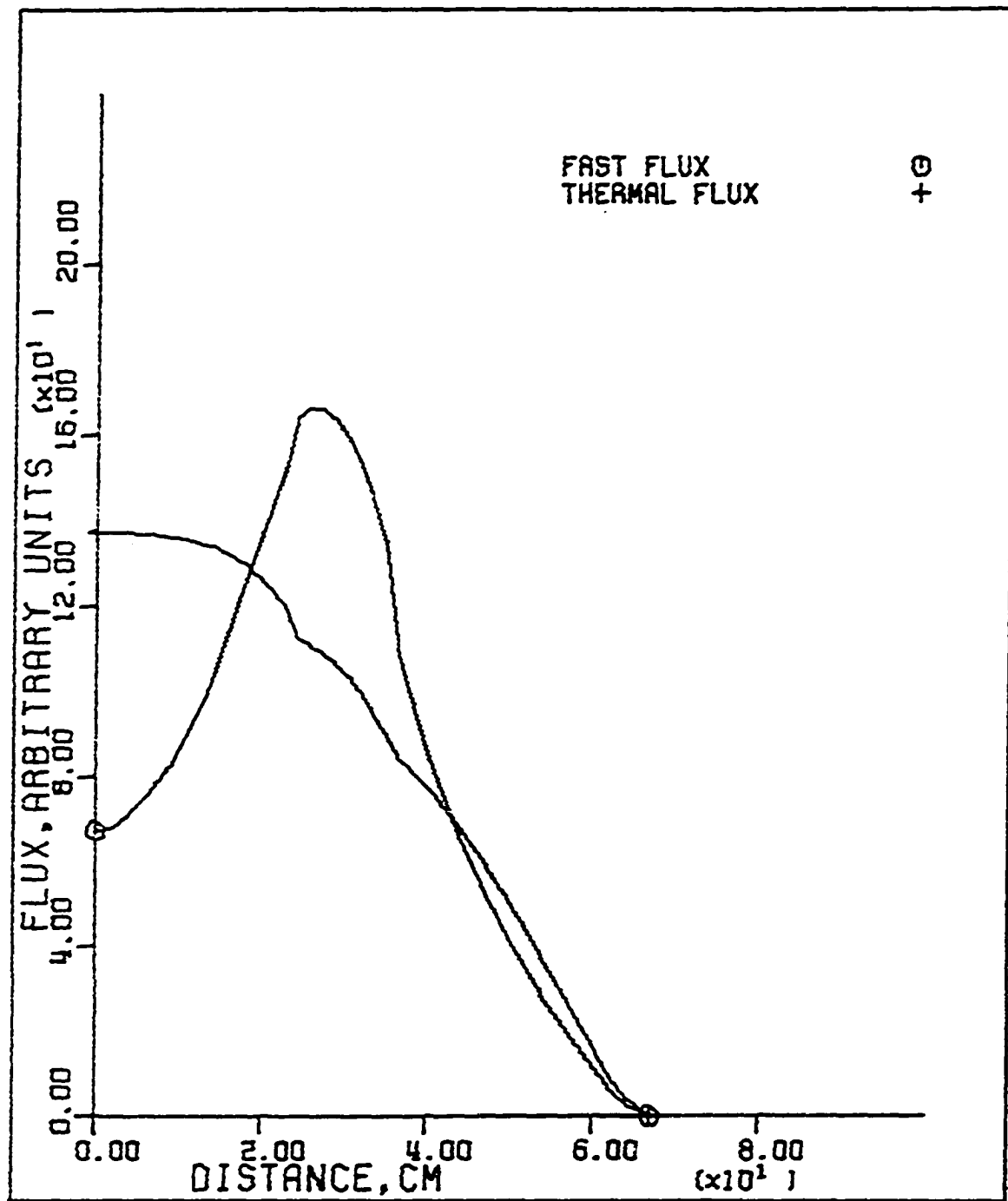


Figure B.4. Fast and thermal flux distribution along the x-axis ( $Z = 19.6$ ,  $y = 0$ ) crossing the internal graphite, fuel and graphite reflector regions

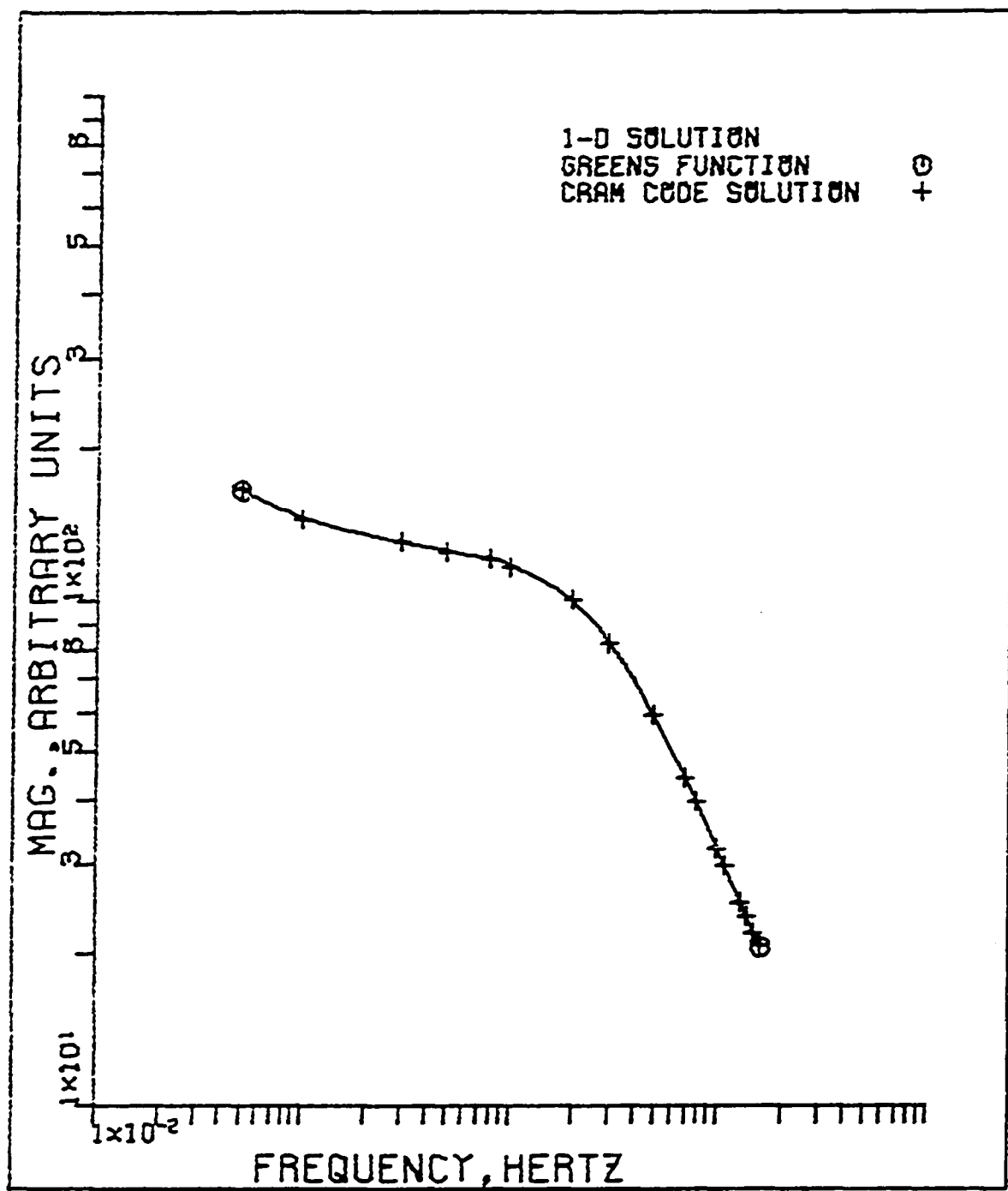


Figure B.5. A comparison between the adjoint response's magnitude for the 1-D CRAM solution and the exact Green's solution

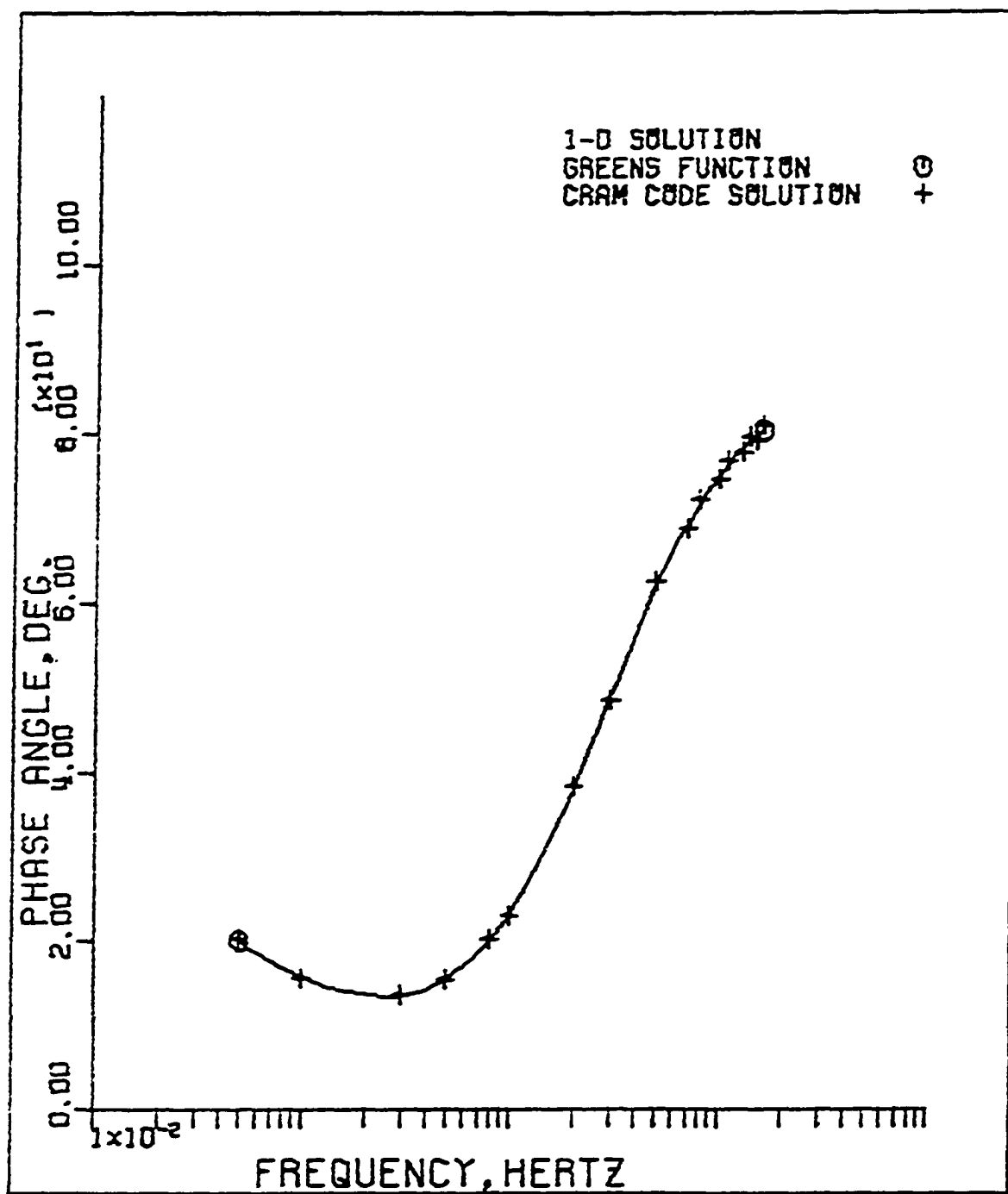


Figure B.6. A comparison between the adjoint response's phase for the 1-D CRAM solution and the exact Green's solution

were required for the two-dimensional two energy group adjoint response calculations. Five frequencies were selected for the calculations, namely at 0.4, 1, 2, 5 and 7 Hertz. The results for one and five Hertz are summarized in Table B.5 and B.6. The magnitude and phase of the adjoint response at position  $x = y = 0$  are shown in Figures B.7 and B.8. The shapes of the adjoint response (at one Hertz) show a peak at the detector positions while their phase shows a valley instead. The validity of these results are confirmed by the reactor response results of Pazsit [84] which are based on the exact one-dimensional two-energy groups solution. In this comparison, one should bear in mind the difference between the reactor adjoint-response (this work) and the reactor response (Pazsit work). According to Equation (3-136) the reactor response to an arbitrary input disturbance is equivalent to the complex conjugation of the corresponding adjoint response.

The magnitude and phase of the adjoint response, as a function of frequency, from a detector at position  $x = y = 0$  and  $z = 27$  cm are shown in Figures B.9 and B.10 for different source positions. The magnitude of the reactor adjoint-response, which has the same frequency behavior as the reactor response, rolls off at approximately seven Hertz as expected for the UTR-10 reactor [49, 82].

Table B.5. The thermal adjoint response (at  $x = y = 0$ ) for a detector at position  $Z = 15 \text{ cm}$

Frequency, Hz Distance along z direction, cm	1		5	
	Magnitude	Phase, deg.	Magnitude	Phase, deg.
2.064	252.62	29.71	187.96	51.90
4.128	252.05	29.63	187.54	51.75
6.192	251.02	29.55	186.77	51.41
8.256	249.68	29.34	185.83	50.89
10.320	248.42	28.89	184.84	50.03
12.384	248.04	28.07	184.60	48.77
14.448	250.51	26.65	186.44	46.89
16.512	234.76	28.12	172.84	48.75
18.576	231.68	28.97	163.41	50.11
20.640	219.36	29.73	154.97	51.03
22.704	207.39	30.45	146.51	51.67
24.768	196.07	31.21	138.53	52.24
26.832	185.37	31.60	130.95	52.67
28.896	175.25	31.83	123.81	53.19
30.960	165.68	31.97	117.05	53.52
33.024	156.64	32.09	110.47	53.80
37.681	135.53	32.22	95.79	54.09
42.338	117.26	32.43	77.32	54.46
46.995	101.46	32.58	62.41	54.75
51.652	70.37	32.71	48.38	54.99
56.309	48.80	32.83	28.24	55.17
60.966	16.08	32.87	9.31	55.25

Table B.6. The thermal adjoint response (at  $x = y = 0$ ) for a detector at position  $Z = 27$  cm

Frequency, Hz Distance along Z direction, cm	1		5	
	Magnitude	Phase, deg.	Magnitude	Phase, deg.
2.064	245.04	33.09	204.66	53.90
4.128	244.19	32.95	203.96	53.61
6.192	242.49	32.83	202.53	53.45
8.256	239.91	32.67	200.37	53.17
10.320	336.61	32.38	197.62	52.71
12.384	232.90	32.19	194.52	52.15
14.448	228.19	31.87	190.59	51.55
16.512	222.88	31.35	186.15	50.71
18.576	217.79	30.71	181.90	49.82
20.640	215.59	30.03	177.55	48.85
22.704	207.89	29.07	173.63	47.91
24.768	205.02	28.10	171.61	46.77
26.832	206.50	26.63	172.47	46.83
28.896	184.76	78.15	154.31	48.81
30.960	167.67	29.01	140.04	49.89
33.024	152.51	29.63	127.38	50.67
37.681	129.87	30.08	108.47	51.28
42.338	101.76	30.52	84.99	51.80
46.995	76.16	30.89	63.61	52.45
51.652	52.59	31.75	43.92	52.99
56.309	30.84	31.60	25.76	53.57
60.966	10.16	31.93	8.48	54.12

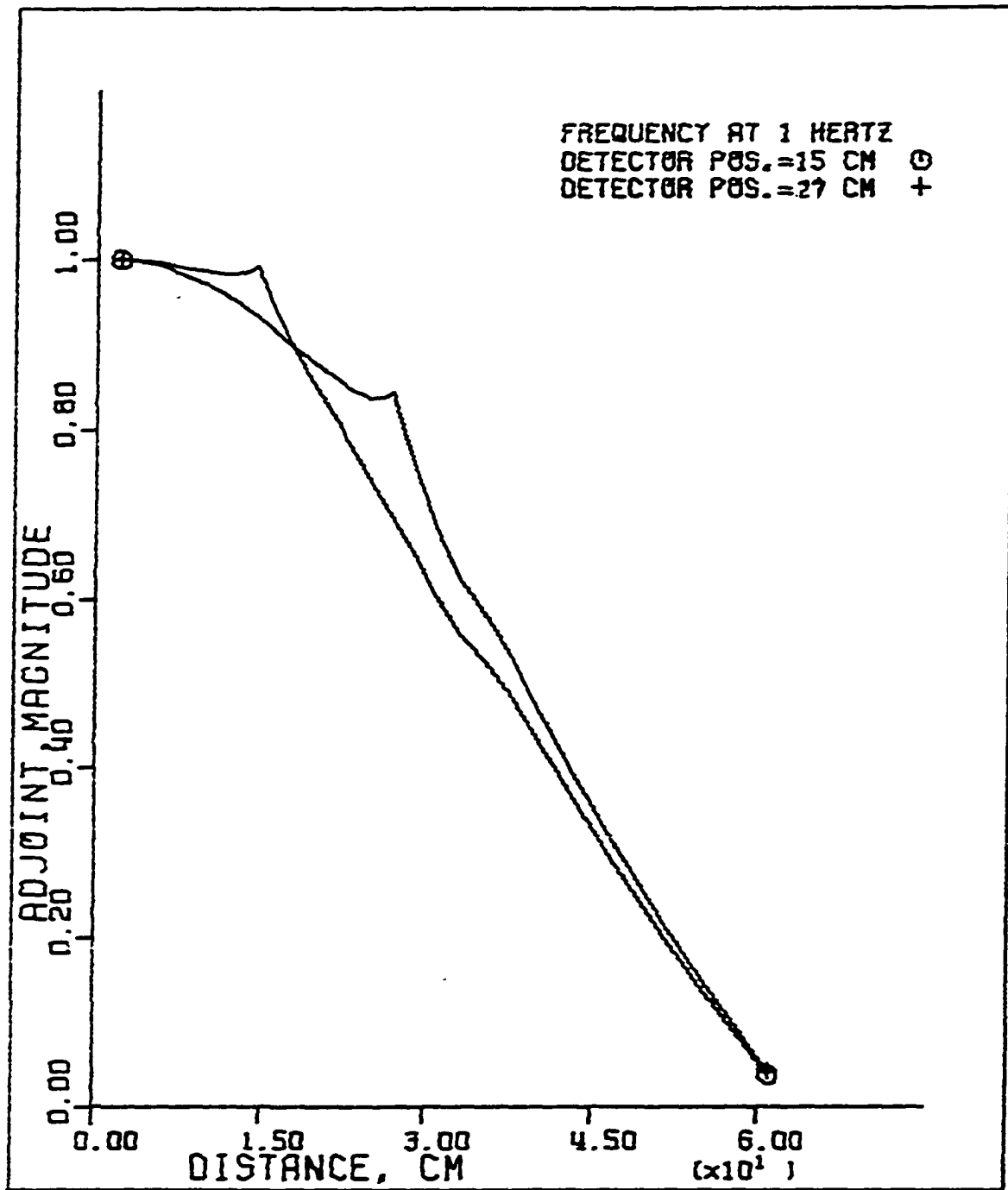


Figure B.7. The magnitude of the thermal adjoint functions along the Z-axis ( $x = y = 0$ )

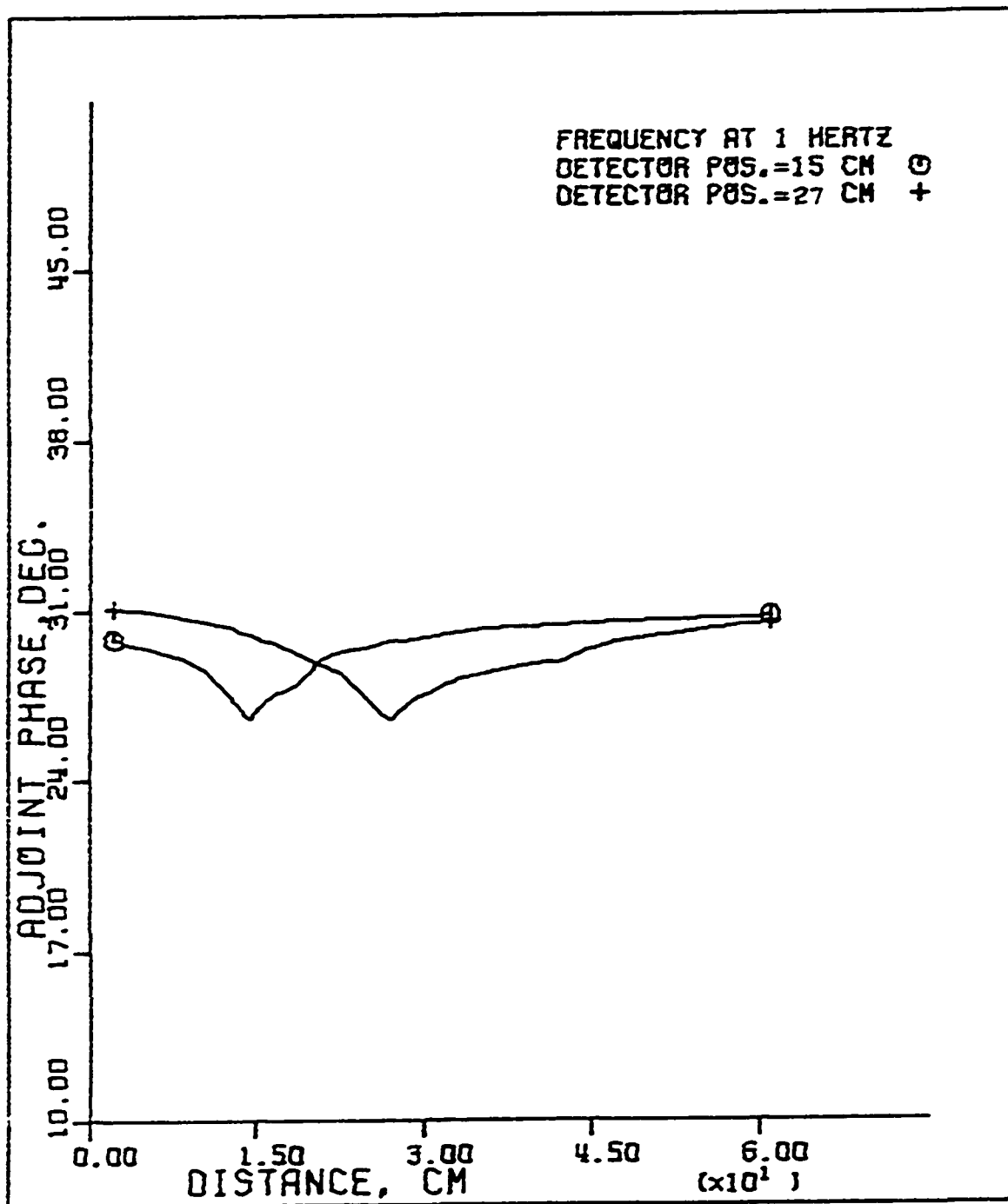


Figure B.8. The phase of the thermal adjoint functions along the z-axis ( $x = y = 0$ )

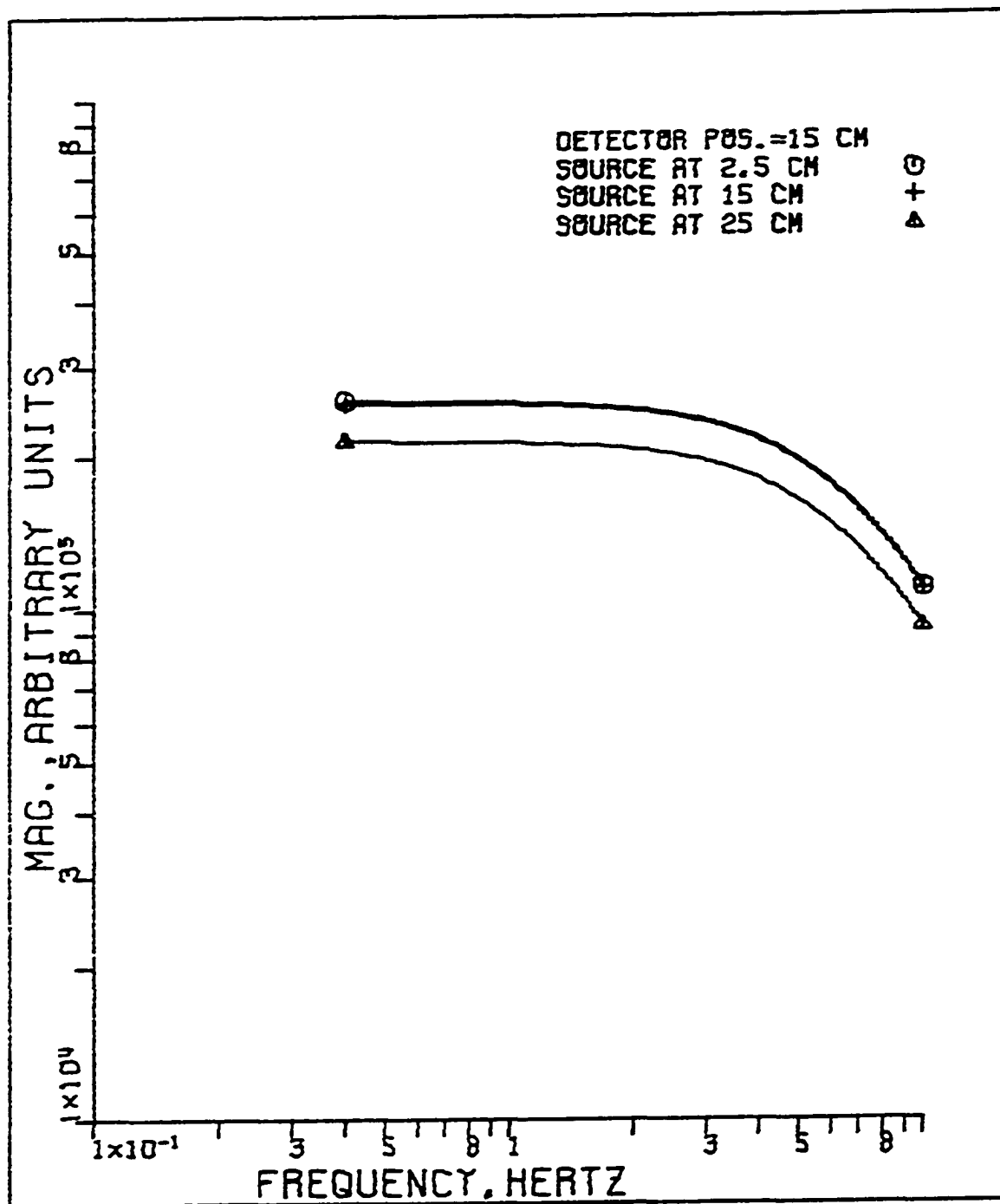


Figure B.9. The magnitude of the UTR-10 reactor response for various source locations along the Z-axis ( $x = y = 0$ )

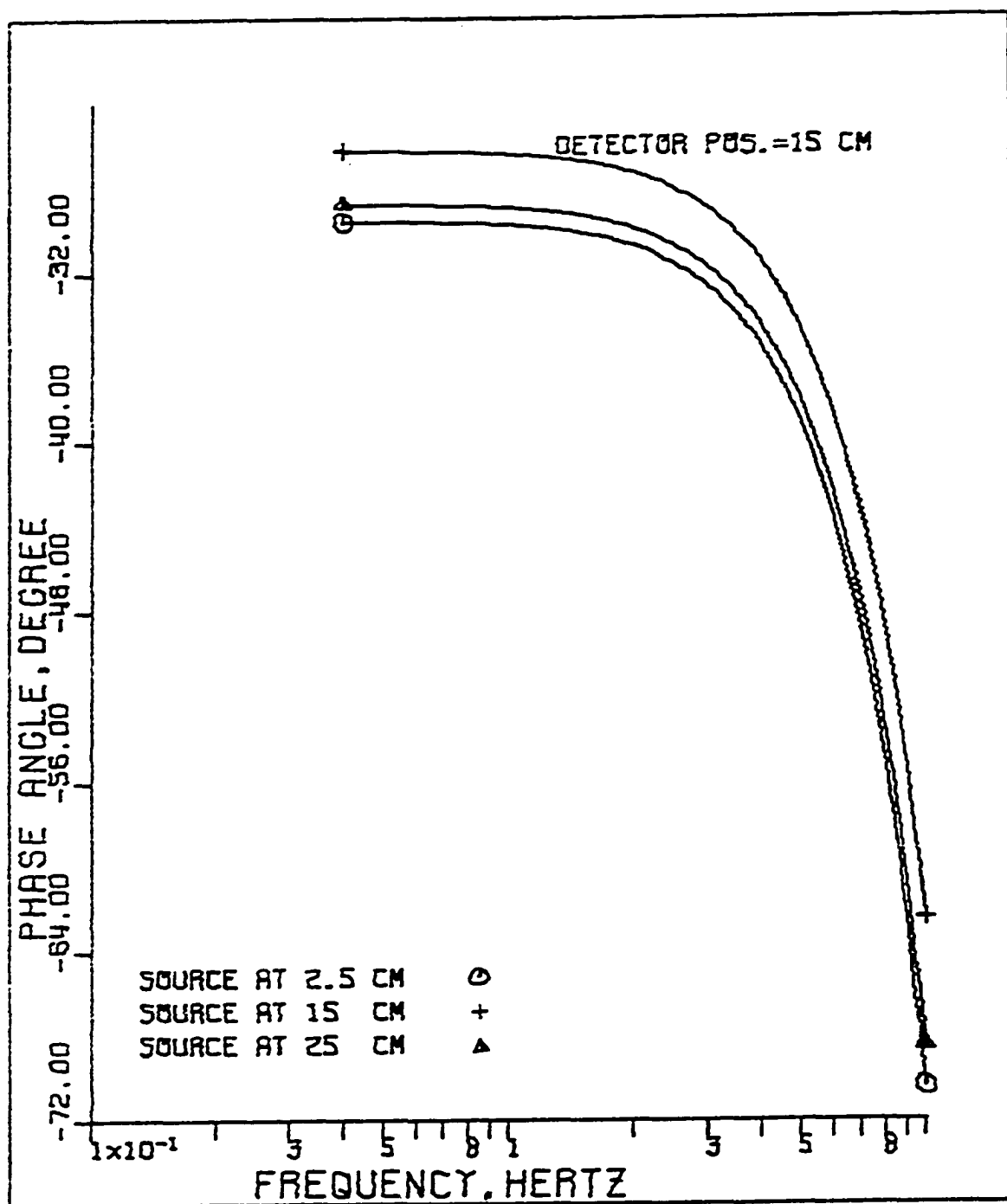


Figure B.10. The phase of the UTR-10 reactor response for various source locations along the Z-axis ( $x = y = 0$ )

#### D. Input Data Preparation

Individual cards may be punched in any manner [47], provided they can be read by eye. A number may be punched in any style, for example 8, 8., 8.0, .008E3, all are equivalents. Any work is terminated by a blank or numeric character, any number by a blank or nonnumeric character. Initial blanks are ignored. Any card, apart from the title card, which has a \* in column one is ignored. The following definitions are useful:

Zone = a homogenized two-dimensional region that consists of one or more materials

Channel = a vertical strip, of one mesh width, that consists of one or more zones.

A schematic diagram for a two-dimensional reactor is given in Figure B.11 as reference.

##### 1. Title card

: Any number of characters up to 72 (must be on one card).

##### 2. General constants (GC) card

The format is the word GC followed by five numbers: number of energy groups, g; number of delayed neutron groups, n; maximum number of materials, M in any zone Z; type of criticality control search (1 to 7); initial value of control eigenvalue, X (must be zones for controls 2, 3 and 7). The criticality control search

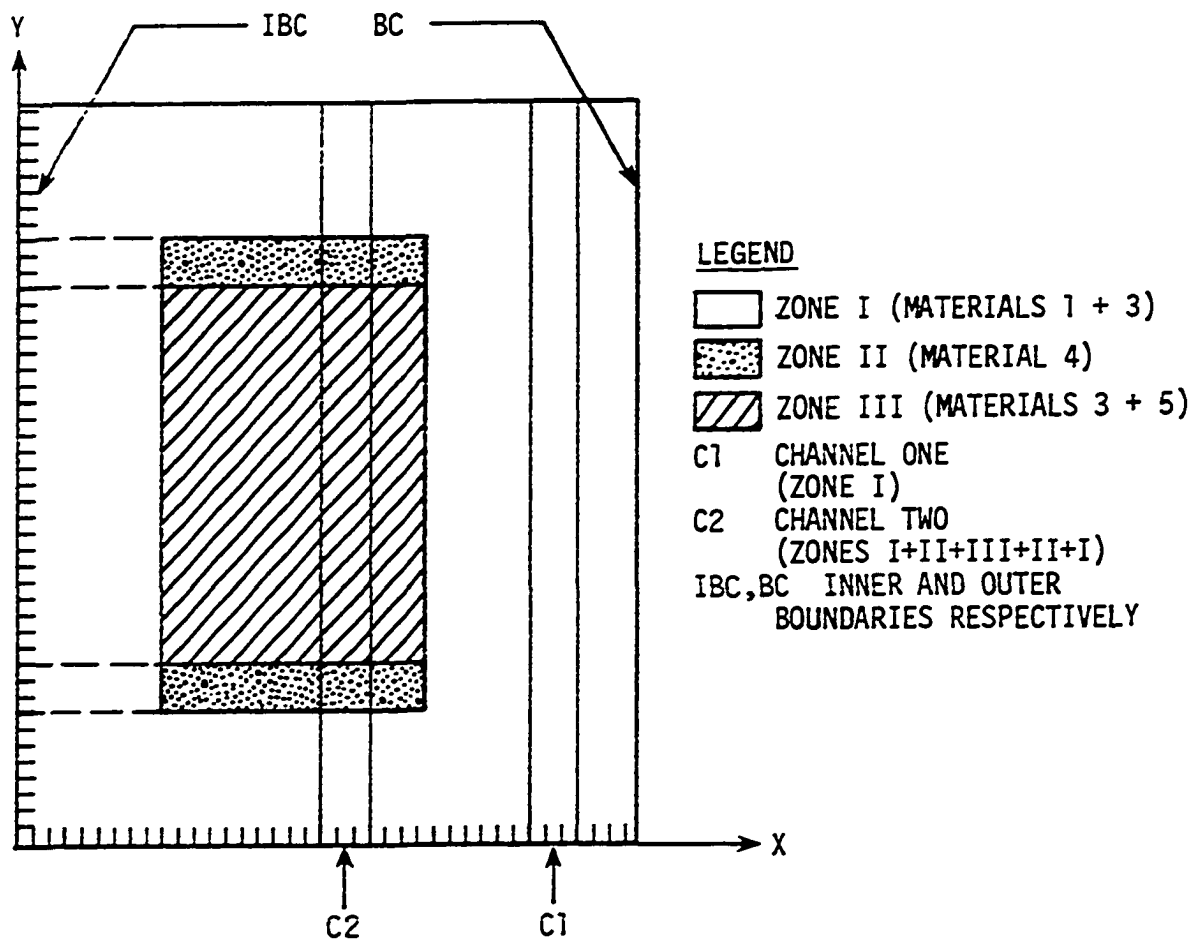


Figure B.11. A schematic of a two-dimensional reactor (illustrating the zone and channel concepts)

are: 1 =  $K_{eff}$ ; 2 = radial mesh; 3 = axial mesh (and one dimensional (1-D) mesh); 4 = composition; 5 = buckling; 6 = source; 7 = radial and axial mesh (refer to page 14 of [147]).

### 3. Geometry selector and buckling value (if any) card

The format is GEOMETRY  $\omega$   $B^2$ . The item  $\omega$  is one of six code words as follows

$\omega$  = SPH, CYL or SLAB for 1-D problems

= RZ, RT or XY for 2-D problems.

All except SPH and RZ may be followed by a single positive number equal to the buckling,  $B^2$ , to represent a finite bare system in a transverse dimension. If the  $B^2$  value is zero or is omitted, the system is infinite. The defaulted geometry is RZ.

### 4. Accuracy control card

The format is ACCURACY followed by five numbers to overwrite the standard assignment included in the code. With control type 1, 5 and 6 the standard numbers should be adequate but for other controls refer to page 17 of [47] for more details.

### 5. Radial mesh (mesh 1) card (cards)

The format is RM or XM followed by data to define  $r_{max}$  mesh widths in the first direction (R or X) in the form, for example: 0(0.7)5(0.62)9... $r_{max}$  which would specify the first five intervals with equal mesh

width of 0.7, the next four with mesh width of 0.62, etc. All widths are in cm. A mesh boundary must fall on every physical boundary in the problem, but mesh width may be changed at will within zones and the spacing should be fine where flux gradients are expected to be high.

6. Axial mesh (mesh 2) and 1-D mesh card(cards)

The format is any of the words ZM, TM, YM, RM or SM (for 1-D) followed by mesh width data in the second direction (Z, T, Y or S). The format is identical to that for the radial mesh above.

7. Isotope data card(cards)

For each of the isotopes, the word  $I_i$  ( $i = 1, 2, \dots$ ) is followed by a complete block of microscopic (or macroscopic, if preferred) data in the order:

$$\sigma_{tr}^g, \sigma_{rem}^g, v\Sigma_{fiss}^g \text{ and } \sigma_{scat}^{g \rightarrow g'}$$

The group index,  $g$  starts with  $g = 1, 2, \dots, N$  (number of groups) and the scattering matrix  $\sigma_{scat}^{g \rightarrow g'}$  is an  $(N \times N)$  matrix and should be given in the following order:

$$\begin{array}{cccc}
 c_{11} & c_{12} & \dots & c_{1N} \\
 c_{21} & c_{22} & \dots & c_{2N} \\
 \cdot & \cdot & & \cdot \\
 \cdot & \cdot & & \cdot \\
 c_{N1} & c_{N2} & \dots & c_{NN}
 \end{array}$$

8. Mixture data card(cards)

This card provides for isotopes mixing for each of the materials present, for example:

M2 I6 0.61 I2 0.21 I4 0.18

will define material 2 as a mixture of 0.61 (by volume) of isotope number 6, 0.21 of isotope number 2 and 0.18 of isotope number 4.

9. Zone data card(cards)

This card provides for materials specification in all the zones. For example:

Z3 M2 0.29 M1 0.31 M5 0.4

will define zone 3 as a mixture of 0.29 (by volume) of material number 2, 0.31 of material number 1 and 0.4 of material number 5.

10. Channel data (mesh 2 direction) and boundary conditions card(cards)

This card specifies the zone pattern for each channel.

For channel number one for example:

C1 0 Z3 2 Z1 7 Z5 10 1.E9 0

will define channel number 1 to consist (starting at the bottom and going upward) of 2 mesh widths of zone 3, followed by 5 mesh width of zone 1, followed by 3 mesh width of zone 5. The vacuum boundary condition (1.E9) is set at the bottom of the channel and a reflective boundary condition (0) at the top of the

channel. As many  $C_i$  sets of data are given as will cover the full horizontal mesh space. For a 1-D case, a single channel (C1) is needed.

11. Channel assignment (mesh 1 direction) card(cards)

This card specifies the layout pattern of the channels in the correct physical order by writing for example:

CA 0 C2 4 C3 7 C1 14

will assign channel 2 to fall across all the first 4 intervals, channel 3 across the next 3 and channel 1 across the last 7. The interval being those of mesh 1(x direction) and  $r_{max}$  being 14 in this case. For a 1-D case, no CA data is needed.

12. Inner boundary condition card

The format is the word IBC followed by a set of data numbers in the form, for example

0(1.E9)3(0)7(1.E9)16

will define a vacuum boundary for the first 3 mesh points in the Z direction (mesh 2), followed by the next 4 points with a reflective boundary and the last 9 points with a vacuum boundary. The number of mesh points in the Z direction are 16 in this example. If the IBC card is omitted, a reflective inner boundary condition is assumed.

13. Outer boundary condition card

The format is the word BC followed by a set of data numbers (written as for IBC) to specify the outer

boundary conditions. The default value is vacuum boundary condition.

14. Fission spectrum card

The format is the word SP followed by N values of the fission spectrum:  $X_1, X_2, \dots, X_N$ . After SP data will follow delayed neutron spectra, if any.

15. Control words card

After the last data item is given (this must be "SP"), a set of control words follow to control the course of the calculation. None of these except "STOP" is individually essential, and any of them may appear in any order.

- a. ENTER: commences solution of the problem. It must appear to achieve a solution.
- b. PRINT 2: to provide a standard output print, after the solution, with fluxes printed by channel. Recommended for outputting 1-D problems.
- c. PRINT 3: to print output with fluxes by group. Recommended for 2-D problems.
- d. NEXT: prepares to receive data for next problem. A title card must follow.
- e. ALTER w: will alter the data of the current problem as follows:  
 $w = \text{Mesh } l \ n$  followed by p numbers will overwrite the mesh l values starting at the nth.

- = Mesh 2 n (the same for mesh 2)
- =  $I_i$  followed by p numbers to overwrite the first p numbers of isotope i (use transport cross sections, not D's).
- = M2 7 0.65 I3 .91 ..., etc. would overwrite material 2 data to M2 I7 0.65 I13 0.91 ... etc.  
If the ALTER data is shorter in length than the full original M2 data, the remaining old data will stay unaffected. Do not write ALTER data of greater length than the original.
- f. DUMP: will dump complete problem information on to data set number 9.
- g. FLUX: read flux guess into current data set from old dump data set. This is a useful facility and can save about half a problem's running time if the old problem fluxes are reasonably similar physically to the new. Number of groups and mesh points must match for the two problems.
- h. ADJOINT: will set up the adjoint problem. ADJOINT repeated will cancel itself.
- i. DOUBLE: will halve the current mesh width in both directions. This feature is only available for the 2-D case.
- j. STOP: Must be included at the end of every CRAM data deck. Returns control to the monitor.

#### E. Sample Input Data to CRAM

CRAM was used to evaluate the frequency dependent adjoint response in two-groups and two-dimensions. The sample input data to CRAM, used in a representative modeling calculation, for the UTR-10 reactor is given below.

CASE 1 FREQUENCY = 1.00 C/S  
GC 5 0 1 6 80  
ACCURACY .002 .002 .002 .002 .02  
GEOMETRY XY 3.E-7  
XM 0(2.381)2(4.524)6(1.524)16(4.354)23  
YM 0(2.064)16(4.657)22 BC 0(1.E9)22  
\* GROUP CONSTANTS FOR FUEL REGION  
I 1 D  
0.100000E-08 0.1327444E 01 0.1327444E 01  
0.4976611E 00 0.4976611E 00  
0.100000E 01 0.2491331E-01 0.2491331E-01  
0.3434182E-01 0.3434182E-01  
0.000000E 00 0.4934548E-01 0.000000E 00  
0.000000E 00 0.000000E 00  
0.100000E 01 0.000000E 00 0.000000E 00  
0.000000E 00 0.000000E 00  
0.000000E 00 0.1205324E-02 0.4792444E-06  
0.900000E 00 0.1938580E-04  
0.000000E 00 -0.4792444E-06 0.1205324E-02  
-0.1938580E-04 0.4934548E-01  
0.000000E 00 0.2318973E-01 0.000000E 00  
0.000000E 00 0.3001706E-04  
0.000000E 00 0.000000E 00 0.2318973E-01  
-0.3001706E-04 0.000000E 00  
\* GROUP CONSTANTS FOR WATER REGION  
I 2 D  
0.100000E-08 0.1263185E 01 0.1263185E 01  
0.4480354E 00 0.4480354E 00  
0.100000E 01 0.3338891E-01 0.3338891E-01  
0.1246879E-01 0.1246879E-01  
0.000000E 00 0.000000E 00 0.000000E 00  
0.000000E 00 0.000000E 00  
0.100000E 01 0.000000E 00 0.000000E 00  
0.000000E 00 0.000000E 00  
0.000000E 00 0.000000E 00 0.5865591E-08

```

0.000000E 00  0.000000E 00
  0.000000E 00 -0.5865591E-08  0.000000E 00
-0.000000E 00  0.000000E 00
  0.000000E 00  0.3244445E-01  0.000000E 00
  0.000000E 00  0.2903276E-04
  0.000000E 00  0.0000000E 00  0.3244445E-01
-0.2903276E-04  0.0000000E 00
* GROUP CONSTANTS FOR GRAPHITE REGION
I 3 D
  0.1000000E-08  0.1152864E 01  0.1152864E 01
  0.9918190E 00  0.9918190E 00
  0.1000000E 01  0.3262653E-02  0.3262653E-02
  0.6412384E-03  0.6412384E-03
  0.0000000E 00  0.0000000E 00  0.0000000E 00
  0.0000000E 00  0.0000000E 00
  0.1000000E 01  0.0000000E 00  0.0000000E 00
  0.0000000E 00  0.0000000E 00
  0.0000000E 00  0.0000000E 00
  0.0000000E 00  0.0000000E 00  0.5266081E-08
  0.0000000E 00  0.0000000E 00
  0.0000000E 00 -0.5266081E-08  0.0000000E 00
-0.0000000E 00  0.0000000E 00
  0.0000000E 00  0.2873637E-02  0.0000000E 00
  0.0000000E 00  0.2858596E-04
  0.0000000E 00  0.0000000E 00  0.2873637E-02
-0.2858596E-04  0.0000000E 00
* GROUP CONSTANTS FOR DETECTOR REGION
I 4 D
  0.1000000E-08  0.1152864E 01  0.1152864E 01
  0.9918190E 00  0.9918190E 00
  0.1000000E 01  0.3894949E-03  0.3894949E-03
  0.6412384E-03  0.6412384E-03
  0.0000000E 00  0.0000000E 00  0.0000000E 00
  0.0000000E 00  0.0000000E 00
  0.1000000E 01  0.0000000E 00  0.0000000E 00
  0.5000000E-01  0.0000000E 00

```

0.000000E 00 0.000000E 00 0.5214264E-03  
0.000000E 00 0.000000E 00  
0.000000E 00 -0.5214264E-08 0.000000E 00  
-0.000000E 00 0.000000E 00  
0.000000E 00 0.2873637E-02 0.000000E 00  
0.000000E 00 0.2858596E-04  
0.000000E 00 0.000000E 00 0.2873637E-02  
-0.2858596E-04 0.000000E 00  
M1 I1 1 M2 I2 1 M3 I3 1 M4 I4 1  
Z1 M1 1 Z2 M2 1 Z3 M3 1 Z4 M4 1  
C1 0 Z3 6 Z4 7 Z3 22 0 1.E9  
C2 0 Z3 22 0 1.E9  
C3 0 Z1 16 Z2 22 0 1.E9  
CA 0 C1 1 C2 6 C3 16 C2 23  
SP 0 0 0 1 0  
ENTER PRINT 3  
STOP

XIII. APPENDIX C: THE COMPUTATIONS OF THE APSD  
AND CPSD OF THE VOID FRACTION  
FOR TWO-PHASE FLOW

The stochastic state equations for two phase flow in a one-dimensional channel were derived in Section B of Chapter III as Equations (3-60) through (3-63). Two different flow regimes were incorporated in the formulation, namely bubbly and slug flow. The space and frequency dependent Fourier transforms (FT) of two stochastic variables,  $\Delta\alpha$  and  $\Delta v$  (void fraction and velocity) were derived for each of the following cases:

- a. Noise sources are completely correlated in space.
- b. Noise sources are exponentially correlated in space.  
The correlation coefficient,  $\mu$ , was taken as  $30/M$  for a BWR channel [110], while a value of  $6.67/M$  was found more appropriate for the loop.
- c. Noise sources are uncorrelated in space.

The resulting APSD and CPSD were derived as Equations (3-90) through (3-95). These equations were programmed into the SOURCE code, which basically, computes and plots (if desired) the auto and cross power spectral densities of the stochastic variables  $\Delta\alpha$  and  $\Delta v$  for a given flow pattern (or patterns). The steady state solutions are required as input. A schematic flow diagram of this program is shown in Figure C.1.

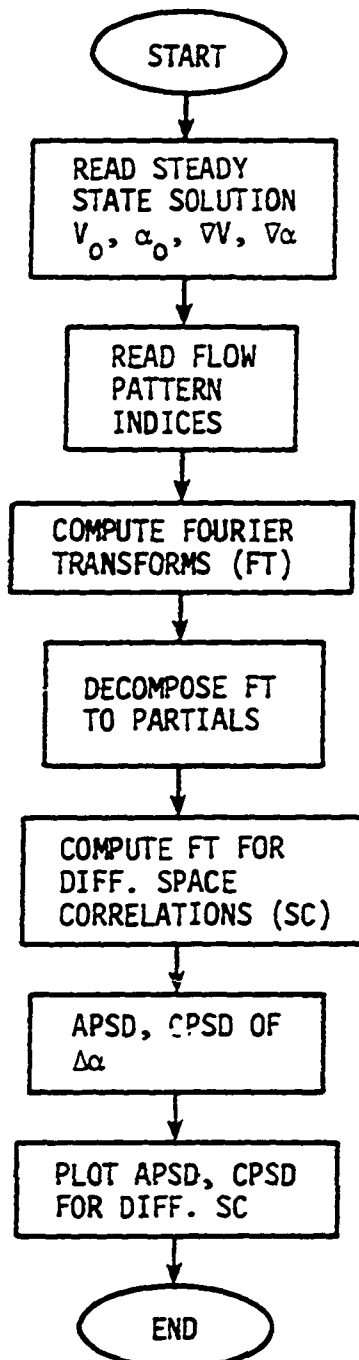


Figure C.1. Schematic flow diagram of the SOURCE code

### A. SOURCE Results

Figures C.2 through C.6 show some typical runs that illustrate the type of results to be expected from this code. The plots of the APSD's of the stochastic void fraction are given in Figure C.2 for coherent sources, Figure C.3 for exponentially coherent sources and Figure C.4 for uncorrelated sources. As indicated in these figures, the flow regime was taken to be bubbly in the lower 10 cm of the channel and to be slug above 10 cm. Three general features of interest are readily apparent, and are:

- a) As the noise sources lose coherence, the shape of the APSD loses, progressively, any structure that it originally had. For example, the APSD at a position of 8 cm, shows a prominent and well-defined peak around 6 Hz for coherent sources (Figure C.2), a minor peak around 6 Hz for exponentially coherent sources (Figure C.3) and no peak structure for uncorrelated sources (Figure C.4).
- b. As the noise sources lose coherence, the individual APSD shows a corresponding loss in magnitude.
- c. Regardless of the space correlation dependence of the noise sources, all the plots show that the magnitude of the APSD for slug flow is approximately four times greater than for bubbly flow.

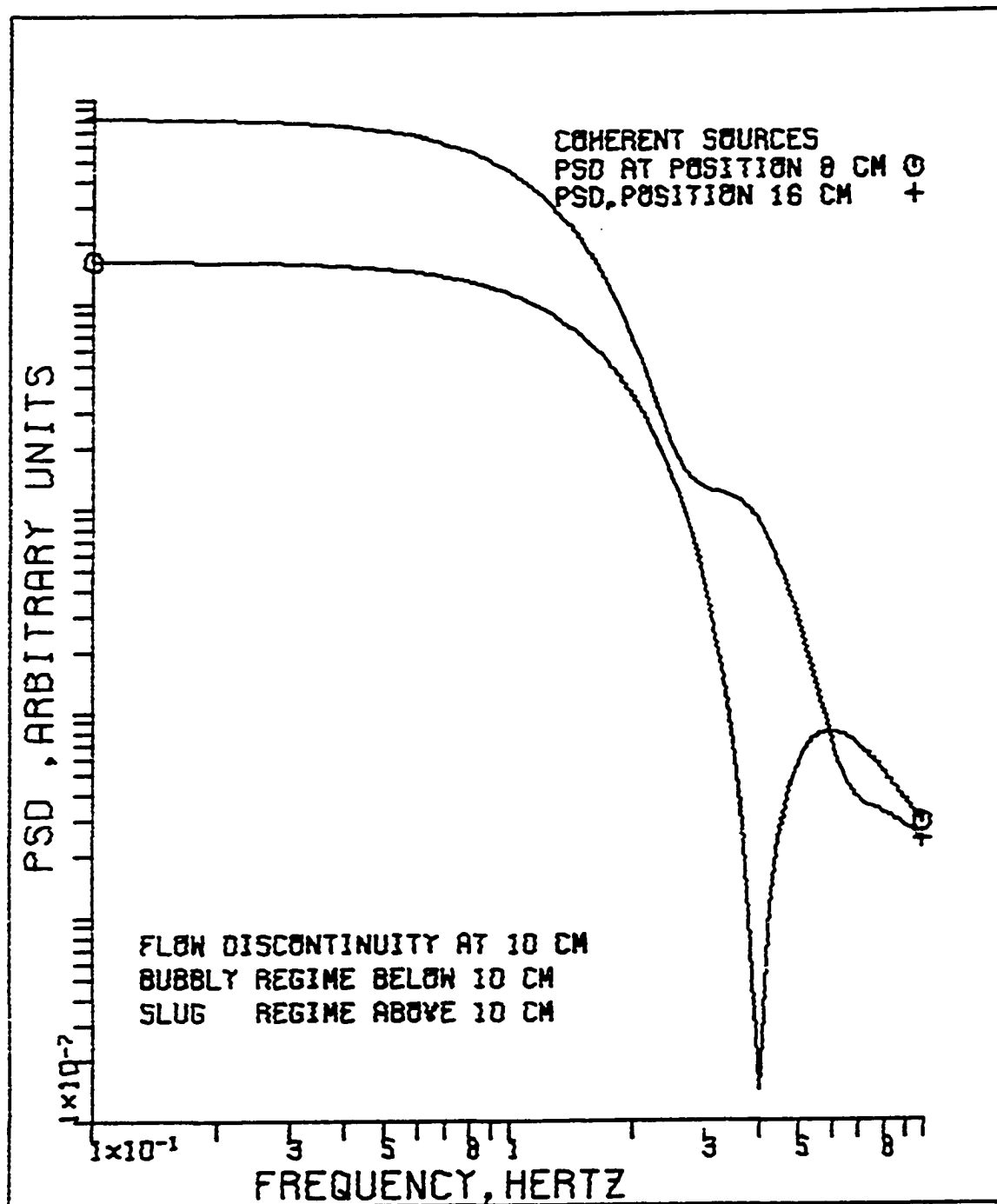


Figure C.2. APSD's due to void fluctuations for completely coherent sources

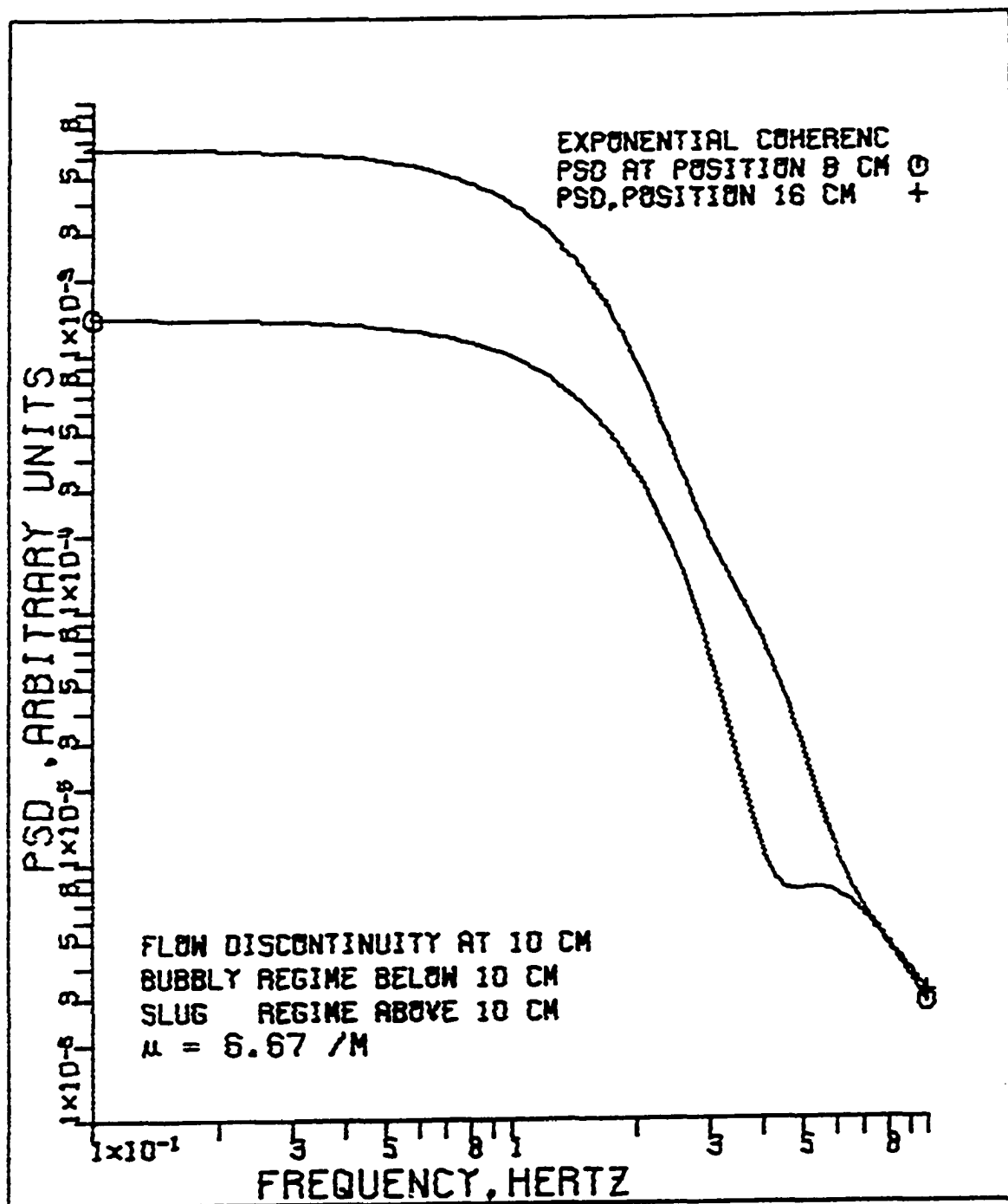


Figure C.3. APSD's due to void fluctuations for exponentially coherent sources

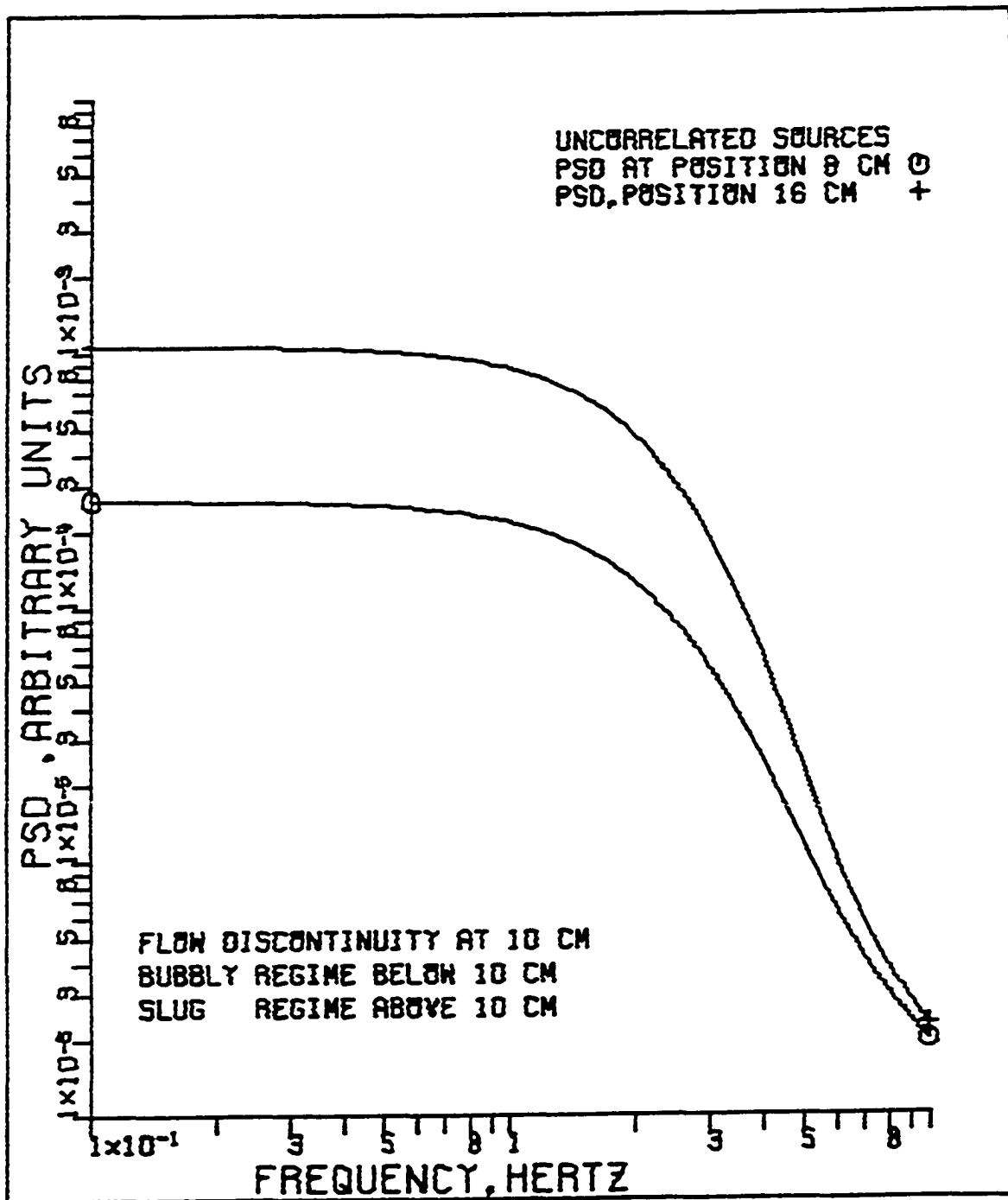


Figure C.4. APSD's due to void fluctuations for uncorrelated sources

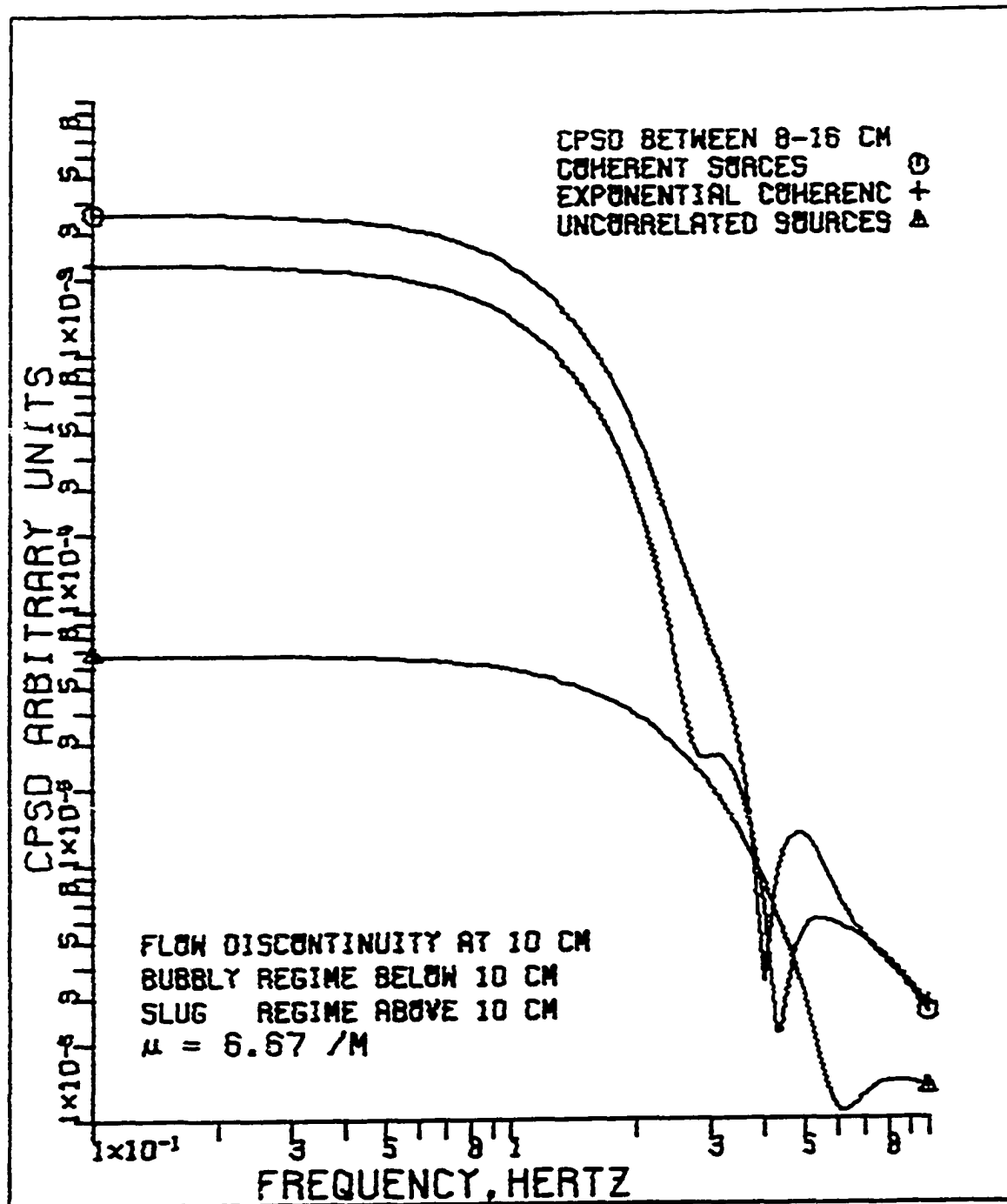


Figure C.5. The magnitude of the CPSD's due to void fluctuations for different space correlation dependence

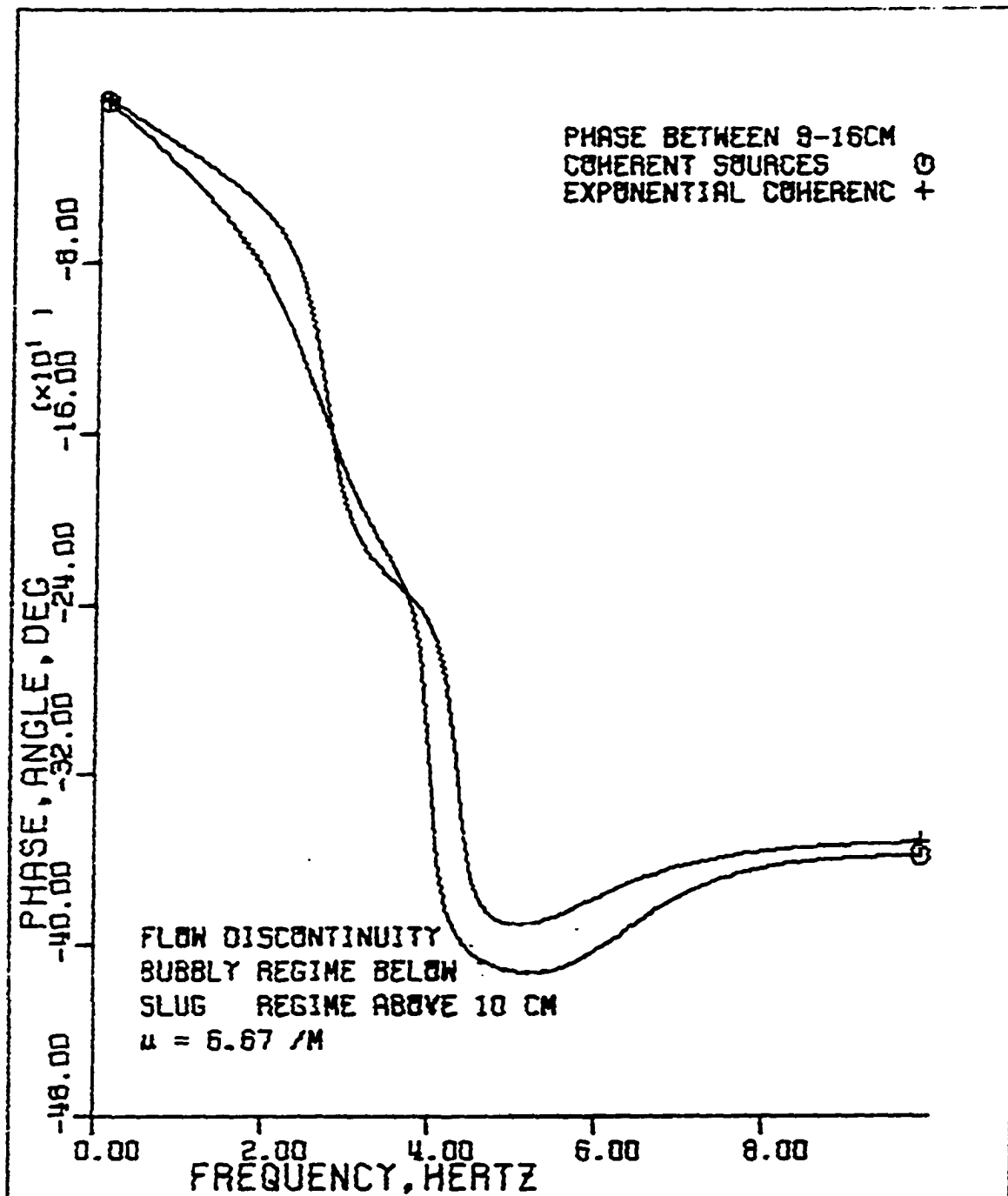


Figure C.6. The phase angle of the CPSD's due to void fluctuations for different space correlation dependence

The magnitudes and shapes of the CPSD's for a typical run are shown in Figures C.5 through C.6. It is interesting to observe that the magnitude decreases with successive loss of coherence. On the other hand, for both the coherent and exponentially coherent sources, the phase angle of the CPSD is always negative and vacillates around a straight line up to about 4 Hz where it begins to taper off to a constant value. This tapering off behavior is believed to be attributed to the relatively low magnitude of the CPSD in that frequency range as is evident in Figure C.5. The phase angle for the uncorrelated case was found, as expected, to be identically zero and subsequently was not plotted.

#### B. Listing of the SOURCE Code

Given below is a complete listing of the SOURCE code, along with a sample input data.

```

//STEP1 EXEC WATFIV,REGION.G0=256K,TIME.G0=(2.30)
//GO.SYSIN DD *
$JOB PROGRAMMER,TIME=120,PAGES=40
REAL K,MU
DIMENSION CC(100),CE(100),CG(100),PC(100),PE(100),PU(100),
        ZW6(100),WI(100),SC(100,30),SU(100,30),SE(100,30),YL(100),
        2Y2(100)
DIMENSION DEIA(30),DELV(30) ,V(30),AL(30)
DIMENSION DET,DZ,X1,ZC(22)
COMPLEX R(2,2),R1(2,2),R2(2,2),R3(2),X2,SAE(100,30)
COMPLEX BV(30,30),PA(30,30),Z7,X8,X9,SAC(100,30),SAT(100,
        130)
COMPLEX A(2,2),B(2,2),AI(2,2),D(2,2),E(2),X(2,30),C(2)
C Q IS DIAM. OF CHANNEL
DATA CF,S,K,Q / .005,1.537,1.537,.67,.0933/
DATA CE,S,K,Q / .005,1.537,1.537,.67,.0933/
DATA M1,M2/8,16/
DATA Z/16*.064,6*4.657/
F1(H,V)=-4.*CF*V/Q*(1.+H*(S-1.))*(1.+H*(S-1.))/((K-H)*
        1(1-S)/(K-H))
F2(H,V)=-32.2 -2.*CF*V/Q*V*(2.*H*(1.-S)*S-2-H*(1-H)*
        F1(H,V))/-4*CF*V/Q*(H*H*(1-S)+H*(S-2)+1)
F3(H,V)=-4.*CF*V/Q*(1.+H*(S-1.))*(1.+H*(S-1.))/((K-H)*
        1(1-S)/(K-H))
F4(H,V)=-32.2-4.*CF*V/Q*(1.+H*(S-1.))*(1.+H*(S-1.))/((K-H)*
        1S-1.)

```

```

X2=CMPLX(0.,0.)

MU=2.

N=22

NW=100

DO 93 I=1,NW

W7=I

W1(I)=W7*.1

93   W6(I)=W1(I)

P=2.*3.1415927

READ,(DELA(I),I=1,N)

READ,(DELV(I),I=1,N)

READ,( V(I),I=1,N)

READ,(AL(I),I=1,N)

DO 2000 II=1,22

Z(II)=Z(II)/30.

2000 ZC(II)=CMPLX(Z(II),0,)

X(1,1)=X2

X(2,1)=X2

C   KKK CONTROL MU

D) 1 IK=4,NW

W=W1(IK)

IJ=IK-3

W=W*P

DO 15 M=1,N

VL=V(M)

AL=AL(M)

```

```

B(1,1)=CMPLX(DELA(M),0.)

T=DELV(M)

B(1,2)=CMPLX(T,W)

IF(M.GT.13) GO TO 77

B(2,1)=CMPLX(F1(AL,V1),W)

B(2,2)=CMPLX(F2(AL,V1),0.)

GO TO 88

77   B(2,1)=CMPLX(F3(AL,V1),W)

      B(2,2)=CMPLX(F4(AL,V1),0.)

88   CONTINUE

A(1,1)=CMPLX(AL-1.,0.)

A(1,2)=CMPLX(V1,0.)

A(2,1)=CMPLX(V1,0.)

A(2,2)=CMPLX(0.,0.)

C(1)=CMPLX(-.1,0.)

C(2)=CMPLX(0.,0.)

DZ=ZC(M)

DET=A(1,1)*A(2,2)-A(1,2)*A(2,1)

DET=CMPLX(1.,0.)/DET*DZ

AI(1,1)=A(2,2)*DET

AI(2,2)=A(1,1)*DET

AI(1,2)=-A(1,2)*DET

AI(2,1)=-A(2,1)*DET

DO 2 I=1,2

DO 2 J=1,2

X1=X2

```

```

DO 3 L=1,2
3   Xl=Xl+AI(I,L)*B(L,J)
2   D(I,J)=Xl
    DO 4 I=1,2
      E(I)=AI(I,1)*C(1)+AI(I,2)*C(2)
    DO 4 J=1,2
      Xl=CMPLX(0.,0.)
      IF(I.EQ.J) Xl=CMPLX(1.,0.)
      R(I,J)=Xl+D(I,J)
4   CONTINUE

C INV. OF R, STORED IN R
DET=R(1,1)*R(2,2)-R(1,2)*R(2,1)
DET=CMPLX(1.,0.)/DET
Xl=R(1,1)
R(1,1)=R(2,2)*DET
R(2,2)=Xl*DET
R(1,2)=-R(1,2)*DET
R(2,1)=-R(2,1)*DET
DO 50 I=1,2
R3(I)=R(I,1)*E(1)+R(I,2)*E(2)
50  CONTINUE
55  CONTINUE
DO 5 I=1,2
5   X(I,M+L)= R(I,1)*X(1,M)+ R(I,2)*X(2,M)+R3(I)
DO 10 KK=1,M
IF(KK.GT.1) GO TO 11

```

```

PV(M,KK)=R3(1)

PA(M,KK)=R3(2)

GO TO 10

11  PV(m,KK)=R(1,1)*PV(M-1,KK-1)+R(1,2)*PA(M-1,KK-1)
    PA(M,KK)=R(2,1)*PV(M-1,KK-1)+R(2,2)*PA(M-1,KK-1)

10  CONTINUE

S=(1.-A1(M))/(K-A1(M))

15  CONTINUE

DO 12 M=1,N

X1=X2

X7=X2

X9=X2

DO 13 I=1,M

DO 13 J=1,M

C PUT CONJ. OF PA IN X8

C     G1=REAL(PA(M,I))

C     G2=A1MAG(PA(M,I))

C     X8=CMPLX(G1,-G2)

C     X8=X8*PA(M,J)

X8=PA(M,J)

IF(I.EQ.J) X9=X9+X8

X1=X1+X8

C     EX=EX*.5

IF(I.GT.J) TO TO 600

IF(I.LT.J) GO TO 700

GO TO 13

```

```

600  SUM=0.

      DO 601 K3=I,J

601  SUM+Z(K3)

      EX=-SUM*MU

      EX=EX*.5

      GO TO 13

700  SUM=0.

      DO 701 K3=K3=J,I

      SUM=SUM+Z(K3)

      EX=-SUM*MU

      EX=EX*.5

13    X7=X7+CMPLX(EXP(EX),0.)*X8

C   SC FOR COH. SOURSES

C     SC(IJ,M)=CABS(X1)

C   SE FOR EXP. COH. SOURSES

C     SE(IJ,M)=CABS(X7)

C   SU FOR UN CORRELATED SOURSES

C     SU(IJ,M)=CABS(X9)

      SAC(IJ,M)=X1

      SAU(IJ,M)=X9

12    SAE(IJ,M)=X7

      WRITE(10)(SAC(IJ, JJ),SAU(IJ,JJ),SAE(IJ,JJ),JJ=1,N)

      GO TO 1

      X1=X2

      X7=X2

      X9=X2

```

```

DO 20 I=1,M1

DO 20 J=1,M2

G1=REAL(PA(M1,I))

G2=AIMAG(PA(M1,I))

X8=CMPLX(G1,-G2)

X8=X8*PA(M2,J)

IF(I.EQ.J)X9=X9+X8

X1=X1+X8

20 X7=X7+CMPLX(EXP(EX),0.)*X8

CC(IJ)=CABS(X1)

CE(IJ)=CABS(X7)

CU(IJ)=CABS(X9)

VV=360./P

PC(IJ)=0.

PE(IJ)=0.

PU(IJ)=0.

IF(REAL(X1).NE.0.)PC(IJ)=ATAN(AIMAG(X1)/REAL(X1))*VV

IF(REAL(X7).NE.0.)PE(IJ)=ATAN(AIMAG(X7)/REAL(X7))*VV

IF(REAL(X9).NE.0.)PU(IJ)=ATAN(AIMAG(X9)/REAL(X9))*VV

PRINT,X1,X7,X9

1 CONTINUE

GO TO 104

DO 16 I=1,NW

Y1(I)= ALOG 10(SC(I,M1))

WI(I)= ALOG 10(W1(I))

16 Y2(I)= ALOG 10(SC(I,M2))

```

```

CALL GRAPH(NW,W1,Y1,1,102,-5.,-6., .5,0., .5,0.,"FREQUENCY,
1HERTZ;"

2      , 'PSD ,ARBITRARY UNITS'

3,'COHERENT SOURCES; , 'PSD AT POSITION 8 CM')

CALL GRAPHS(NW,W1,Y2,3,102,'PSD,POSITION 16 CM;')

C   CALL LETTRS(.3,1.,.1,'FLOW DISCONTINUITY IT 10 CM',0.,27)
C   CALL LETTRS(.3,.8,.1,'BUBBLY REGIME BELOW 10 CM',0.,25)
C   CALL LETTRS(.3,.6,.1,'SLUG    REGIME ABOVE 10 CM',0.,25)

DO 17 I=1,NW

Y1(I)=ALOG 10(SU(I,M1))

17  Y2(I)=ALOG 10(SU(I,M2))

CALL GRAPH(NW,W1,Y1,1,102,-5.,-6., .5,0.,'FREQUENCY,
1HERTZ;"

2      , 'PSD ,ARBITRARY UNITS'

3,'UNCORRELATED SOURCES' , 'PSD AT POSITION 8 CM')

CALL GRAPHS(NW,W1,Y2,3,102,'PSD,POSITION 16 CM;')

C   CALL LETTRS(.3,1.,.1,'FLOW DISCONTINUITY AT 10 CM',0.,27)
C   CALL LETTRS(.3,.8,.1,'BUBBLY REGIME BELOW 10 CM',0.,25)
C   CALL LETTRS(.3,.6,.1,'SLUG    REGIME ABOVE 10 CM',0.,25)

DO 18 I=1,NW

Y1(I)=ALOG 10(SE(I,M1))

18  Y2(I)=ALOG 10(SE(I,M2))

CALL GRAPH(NW,W1,Y1,1,102,-5.,-6., .5,0., .5,0.,
1"FREQUENCY,HERTZ;"

2      , 'PSD ,ARBITRARY UNITS'

3,'EXPONENTIAL COHERENC' , "PSD AT POSITION 8CM")

```

```
CALL GRAPHS(NW,W1,Y2,3,102,"PSD,POSITION 16 Cm;")  
C CALL LETTRS(.3,1.,.1,"FLOW DISCONTINUITY AT 10 CM",0.,27)  
C call lettrs(.3,.8,.1,"BUBBLY REGIME BELOW 10 CM",0.,25)  
C CALL LETTRS(.3,.6,.1,"SLUG REGIME ABOVE 10 CM",0.,25)  
C CALL LETTRS(0.30,0.400,.125,"S = 6.67 /M",0.,11)  
103 CONTINUE  
  
DO 23 I=1,NW  
  
23 PRINT,CC(I),PC(I),CE(I),PE(I)  
  
CC(1)=ALOG 10(CC(1))  
  
CE(1)=ALOG 10(CE(1))  
  
CU(1)=ALOG 10 (CU(1))  
  
Y1(1)=PC(1)  
  
Y2(1)=PE(1)  
  
Y3(1)=PU(1)  
  
CNT1=0.  
  
CNT2=0.  
  
CNT3=0.  
  
DO 21 I=2,NW  
  
CC(I)= ALOG 10(CC(I))  
  
CE(I)= ALOG 10(CE(I))  
  
CU(I)= ALOG 10(CU(I))  
  
Y1(I)=PC(I)  
  
Y2(I)=PE(I)  
  
Y3(I)=PU(I)  
  
V1=1.  
  
V2=1.
```

```

V3=0.

IF(Y1(I-1).NE.0.)V1=Y1(I)/Y1(I-1)
IF(Y2(I-1).NE.0.)V2=Y2(I)/Y2(I-1)
IF(Y3(I-1).NE.0.)V3=Y3(I)/Y3(I-1)

IF(V1.LT.0.)CNT1=CNT1-90.
IF(V2.LT.0.)CNT2=CNT2-90.
IF(V3.LT.0.)CNT3=CNT3-90.

IF(Y1(I).LT.0.)PC(I)=PC(I)+CNT1
IF(Y1(I).GT.0.)PC(I)=PC(I)+CNT1-90.

IF(Y2(I).LT.0.)PE(I)=PE(I)+CNT2
IF(Y3(I).LT.0.)PU(I)=PU(I)+CNT3

IF(Y2(I).GT.0.)PE(I)=PE(I)+CNT2-90.
IF(Y3(I).GT.0.)PU(I)=PU(I)+CNT3-90.

PU(I)=PU(I)+90.

PRINT,CC(I),PC(I),CE(I),PE(I),CU(I),PU(I)

21   CONTINUE

      DO 237 I1=1,2

      DO 220 I=2,NW
         IK=I

220   IF((PC(I-1)-PC(I)),GT.90.)GO TO 225
         GO TO 227

225   DO 226 I=IK,NW
226   PC(I)=PC(I)+180.

227   CONTINUE

      DO 230 I=2,NW
         IK=I

```

```

230 IF((PE(I-1)-PE(I)).GT.90.)GO TO 235
      GO TO 237

235 DO 236 I=IK,NW
236 PE(I)=PE(I)+180.
237 CONTINUE

      CALL GRAPH(NW,W1,CC,1,102,-5.,-6., .5,0., .5,0.,
1"FREQUENCY,HERTZ;"

1     , 'CPSD ARBITRARY UNITS'
2,"CPSD BETWEEN 8-16 CM","COHERENT SORCES;")

      CALL GRAPHS(NW,W1,CE,3,102,"EXPONENTIAL COHERENC")
      CALL GRAPHS(NW,W1,CU,2,102,"UNCORRELATED SOURCES")

C     CALL LETTRS(.3,1.,.1,"FLOW DISCONTINUITY AT 10 CM",0.,27)
C     CALL LETTRS(.3,.8,.1,"BUBBLY REGIME BELOW 10 CM",0.,25)
C     CALL LETTRS(.3,.6,.1,"SLUG      REGIME ABOVE 10 CM",0.,25)
C     CALL LETTRS(0.30,0.400,.125,"S = 6.67 /M",0.,11)

      CALL GRAPH(NW,W6,PC,1,104, 5., 6., .0,0.,0.0,0.,
1"FREQUENCY,HERTZ;"

1     , 'PHASE,ANGLE,DEG;', 'PHASE BETWEEN 8-16CM' ,
2'COHERENT SOURCES;')

      CALL GRAPHS(NW,W6,PE,3,104,"EXPONENTIAL COHERENC")
C     CALL LETTRS(.3,1.,.10,"FLOW DISCONTINUITY AT 10 CM",0.,27)
C     CALL LETTRS(.3,.8,.10,"BUBBLY REGIME BELOW 10 CM",0.,25)
C     CALL LETTRS(.3,.6,.10,"SLUG      REGIME ABOVE 10 CM",0.,25)
C     CALL LETTRS(0.30,0.400,.100,"S = 6.67 /M",0.,11)

104  CONTINUE

      STOP

```

```
END

$ENTRY

.02097 .020978 .01948 .01817 .01701 .0159 .015058 .01422 .0134
.0128 .01217 .01159
.0061 .0061 .00601 .00587 .00575 .0056 .0124 .01182 .01128
.01078
.0466 .0466 .04536 .04423 .0432 .0422 .0414 .0405 .0398 .039
.038 .0379
.03599 .03599 .0358 .0356 .0355 .0354 .0795 .07879 .0782 .07777
2. 2.0466 2.09 2.136 2.179 2.22 2.26 2.3 2.34 2.38 2.42 2.46
3. 3.836 3.87 3.9 3.94 3.98 4.05 4.136 4.22 4.292
.1 .121 .14046 .158 .17566 .1916 .2066 .221 .2344 .247 .2593
.2709
.349 .356 .362 .368 .3737 .379 .392 .40366 .415 .4257
//GO.FT10F001 DD SPACE=(TRK,(019,001),RLSE),
//      DSN=M.I4702.SOURD,DISP=(NEW,CATLG),
//      UNIT=DISK,
//      DCB=(RECFM=VBS,BLKSIZE=808,LRECL=804)
//GO.FT14F001 DD DSNAME=&SM,UNIT=SCRTCH,DISP=(NEW,PASS),
//      SPACE=(800,(120,15)),DCB=(RECFM=VBS,LRECL=796,BLKSIZE=800)
//STEP2 EXEC PLOT,PLOTTER=INCRMNTL,FORM=W
/*
```